W.K. Dahm ED31

ROCKWELL INTERNATIONAL

Rocketdyne Division
6633 Canoga Ave.
Canoga Park, CA. 91304

FLOW INDUCED VIBRATIONS IN THE SSME INJECTOR HEADS

FINAL REPORT

NO. RI/RD 91-157

CONTRACT NO.

NAS8-36195

JUNE 1991

PREPARED BY:

F.A. Lepore

Frank A. Lepore
Applied Fluid Dynamics

APPROVED BY:

Harry C. Dodson

Harry C. Dodson
Program Manager

ACKNOWLEDGEMENTS

The author would like to acknowledge the continued encouragement and guidance of his manager, Dr. L. K. Sharma and the Program Manager, Mr. H. C. Dodson. Valuable discussions with Dr. G.V.R. Rao during the course of this investigation are also appreciated. The support of Messrs. G. M. O'Connor, D. R. Richard and W. C. Cuan during the early phases of this study is also acknowledged.

The author would like to take this opportunity to acknowledge the outstanding and timely support of Dr. H. J. Connors of the Advanced Energy Systems Division of the Westinghouse Electric Corporation.

Without the dedication of the Aerophysics Laboratories personnel of NASA's George C. Marshall Space Flight Center in Huntsville, AL the test program phase of this study would not be possible. The author would like in particular to thank Messrs. P. Ramsey, H. Bush and J. Heaman for their support in facility and model set-up and instrumentation.The help of Mr. Bruce Epps of Rockwell's Space Systems Division is also acknowledged. The technical data reduction support of Mr. Homero Hidalgo and Ms. Lauren Mahorter is gratefully acknowledged. Additionally, helpful discussions with Mr. H. Struck during the course of this investigation is also noted. The support over the years of the Program Monitor, Dr. Werner Dahm is sincerely appreciated.

Finally, the author would like to thank Ms. Laurie Beerman for her help in preparing this document.

FOREWORD

This report is submitted by the Rocketdyne Division of Rockwell International, Canoga Park, CA, to the Contracts Office, George C. Marshall Space Flight Center, Huntsville, AL, as interim Final Report in support of Contract No. NAS8-36195.

ABSTRACT

This report presents the results of a research study on the fluid elastic instability boundary for various geometries of the Space Shuttle Main Engine (SSME) injector under cross flow and skimming flow conditions. Tasks being reported include: (1) Pretest Analysis, through which the relevant parameters and a properly simulated test approach using full scale SSME hardware have been determined; (2) Lox Post model design, based upon requirements set forth by the pretest analysis; (3) Lox Post model fabrication, instrumentation and installation; (4) Testing, through which an attempt has been made to establish experimentally the stability boundaries for both skimming and cross flow conditions; and (5) Data analysis and interpretation, whereby experimental data is interpreted to provide SSME stability boundaries.

A discussion of the technical approach used for accomplishing the requirements of the Statement of Work initially provided by the Technical Proposal (Ref.(1)) is also provided in this report. Although LOX post instability was not observed in the course of the experimental phase of the program, it was possible to infer from the test data an approximate position of the instability threshold line. A discussion will be included in this report on the conclusions drawn based on various extrapolation techniques employed in the data analysis phase of the project.

CONTENTS

CONTENTS (CONTINUED)

ILLUSTRATIONS

ILLUSTRATIONS (CONTINUED)

ILLUSTRATIONS (CONTINUED)

TABLES

INTRODUCTION

This report is being submitted to the NASA George C. Marshall Space Flight Center to document the study conducted on the Flow-Induced Vibrations in the Space Shuttle Main Engine (SSME) Powerhead. The subject of this study is important to the rocket engine industry in terms of upgrading current engines and improving the performance of future engines. It is also of great interest to Rocketdyne because of its potential impact on Rocketdyne current and future products, including the SSME.

In the course of this technical effort, existing full-scale main injector hardware was utilized; this decision was made in view of the considerable air flow testing experience accumulated during the development of the SSME in the past decade. This has brought significant benefits to the program, in terms of economics, technology utilization and direct applicability of experimental results to the existing SSME hardware. It should also be noted that the present study is an extension of a preliminary investigation of LOX post instability conducted under the development SSME contract.

A portion of the program was subcontracted to the Advanced Energy Systems Division of the Westinghouse Electric Corporation to utilize their internationally recognized expertise in flow-induced vibrations of tube bundles. The combination of talent and expertise from the two companies has greatly enhanced the overall technical capabilities of the resulting team.

This report is organized into the following sections: Introduction, Technical Background, Program Overview, Analysis and Discussion of Experimental Results, and, Conclusions and Recommendations. The Introduction outlines the problem and provides a program summary.

The Technical Background contains three major sections. A description of the flow-field in the SSME powerhead, the mechanisms which control flow-induced vibrations, and a summary of previous experimental work carried out by Rocketdyne as well as other workers in this field. The Program Overview is an in-depth description of the development phase of the program; it addresses the analysis, design and fabrication of the LOX Post models utilized in the experimental phase, as well as test facilities, equipment and procedures employed. The section on Experimental Results focuses on the experimental data analysis which includes the overall steady-state powerhead flow field as well as the high frequency response of the LOX posts.

STATEMENT OF PROBLEM

The Rocketdyne designed and built Space Shuttle Main Engines have performed exceptionally well during all launches performed to date, logging several hours of total engine burn time. However, in the very early years of the program, main injector problems occurred in the form of LOX post failures. These problems were overcome initially by introducing shields on the outer row LOX posts, and later by also changing the LOX posts material such that its thermo-mechanical properties would permit a higher yield strength at elevated temperatures. Since there are penalties associated with the shields, i.e. added weight and unrecoverable fluid total pressure loss, it is of great interest to determine the cause of the problems with an eye towards a less adverse solution.

There are three potential mechanisms that may lead to failure in a configuration such as the main injector. They are vortex shedding, turbulence buffeting, and fluidelastic excitation. Vortex shedding has been ruled out as the actual cause by the use of air flow and engine test data. Turbulence buffeting cannot be ruled out, although test data indicate its magnitude to be too low to be the primary cause of the problem. This leaves fluidelastic excitation as the leading failure mechanism candidate.

Fluidelastic excitation has been observed in heat exchangers with tube bundles to cause large amplitude tube vibration leading to sudden failure. This phenomenon is characterized by a critical velocity below which vibration amplitudes are generally small and governed by turbulence buffeting vortex shedding. Above the critical velocity the amplitude increases exponentially with velocity until material failure occurs. The critical velocity defines the stability boundary for the system. Determination of the stability boundary is the central problem in consideration of fluidelastic coupling of any system.

For the SSME, the role of fluidelastic excitation can be determined by finding the stability boundary of the Main Injector. This is to be done in the proposed program. Because different sections of the Main Injector are affected differently by the flow, i.e. one section appears to be in cross flow while another is in skimming or tangential flow, the stability boundary is a function of spatial position, and therefore must be treated as such.

PROGRAM SUMMARY

The technical effort for this research study entails determining the fluidelastic stability boundary for different sections of the SSME main injector. To achieve this objective, a full-scale injector was modified such that strategically located LOX posts were substituted by geometrically similar models. Such models were fabricated from "Vespel", a material specially selected to respond to fluidelastic instability at a lower critical velocity while retaining similar mode shape characteristics of the prototype LOX post. The injector was then instrumented and tested in a full-scale Hot Gas Manifold (HGM) using compressed air as flow test medium.

The first task of the study was to perform a detailed pre-test analysis during which important flow and structural parameters were defined and chosen. Based on this analysis and a comprehensive investigation of suitable simulation methods, a test approach was then selected. Several combinations of structural boundary conditions were considered in the selection process in an effort to closely simulate the prototype hardware. After detailed scrutiny, it was ultimately decided to design all LOX post models with fixed/fixed end conditions.

Following the design and fabrication of the model LOX posts, strain gages were installed and calibration tests performed to assess the strain response per input unit load. This procedure later proved helpful in estimating and cross-checking the actual aerodynamic forces acting on each LOX post element. Three groups of LOX posts were installed in separate regions of the outer main injector rows (rows 11 through 13), approximately corresponding to areas known from past experience to be susceptible to LOX post failures. Each LOX post element was instrumented with two pairs of strain gages acting in planes normal and tangential to the injector's radius of curvature; this was necessary in order to measure lateral and transverse deflections.

Air flow testing was conducted at the Aerophysics Laboratories of NASA's George C. Marshall Space Flight Center in Huntsville, Alabama. Several test runs were made at different transfer duct exit velocities and densities in order to assess the respective influence of reduced velocity and damping parameter on the stability threshold. Despite numerous attempts at very high equivalent engine power levels, all LOX posts were never exposed to a sufficiently severe environment to cause fluidelastic instability.

1.0 TECHNICAL BACKGROUND

The investigation of flow-induced vibration, and its relation to the complex flow in the Space Shuttle Main Engine, is best preceded by a technical discussion encompassing several areas. The following discussion serves as a thorough and appropriate background for the flow-induced vibration study being presently reported. The following topics will be discussed in this section: (1) the general SSME operation, with emphasis on the Hot Gas Manifold (HGM) and Main Injector flowfields and other related components, including a history of previous main injector failures; (2) the physical mechanisms involved in flow induced vibration phenomena, including the effects of array geometry; and (3) the results obtained from Rocketdyne's investigations of SSME LOX post stability as well as from other prominent investigators.

SSME FLOW FIELD DESCRIPTION

Figure 1.1 shows a cross-sectional view of the SSME powerhead. The figure identifies the major components of the powerhead including the hot gas manifold, which is the main structural backbone of the engine, supporting the preburners and turbopumps and forming the transfer ducts leading to the main injector. A cutaway view of the HGM is shown in Figure 1.2. The main injector is illustrated in Figure 1.3, with a detail of a portion of one of the main injector LOX post elements shown in Figure 1.4.

Figure 1.1 - SSME Powerhead

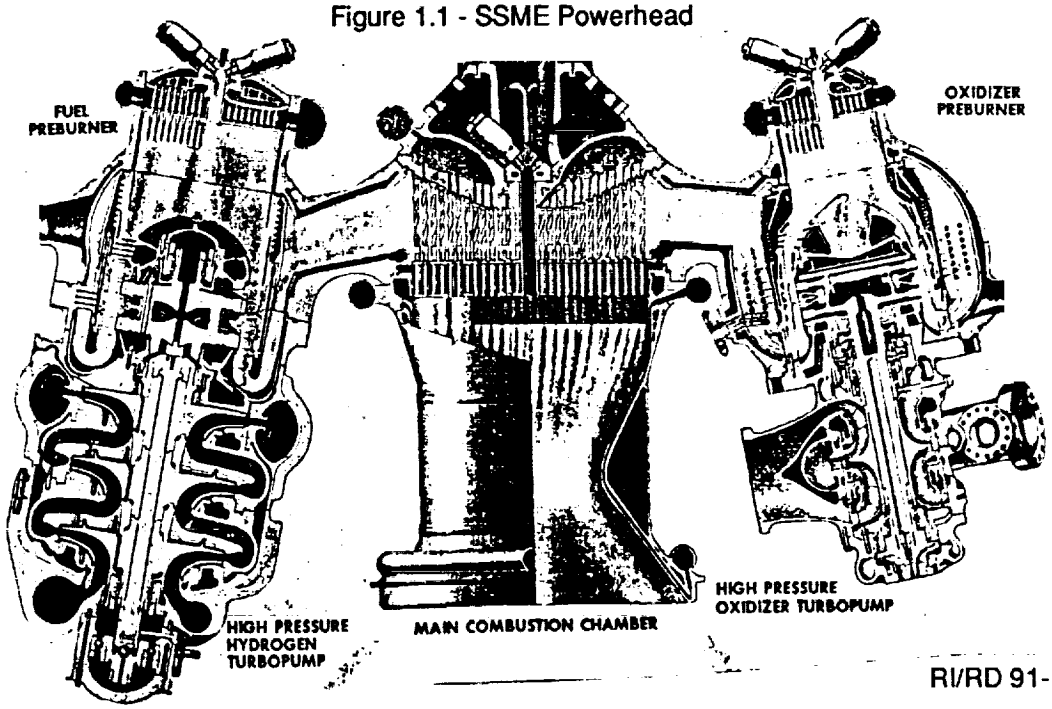

RI/RD 91-157

Figure 1.2 - Cutaway view of SSME Hot-Gas Manifold

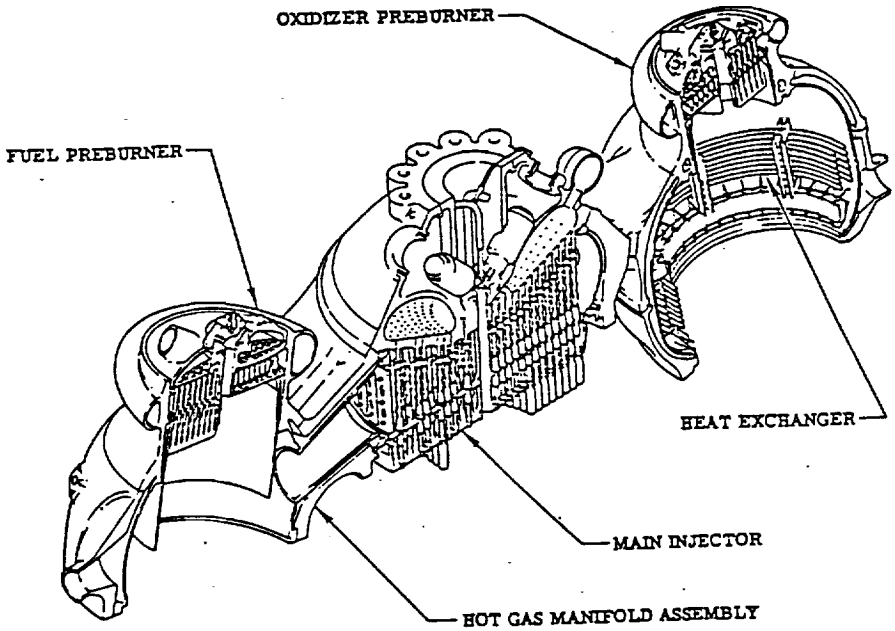

Figure 1.3 - Main Injector Assembly

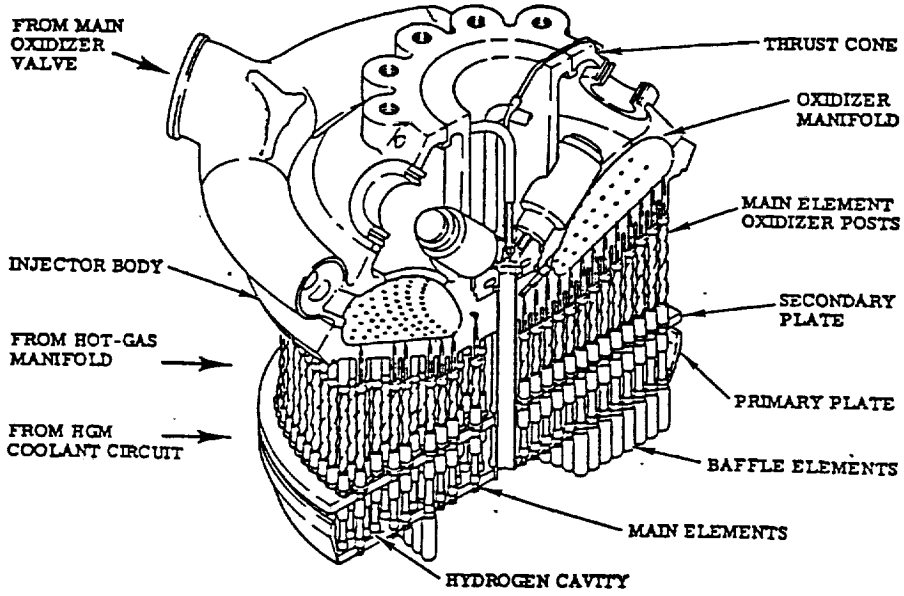

The SSME was designed based on a staged combustion cycle, where the propellants are partially burned within the preburners at low mixture ratio, high pressure and relatively low temperature. The hydrogen-rich combustion products are subsequently used to power the high-pressure turbopumps. The gas exiting each turbine is then routed through axisymmetric 180° turns which lead into the respective fuel and LOX bowls. Transfer ducts from opposite sides connect the fuel and LOX bowls to the main injector torus manifold where the flow enters the main injector array through 600 LOX post injector elements.

As shown in Figure 1.4, the oxidizer (liquid oxygen) flows through the center of each LOX post. The hydrogen-rich hot-gas flowing from the preburners enters a sleeve, coaxial to the injector element, through six 0.140 in. diameter holes located at the secondary plate retainer. Mixing of the hydrogen-rich gas and oxidizer occurs at the primary plate. The resulting combustion produces sufficient pressure in the Main Combustion Chamber (MCC) to provide the required engine thrust. Cooling for the sleeves, primary and secondary plates, and baffle elements is accomplished by pressurizing the space between the two plates with cool hydrogen gas, at a pressure greater than that acting on the opposite side of either plate. Both primary and secondary plates are made of a porous "rigimesh" material, thereby allowing for transpiration cooling to take place.

Figure 1.4 - Detail of Main Injector LOX Post Element

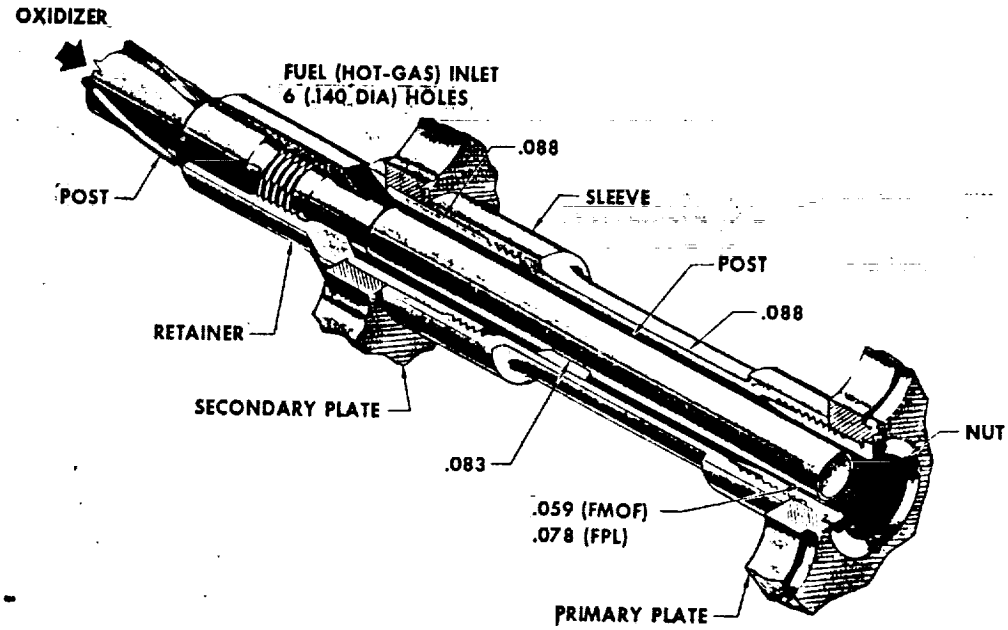

RI/RD 91-157

The powerhead flow path just described, results in a very complex, turbulent and highly three-dimensional flow pattern. The fuel side of the powerhead assembly is subject to greater mass flow rates than the oxidizer side, and thus more likely to induce instability. For this reason, the present study is focused primarily on the fuel side of the powerhead as opposed to the oxidizer side. Some of the more common flow characteristics pertinent to the transfer ducts in the current flight engine configuration are listed in Table 1.1.

MAIN INJECTOR HISTORY

A large amount of effort has been devoted to understanding the flow inside and approaching the main injector elements (LOX posts). The first SSME LOX posts were made of Haynes 188 and were later changed to 316L CRES. Early engine firings (engines 0002 and 0005) employing injectors with CRES posts experienced LOX post failures due to cracking in the thread and tip regions as indicated in Figure 1.5. Figure 1.6 indicates that the LOX post failures occurred in regions of the main injector corresponding to areas on the fuel-side transfer ducts where the discharge velocities are known to be maximum. The main injectors installed on engines 0002 and 0005 had accumulated approximately 780 seconds of equivalent RPL (Rated Power Level, or, 100% Power Level) time at failure.

Table 1.1 - SSME Powerhead Operating Conditions at Transducer Ducts for FPL Baseline Engine Operating at 109% Power Level

PARAMETER	FUEL TRANSFER DUCTS	OXIDIZER TRANSFER DUCTS
FLOW RATE	76.3 kg/s (168.2 Lbm/s)	32.0 kg/s (70.5 Lbm/s)
TOTAL PRESSURE	24.7 MPa (3585 psi)	24.6 MPa (3574 psia)
TEMPERATURE	952 K (1715 R)	786 K(1415 R)
MACH No.	0.11	0.10
DENSITY	11.7 kg/m3 (0.73 Lb/Ft3)	12.5 kg/m3 (0.78 lb/ft3)
AREA	0.0368 m2 (0.396 Ft2)	0.0165 m2 (0.178 ft2)
VELOCITY	176.5 m/s (579.2 Ft/s)	155.0 m/s (508.6 ft/s)
MOLECULAR WGHT	3.83 kg/kg-m (3.83 lb/lb-m)	3.47 kg/kg-m (3.47 kg/kg-m)
REYNOLDS No.	8.5E+7/m (2.6E+7/ft)	9.2E+7/m (2.8E+7/ft)

Figure 1.5 - LOX Post Failures for Engines 0005, 0002, and 2004

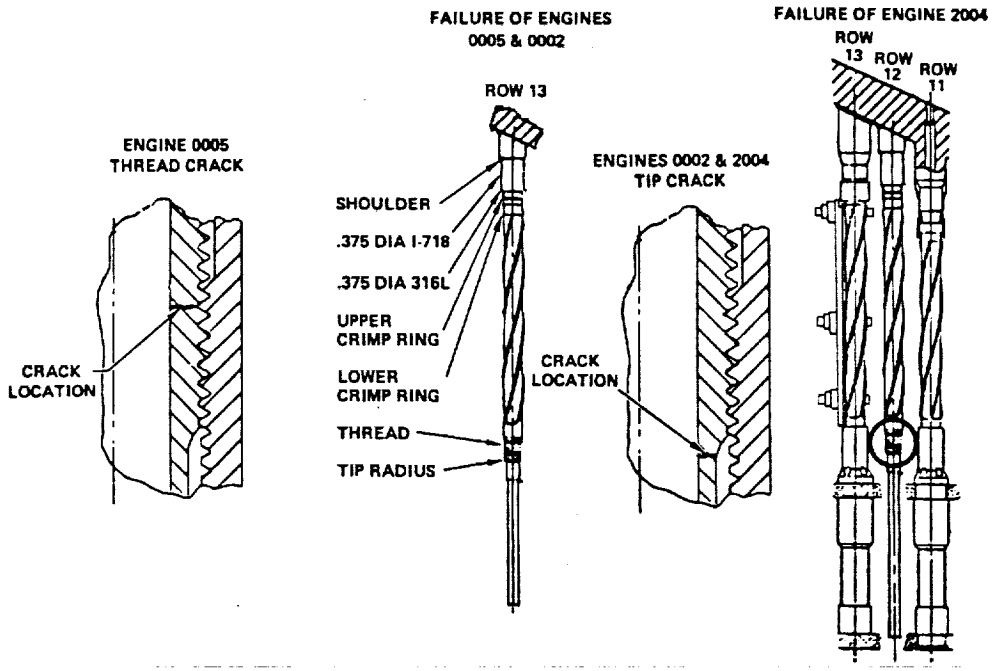

Figure 1.6 - Main Injector Failures for Engines 0002, 0005, and 2004

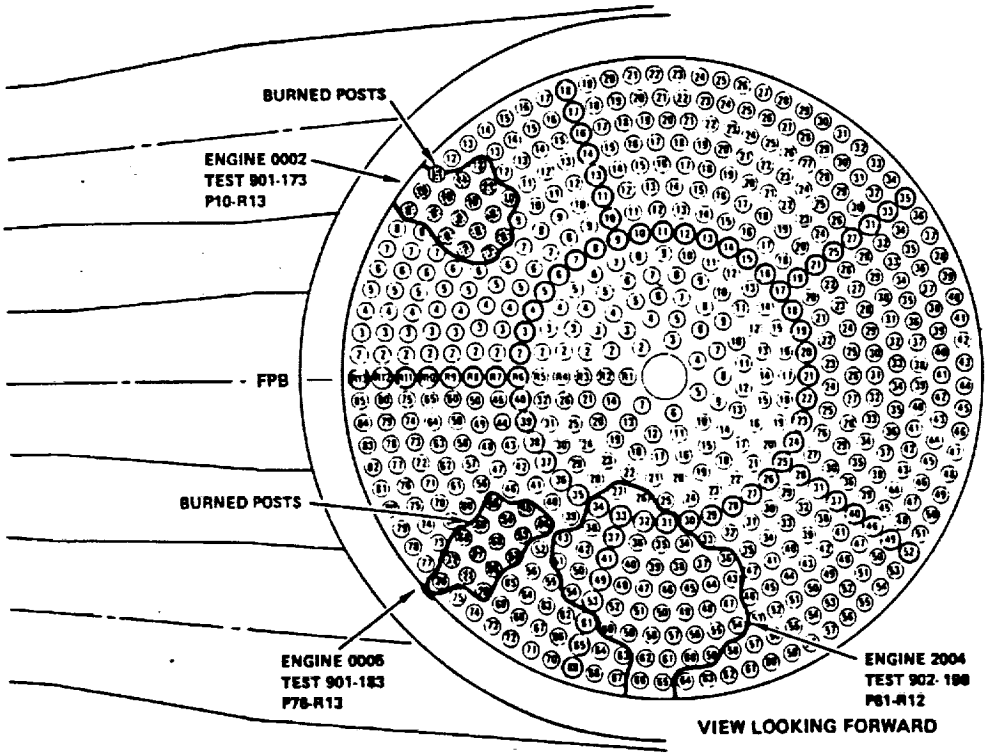

Flow shields were added to later main injector configurations in an effort to increase the stiffness of the LOX posts; Figure 1.7 illustrates the assembly of flow shields to row 13 of the main injector. At approximately 20,000 seconds equivalent RPL time, the shielded injector on engine 2004 experienced failure in a row 12 LOX post in the tip region (see Figure 1.5). Following that incident, most injectors with CRES LOX posts were modified with Haynes 188 tips, and all future injectors had LOX posts built entirely of Haynes 188. Two latter engines, 2108 and 0110, both of which had some run time at Full Power Level (FPL, or 109% power level), experienced failures as a result of cracks developed in the inertia weld region (Figure 1.8). Such cracks occurred after approximately 2800 seconds of equivalent FPL time. Recent design considerations for the main injector have been the use of unshielded "super-posts". Super-posts are made of Haynes 188 and have slightly larger diameter than the baseline LOX posts currently used on flight engines. A comparison between the two posts is made in Table 1.2.

Figure 1.7 - Example of Shielded LOX post

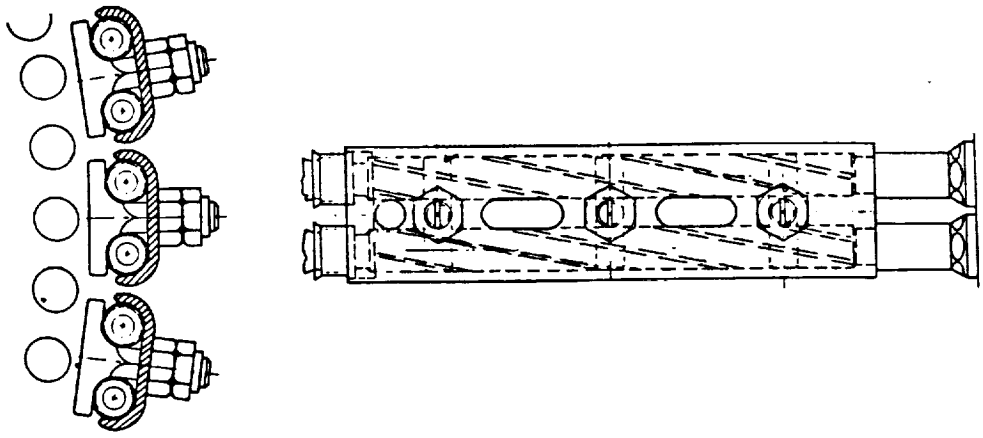

Figure 1.8 - Inertia Weld Cracks for Engines 2108 and 0110

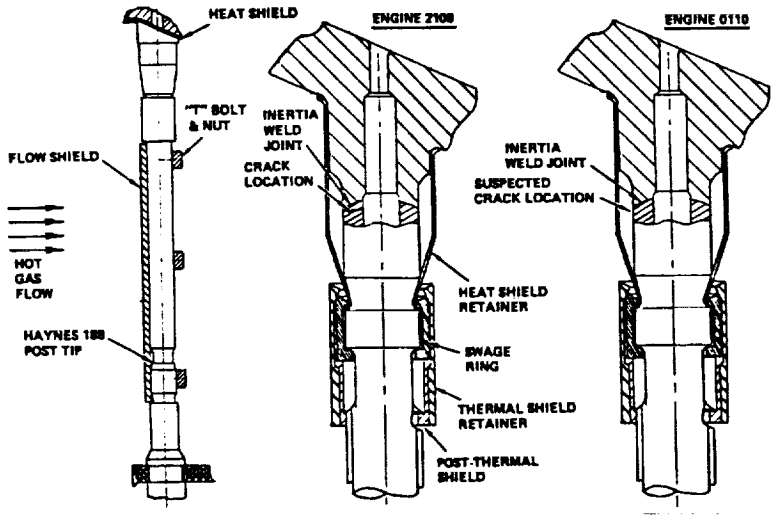

RI/RD 91-157

Table 1.2 - Comparison of Flight and Superpost LOX Posts

PARAMETER	FLIGHT	SUPERPOST
DIAMETER(INCL. SWIRLER)	0.94 cm (0.371 in)	0.986 cm (0.388 in)
MASS/LENGTH	0.3518 kg/m (0.2364 Lbm/Ft)	0.4161 kg/m (0.2796 Lbm/Ft)
NATURAL FREQUENCY	1640 Hz	1840 Hz
MATERIAL	CRES 316L/ HAYNES 188	HAYNES 188

Efforts to improve the SSME powerhead overall system pressure loss, lower operating temperatures and LOX post environment, have resulted in the consideration of a major design change in the HGM. Extensive testing and analysis have been performed on a hot gas manifold design consisting of two large diameter fuel side transfer ducts in place of the current three transfer duct design. Engine prototypes equipped with two-duct hot gas manifold have been built and are currently undergoing an extensive test firing program.

AIR FLOW TESTS

Air flow testing of full-scale SSME hardware has been an important method for understanding the powerhead flow field and for testing new design concepts. Several tests have been conducted at Rockwell's North American Aircraft Operations (NAAO) Division in El Segundo, California. Recently, a new test facility featuring a modular and extensively instrumented HGM model has attained operational status at the Aerophysics Laboratories of Marshall Space Flight Center in Huntsville, Alabama. The experimental phase of this study has been carried out at the latter test facility. A detailed description of this test facility is given in the Test Facility section of this report.

Earlier full-scale test models tested at NAAO include a "solid-wall" three-duct hot-gas manifold (SWHGM) machined out of CRES, an actual three-duct SSME hot-gas manifold modified to a two-duct design (Technology Model), and a more refined Phase III two-duct HGM model machined from CRES. All of the HGM test models contain hardware for the simulation of the fuel and oxidizer turbine discharge ducts. Main injectors used in the models are actual SSME injectors

modified to meet the requirements of the respective test programs. All models were equipped with digital and high-frequency instrumentation. Additional Information on two-duct and three-duct air flow tests conducted at NAAO can be found in Reference 1.

Air flow tests conducted at all test facilities described above typically consist of a 30-second duration blowdown of ambient temperature air compressed to 2.27 MPa (330 psia). Mass flow rates achieved during testing are nominally 45 kg/sec (100 Lbm/sec). This represents approximately 70% of the engine operating Reynolds number, which is in the highly turbulent regime and thus constitutes an accurate simulation. Both the SSME and air flow test models operate at a sufficiently low Mach number for the flow upstream of the injector to be considered incompressible.

FLOW-INDUCED VIBRATION MECHANISM

The three principal mechanisms typically associated with flow-induced vibration of cylindrical tubes in a closely packed array are:

1. Turbulence
2. Vortex shedding
3. Fluidelastic excitation (self-excited motion)

The independent dimensionless similitude parameters usually considered in flow induced vibration investigations are shown in Table 1.3. Case 1 is the general formulation. Note that vibration does not generally take place at the natural frequency fn. In compressible flow the dependent variables, y/D, for example, can be written as a function of four independent parameters:

$$\frac{y}{D} = \phi\left[\frac{\rho U D}{\mu}, \frac{f_n D}{U}, \frac{m_e}{\rho D^2}, \delta_n\right] \qquad (1)$$

In Case 2, excitation occurs at the fundamental natural frequency and, for incompressible flow:

$$\frac{y}{D} = \phi\left[\frac{\rho U D}{\mu}, \frac{f_n D}{U}, \frac{m_e \delta_n}{\rho D^2}\right] \qquad (2)$$

Table 1.3 - Similitude Parameters Associated With Flow-Induced Vibration Phenomena

CASE 1 - GENERAL FORMULATION					
1.	$\frac{\rho UD}{\nu}$	(Reynolds Number)	4.	$\frac{K}{\rho U^2 D}$	(Fluidelastic Parameter)
2.	$\frac{U}{a}$	(Mach Number	OR	$\frac{U}{f_n D}$	(Reduced Velocity)
3.	$\frac{m_0}{\rho d^2}$	(Mass Ratio)	5.	$\frac{C}{\rho U D^2}$	(Damping Variable)
or	$\frac{\rho_s}{\rho}$	(Density Ratio)	OR	δ	(Logarithmic Decrement)
			6.	$\frac{gD}{U^2}$	(Froude Number)

CASE 2 - VIBRATION AT THE SYSTEM NATURAL FREQUENCY WITH NO GRAVITY OR COMPRESSIBILITY EFFECTS		
1.	$\frac{\rho UD}{\nu}$	(Reynolds Number)
2.	$\frac{U}{f_n D}$	(Reduced Velocity)
3.	$\frac{m_0 \delta_n}{\rho D^2}$	(Damping Parameter)

Turbulent Excitation

Turbulence causes narrow-band random vibration of tubes in a cross-flow at about their natural frequency. Resulting vibration amplitudes vary randomly in time and space (Figure 1.9). Turbulence is believed to be the main cause of tube vibration in heat exchangers when the possibility of fluidelastic excitation is inapplicable.

A semi-empirical formula was derived by Connors (Ref.2) for predicting turbulence induced tube vibration using concepts presented by Fung (Ref.3) and Keefe (Ref.4) for a single-span cylindrical tube:

$$\frac{y_n}{D} = C_1 \left(\frac{\rho_o D^2}{m_o}\right)\left(\frac{U}{f_n D}\right)^{\frac{H+3}{2}} \sqrt{\left(\frac{1}{\delta_n}\right)\left(\frac{D}{L}\right)} \qquad (3)$$

where:

y_n = root-mean-square (RMS) vibration amplitude in the n^{th} mode

C_1 = empirical constant related to the magnitude and spatial correlation of the excitation forces

H = empirical constant related to the shape of the power spectral density (PSD) curve for the excitation forces.

Typically, $0 < H < 3$, and H and C1 depend on the tube pattern and spacing. The purpose of providing Equation (3) is to identify the main parameters associated with turbulence-induced excitation of cylindrical tubes. For tubes with multiple supports subject to spanwise flow variations, a somewhat more complicated formulation is to be employed.

Figure 1.9 - Typical Vibration of a Tube Excited by Turbulence in a Cross-flow:
(a) Typical Lissajous diagram of tube mid-span amplitude;
(b) amplitude histogram for transverse (y) direction;
(c) amplitude histogram for streamwise (x) direction.

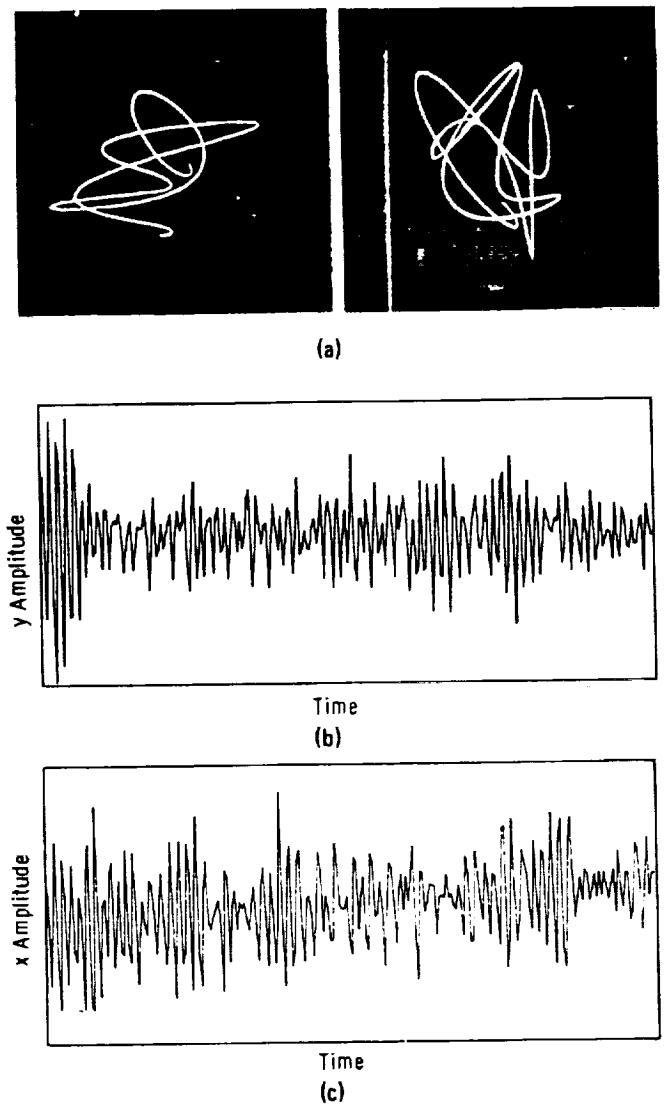

Vortex Shedding

When fluid flows across a circular cylinder, the wake behind the cylinder is characterized by a series of vortices, known as the von Karman Vortex Street. The vortices are shed in a periodic or wide-band random fashion, depending on the Reynolds number, and produce an alternating "lift" force in a direction normal to the flow. The frequency of the alternating force is related to the Strouhal number:

$$f_s = S\left(\frac{U}{D}\right) \qquad (4)$$

where

f_s = vortex shedding frequency

U = approach flow velocity

D = cylinder diameter

S = Strouhal number

The alternating force is associated with the vortex shedding frequency when lock-in is achieved by means of synchronization between the vortex shedding frequency and the tube's natural frequency. Methods are available (Ref.5 through 7) for predicting tube vibration caused by vortex shedding. However, the practical importance of vortex shedding excitation in closely packed arrays is questionable. Vortex shedding excitation has been observed in laboratory tests on tube arrays in uniform cross-flow at relatively low Reynolds numbers. A number of factors tend to reduce the importance of vortex shedding in the SSME:

1. Spanwise variations in flow velocity known to exist in prototype situations reduce the strength of vortex shedding. For example, no evidence of vortex shedding was observed in tests of the inlet region of a Canadian recirculation-type steam generator (Ref. 8).

2. It is likely that vortex shedding excitation is diminished at the higher Reynolds Number that exist at SSME operating conditions.

3. Turbulence in the flow approaching a single tube (Ref. 9)or an array (Ref. 10) may suppress vortex shedding.

4. Helical strakes, such as those on the SSME injector LOX posts, are known (Ref. 11) to suppress vortex shedding.

Fluid-elastic Excitation

Vibration amplitudes associated with vortex shedding and/or turbulent excitation do not usually exceed approximately 20% of the cylinder's diameter (Ref. 7). Larger amplitudes, that have often resulted in rapid deterioration of heat exchanger tubes, have been determined to be induced by fluidelastic excitation. This phenomenon is a self-excited vibration mechanism (Ref. 12)[1], first identified by Westinghouse. The similarity of the SSME main injector LOX post array to the tube arrays found in heat exchangers that have been affected by fluidelastic excitation, makes it reasonable to believe that the potential may exist for fluidelastic excitation to be present in the SSME. The mechanism is characterized by a critical flow velocity below which vibration amplitudes are small, and above which the amplitudes increase very rapidly (Figure 1.10). It is this fact, coupled with the preceding observations, that make the fluidelastic excitation mechanism by far the most critical of the three previously listed flow-induced vibration mechanisms.

The time history of the structural response due to fluidelastic excitation is sinusoidal; it occurs at the natural frequency of the tubes in a cross flow. The tubes vibrate in orbital patterns, as shown in Figure 1.11. The large amplitude vibration initiates when[2]:

$$U_{en} > \beta f_n D \sqrt{\left(\frac{m_o \delta_n}{\rho_o D^2}\right)} \qquad (5)$$

where

U_{en} = effective velocity

β = threshold instability constant (dependent on tube pattern and spacing)

f_n = tube natural frequency in the n'th normal mode

D = tube diameter

The threshold instability constant has been evaluated experimentally for several tube patterns and tube spacings. The tube's structural damping, expressed as a logarithmic decrement δ_n, includes mechanical damping as well as fluid damping. Damping is presently not well defined. Usually values of δ_n between 0.0628 and 0.1257 are used in design (1% to 2% critical damping). The relation given in Equation 5 is often displayed in a stability diagram as shown in Figure 1.12(a).

---

[1] A Comprehensive literature survey is not provided in this report; extensive bibliographical references may be found in Refs. 13 and 14.

[2] Note that the formulation of equation 5 corresponds to Case 2 in Table 1.3, while the formulation of equation 6 corresponds to Case 1.

Figure 1.10 - Detection of Onset of Instability Based on Vibration Amplitude Variation with Increasing Flow.

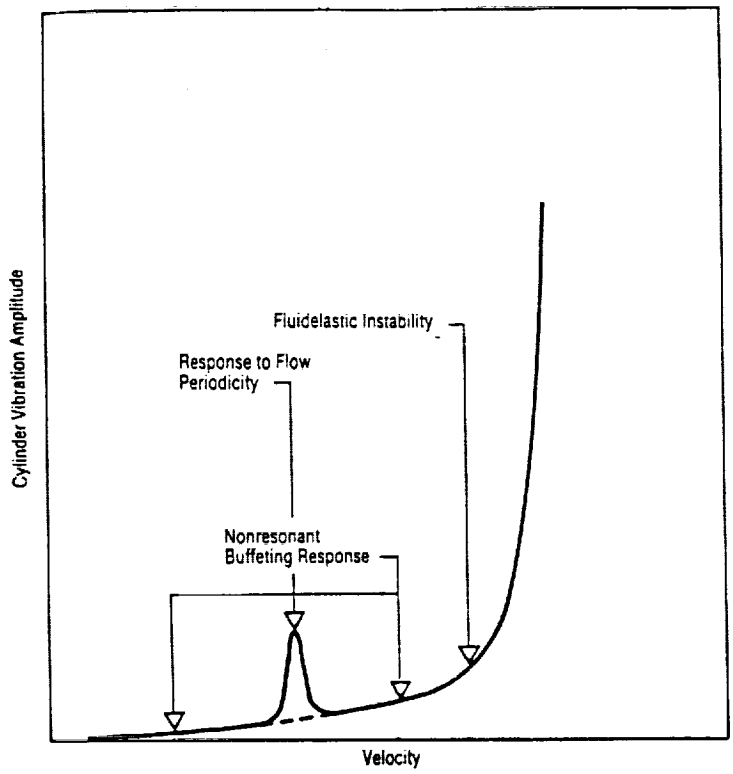

Figure 1.11 - Typical Whirling Vibration of Rods in a Square Array. Lift direction is Vertical and Drag Direction is Horizontal (flow is left to right).

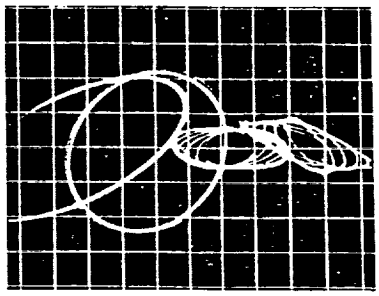

Vibration patterns for shaded tubes,
0.15 mm per division.
Tubes are not hitting, and the physical
tube orbits do not overlap.

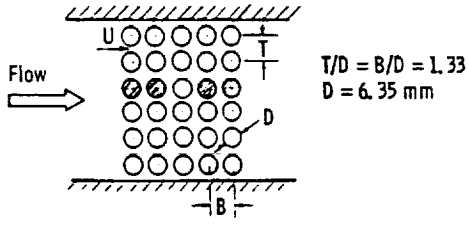

Figure 1.12 (a) - Stability Diagram for Three Row Square Array with T/C = B/D = 1.41

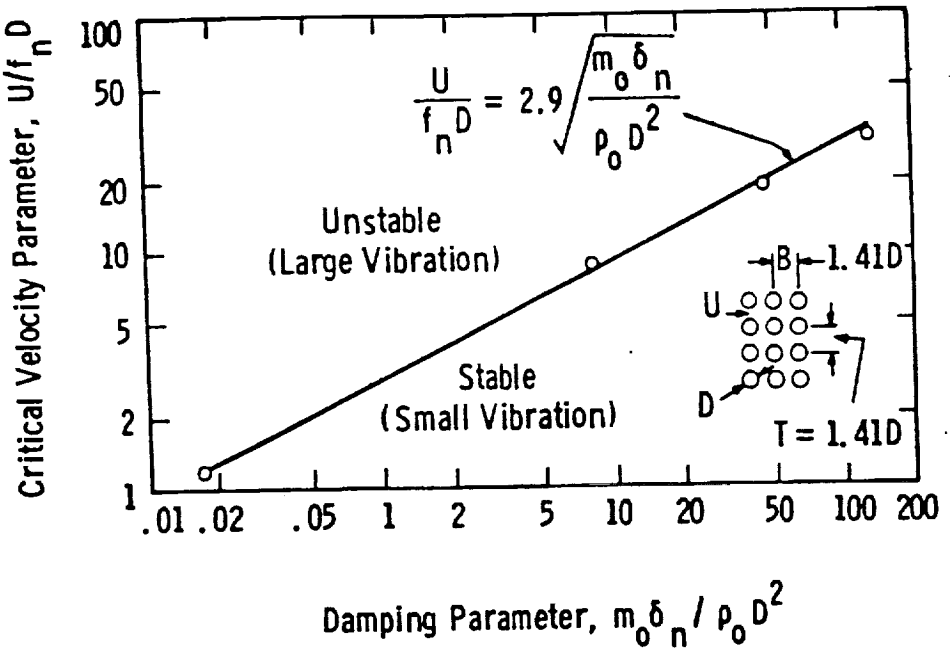

Figure 1.12 (b) - Traditional Plot for the Threshold Fluidelastic Instability Based on the Work of Various Researchers

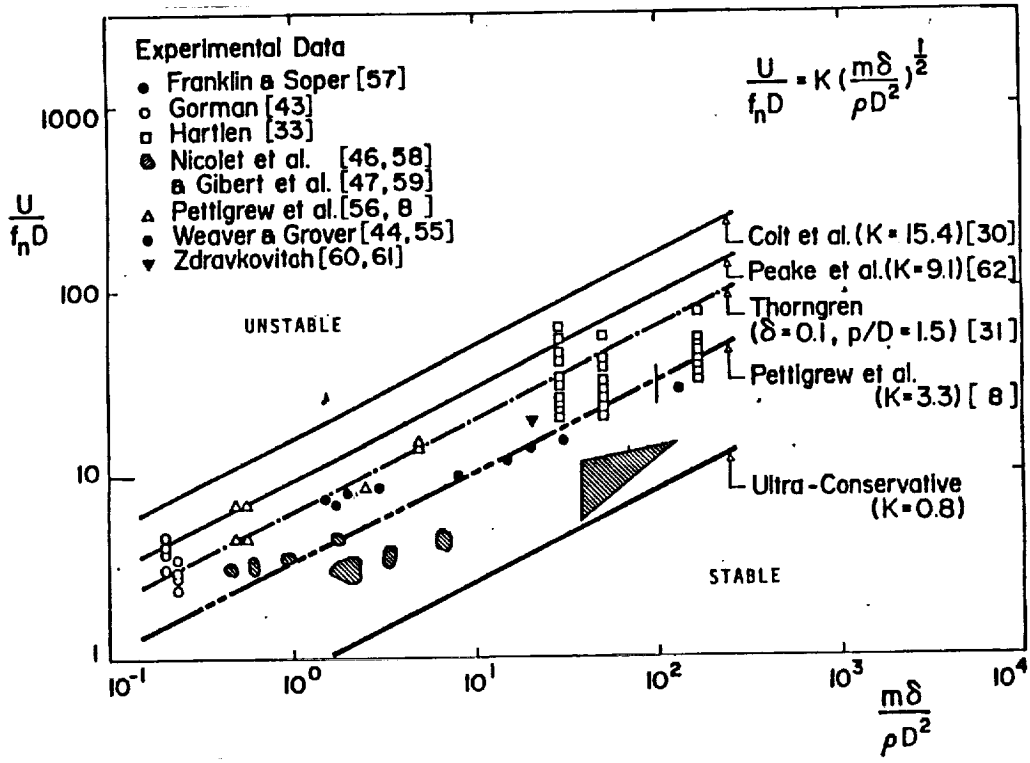

The diagram shows, among other things, that higher flow velocities are required to cause tube whirling for low density fluids such as gases, than for high density fluids such as water when all other parameters are held constant. Figure 1.12(b) is the traditional plot for the instability threshold as viewed by several investigators.

Current research (Refs. 13 and 14) suggests that the onset of fluidelastic instability may be more generally predicted by:

$$U_{en} > \beta f_n D \left(\frac{m_o}{\rho_o D^2}\right)^{\Gamma} \delta^{\gamma} \qquad (6)$$

where Γ and γ depend on whether the fluid density is low (gas) or high (liquid). For the conditions existing in the SSME, Eq. 5 is believed to be appropriate, and values of β are obtained from the experimental data using the relationship given in Eq. 5. It is also noted that Eq.5 is generally accepted as being valid for gaseous flows in the operating range of the SSME, while Eq. 6 has been proposed for liquid flows.

For nonuniform flows, the effective velocity in Eq.5 depends on the spanwise velocity and density distribution, as well as on the mode shape of vibration[3] . The effective velocity is given by (Ref. 15):

$$U_{en}^2 = \frac{\sum_{j=1}^{N} \left(\frac{\rho_j}{\rho_o}\right) U_j^2 \phi_{jn}^2 \Delta Z_j}{\sum_{j=1}^{N} \left(\frac{m_j}{m_o}\right) \phi_{jn}^2 \Delta Z_j} \qquad (7)$$

where U_j , ρ_j and m_j are the velocity, fluid density, and tube incremental mass at various spanwise locations along the tube, respectively, and ϕ_{jn} is the normalized displacement of the j^{th} lumped mass in the n'th mode of vibration.

Most of the investigations reported in the literature involve flows that are essentially uniform in the transverse direction. However, flowfields with highly nonuniform velocity distribution in the transverse direction exist in many types of heat exchangers. Of particular interest are skimming flows created, for example, in the vicinity of inlet nozzle impingement plates. The impingement plate turns the nozzle flow and creates a high tangential skimming velocity between the shell and tube bundle as shown in Figure 1.13.

---

[3] The mode shapes and natural frequencies can be calculated using finite-element computer programs such as NASTRAN and WECAN.

Figure 1.13 - Skimming Flow Developed in the Vicinity of an Impingement Plate in a Heat Exchanger.

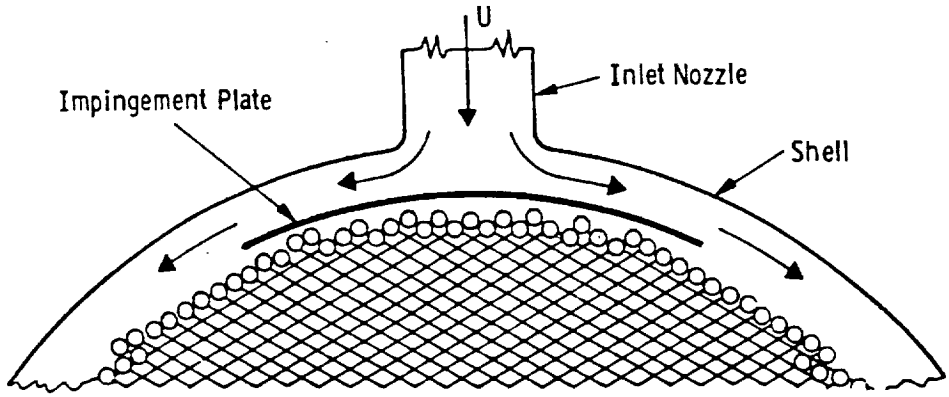

An experimental investigation of flow-induced vibration of tube arrays in highly nonuniform cross flow was conducted by Westinghouse (Ref. 16). It was found that skimming flows cause large amplitude fluidelastic vibration of tubes in model arrays when the velocity exceeds the threshold value. Figure 1.14 shows a typical test configuration, while Figure 1.15 shows the variation of the threshold instability constant with geometry of the flow passage. It is believed that skimming flows similar to those discussed above are the likely cause of the large-amplitude flow-induced tube vibration reported (Ref. 17) for a single pass steam generator.

It is believed that the flowfield in the SSME main injector region is such that the LOX posts may be subject to both cross flow and skimming flow conditions. As will be discussed in a later section in greater detail, the main injector tested in the course of this study is instrumented in such a manner that detection of instability for both flow conditions should be feasible.

Investigations on the effects of impinging jets on the flow-induced vibration of tube arrays has also been carried out at Westinghouse. Figure 1.16 shows fluidelastic excitation of tubes caused by a jet directed between two columns of tubes. This situation is believed to be similar to the SSME injector inner rows, when shields are installed on the outer row.

Figure 1.14 - Vibration of Tubes Located in a Triangular Array Caused by a Tangential Skimming Flow. (Lift Direction is Vertical and Drag Direction is Horizontal.
1 inch = 25.4 mm, 1 fps = 0.3048 m/s)

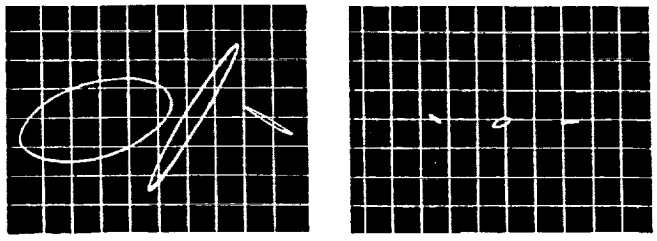

(a) Tubes 2, 3, 4. U = 27.5 fps
.023 in./div.

(b) Tubes 7, 8 9. U = 27.5 fps
.023 in./div.

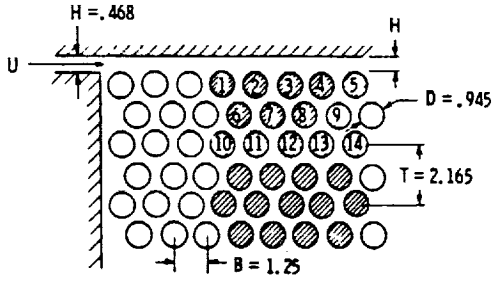

Figure 1.15 - Threshold Instability Constant for Skimming Flow Over a Triangular Array.
(1 inch = 25.4 mm)

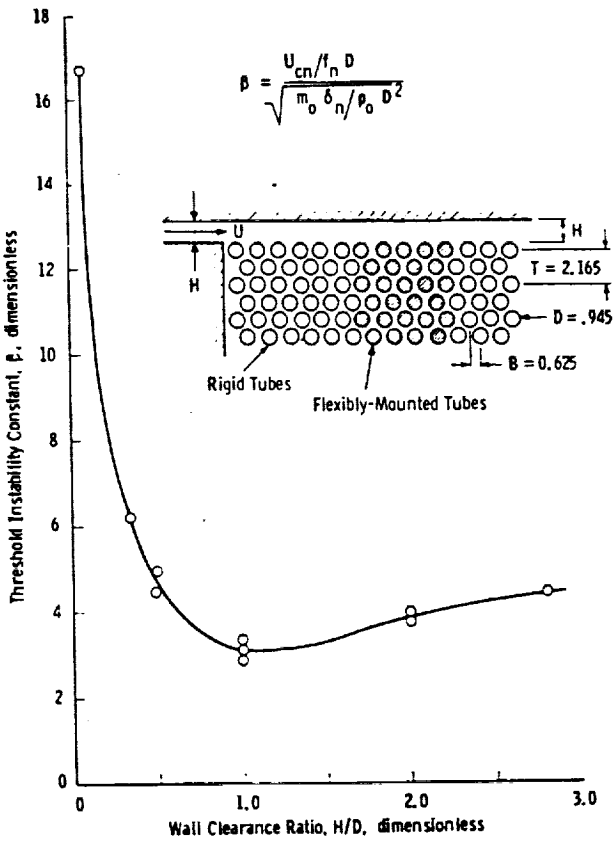

Figure 1.16 - Vibration of Rods 1, 2, 3, and 4 Caused by Jet flow. Vibration orbits are steady. Vibration frequency occurs in the 43.4 Hz fundamental mode.

(a) V = 5.0 fps . .020 in./div.

(b) V = 6.1 fps . .020 in./div.

(c) V = 7.25 fps . .020 in./div.

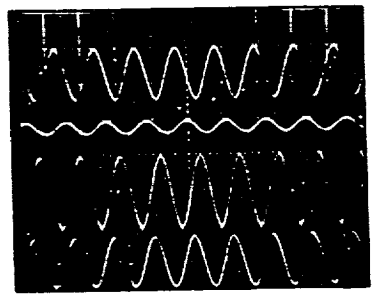

(d) V = 7.25 fps . .050 in./(vert. div.), .02 sec/(hor. div.)
Traces 1, 2 for rod 2 in jet and transverse directions respectively.
Traces 3, 4 for rod 3 in jet and transverse directions respectively.

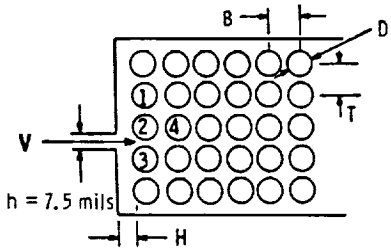

Unbounded Jet Directed between Rods 2 and 3.
B/D = 1.33, T/D = 1.33, H/D = 0.80, D = 0.250

PREVIOUS EXPERIMENTAL WORK

Motivated by plans to hot fire an SSME equipped with an unshielded superpost injector (engine 0208), air flow tests were carried out in 1984 at Rocketdyne by L.K.Sharma and S.T.Vogt. The objective of this air flow test program was to determine whether LOX post instability would occur on technology engine 0208 at 109% power level. Testing was carried out on two test stands: channel tests were conducted on an array with a uniform approach flow, and two-duct HGM tests were conducted at the highest flowrates achievable at the NAAO test facility. It is interesting to note that the test results indicated an unstable condition for the LOX posts in the channel tests, however the two-duct tests showed all instrumented posts to remain quite stable over the entire achievable flowrate range.

Channel Tests

The initial channel stability test phase was conducted using one of three available array geometries. Seventy-seven tests were conducted over a wide range of channel mass flowrates and pressures to obtain the stability boundary and a map of injector stability regions in terms of reduced velocity and damping parameter. Figure 1.17 shows the superpost array geometry and the various array configurations used. Instrumented Vespel posts had four mutually orthogonal strain gages located at the mid-span position along each LOX post. Non-instrumented Vespel posts and aluminum posts were used to provide the appropriate array blockage, and determine the effect of different neighboring posts on fluidelastic excitation.

Testing was carried out at channel velocities large enough to prevent interference from vortex shedding excitation at the post element natural frequency. Typical values of the Strouhal shedding frequency were 2 to 4 times greater than the Vespel post natural frequency. In a number of test runs, the LOX post strain and deflection behaved non-linearly with respect to increasing approach flow velocity head (q). Figure 1.18 shows the post response for runs 1, 2 and 12. As the figure shows, the LOX post strain response behaved linearly with respect to the approach flow velocity head for values of q less than 13.8 KPa (2 psi). At larger values of q the LOX post strain increased exponentially, thus indicating occurrence of fluidelastic instability.

Figure 1.17 - Array Configuration for Air Flow Channel Tests

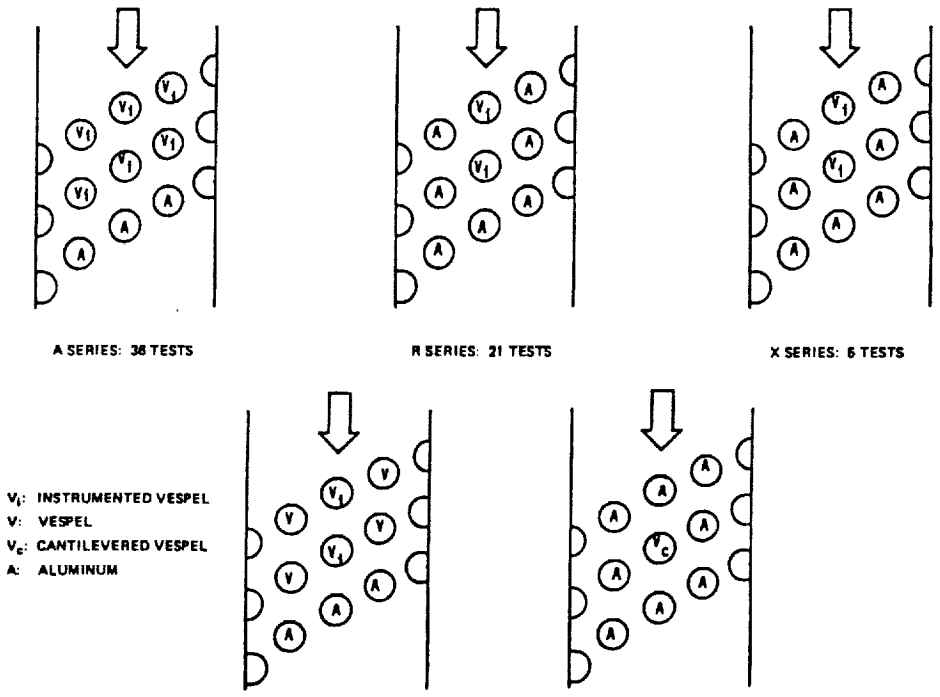

Figure 1.18 - LOX Post Strain Response in Channel Flow Tests

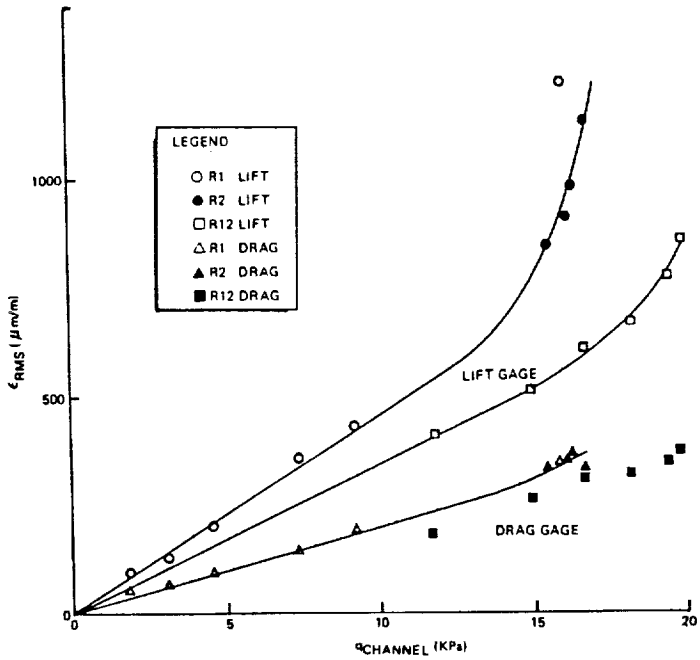

Lissajous diagrams of the strain response confirm this conclusion. In Figure 1.19, the x and y axes represent the LOX post strain response in the drag and lift directions, respectively. As is evident from the illustrations, the first four frames show the orbits as not being well defined, and their amplitudes increase in a linear fashion with the velocity head q; in the fifth frame (q = 15.65 KPa (2.27 psi)), the strain amplitude in the y-direction (lift) has increased nearly 7 times for a twofold increase in q, and the orbit exhibits large elliptical motions, thus indicating fluidelastic instability.

Selected data from the initial stability tests have been plotted in terms of the reduced velocity and damping parameter in Figure 1.20. The data points are differentiated in terms of stable test points, unstable test points, and the location of engine 0208 predicted from three-duct air flow tests and scaled to 120% power level. Uncertainty limits have been placed on most of the data points from the preliminary tests. The lower and upper boundary of the instability thresholds were located based on data points shifted in such a manner as to correspond to the largest and smallest damping parameters possible. Figure 1.21 is an adaptation of Figure 1.20 as it is foreseen that it would apply to SSME operating conditions, and shows the resulting stability limits as they would apply for best and worst case damping. Note that the best estimate for the position of an engine is in the region labeled "possibly unstable". Uncertainty associated with the data used for calculating the non-dimensional parameters in the chart, leads to lack of confidence in the resulting stability boundary.

The largest degree of uncertainty is encountered with the logarithmic decrement (δ). This applies to LOX posts installed on the engine as well as on the air flow test models. Much of this uncertainty results from the difficulty in measuring and/or calculating the damping of a LOX post on an engine during hot-fire operation, or during air flow tests. A second major source of uncertainty is predicting the gap velocity between LOX posts due to the highly three-dimensional nature of the flowfield. In Figure 1.21, error bands have been placed on the gap velocity for Engine 0208. The lower band is based on the one-dimensional gap velocity, whereas the upper band represents the maximum velocity measured in the transfer ducts, accelerated through the gap area between LOX posts. The gap velocity associated with Engine 0208 was obtained from direct measurement during previous air flow tests and scaled to 109% power level.

In summary, it has been shown that LOX posts can be subject to fluidelastic instability in channel flow test conditions, and with uniform approach velocity distribution. Testing has also shown that the uncertainty in the logarithmic decrement, used to calculate the damping parameter, needs to be further reduced in order to obtain a more realistic picture. Nevertheless, the data presented above clearly reveals the existence of a potential instability situation in the main injector LOX posts. Before assessing this potential in the three-duct superpost injector, we shall first examine the results obtained from the two-duct main injector tests carried in 1984.

Figure 1.19 - Lissajous Diagrams of LOX Post Strain Response

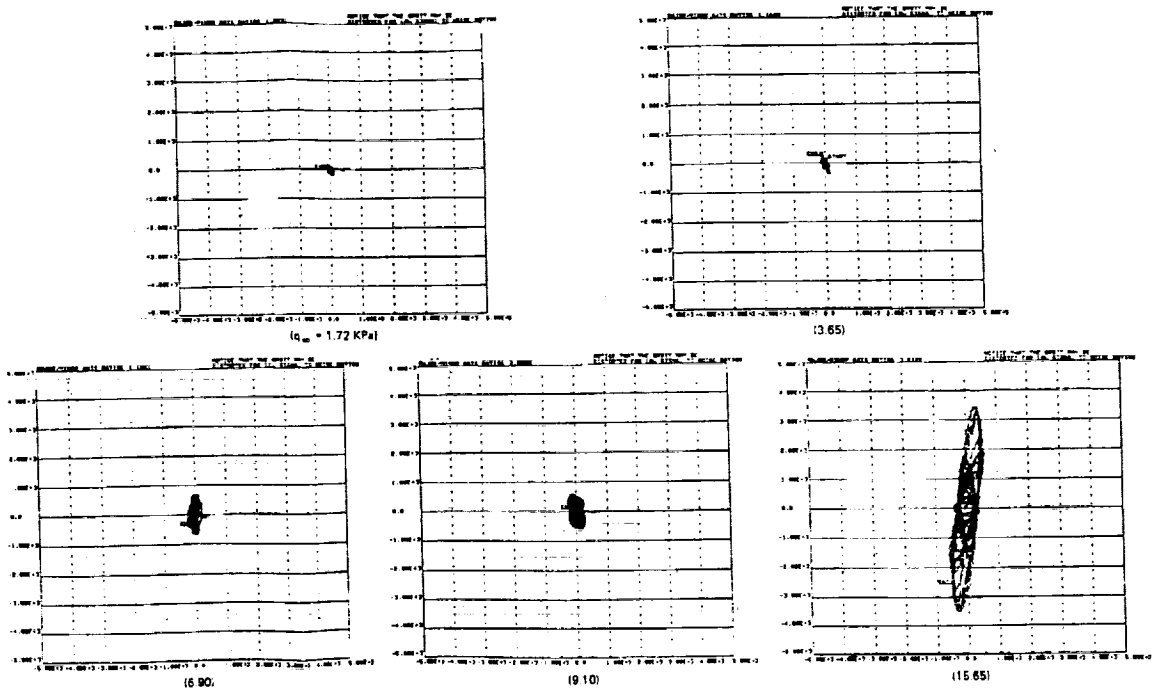

Figure 1.20 - Superpost Stability Parameter Comparison

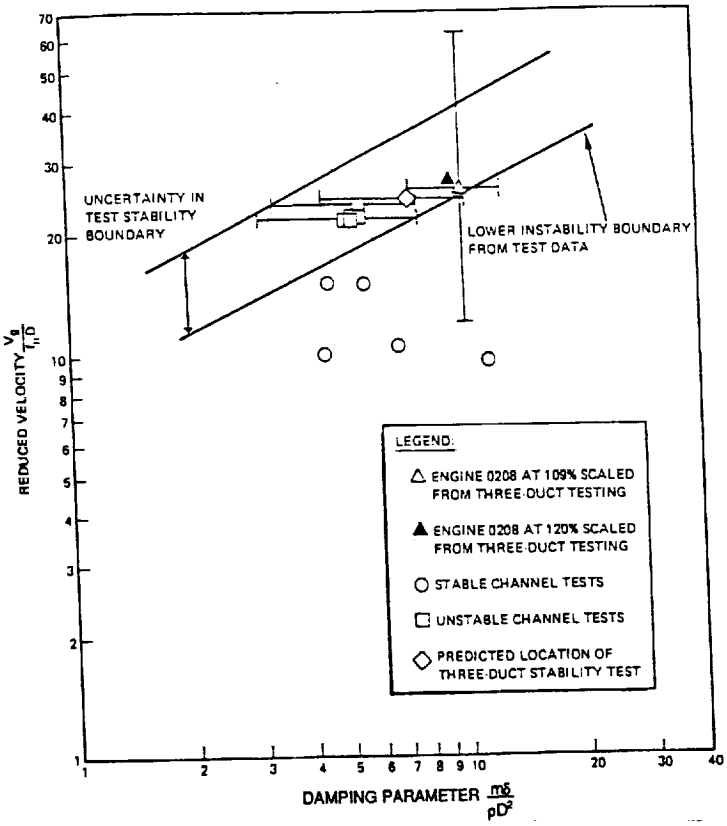

Figure 1.21 - Stability Map Comparison

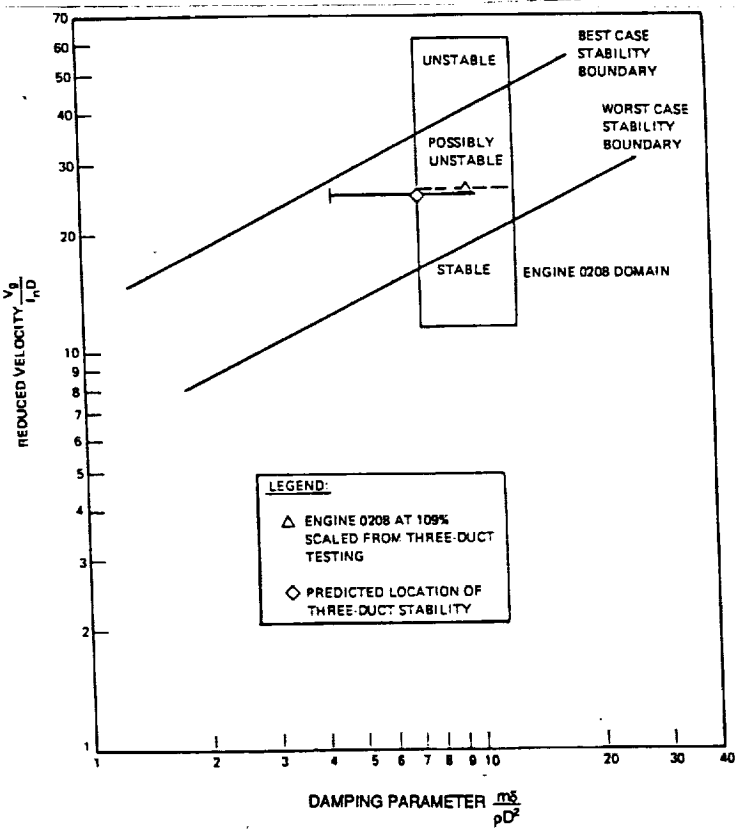

RI/RD 91-157

Two-Duct HGM Tests

Due to unavoidable inaccuracies associated with simulating the SSME injector flow with uniform flow past an array within a channel, stability tests were also on an air-flow main injector equipped with instrumented Vespel LOX posts, as shown in Figure 1.22. The Vespel LOX posts were located on rows 12 and 13 in the portion of the injector adjacent to the inner wall of the right transfer duct. Strain gages were installed 45 degrees left and right of the radially outward position on the row 13 posts. The approach velocity to the instrumented array was increased incrementally until maximum test facility operating conditions were reached. As in the channel tests, the Strouhal shedding frequencies were 2 to 4 times greater than the Vespel post natural frequency. Figures 1.23(a) and 1.23(b) show the behavior of the strain response as a function of the one-dimensional transfer duct velocity head. As the figures indicate, the response is linear, thus suggesting that the mode of excitation is due solely to turbulent buffeting.

The apparent lack of excitation induced by fluid-elastic instability is also confirmed by Lissajous diagrams shown in Figure 1.24. Post instability was not detected in any of the two-duct air flow tests. Due to hardware limitations inherent with the two-duct HGM which control the mass flow rate, as well as facility limitations which control the maximum system pressure, the maximum achievable reduced velocity and damping parameter were limited to values lower than those obtained in the channel flow tests.

Figure 1.25 maps the stability parameters of a two-duct engine with respect to those resulting from the scaled two-duct air flow tests. The reduced velocity coordinate corresponding to the two-duct engine data point was obtained from the one-dimensional fuel side transfer duct velocity. Similar to the channel test data, uncertainty limits have been added to account for the uncertainty of the logarithmic decrement of both engine and model posts. Ultimately, this results in the inability to form a definite conclusion about the stability of the two-duct engine LOX posts.

Figure 1.22 - Instrumented LOX Posts in Two-Duct Air Flow Test Model

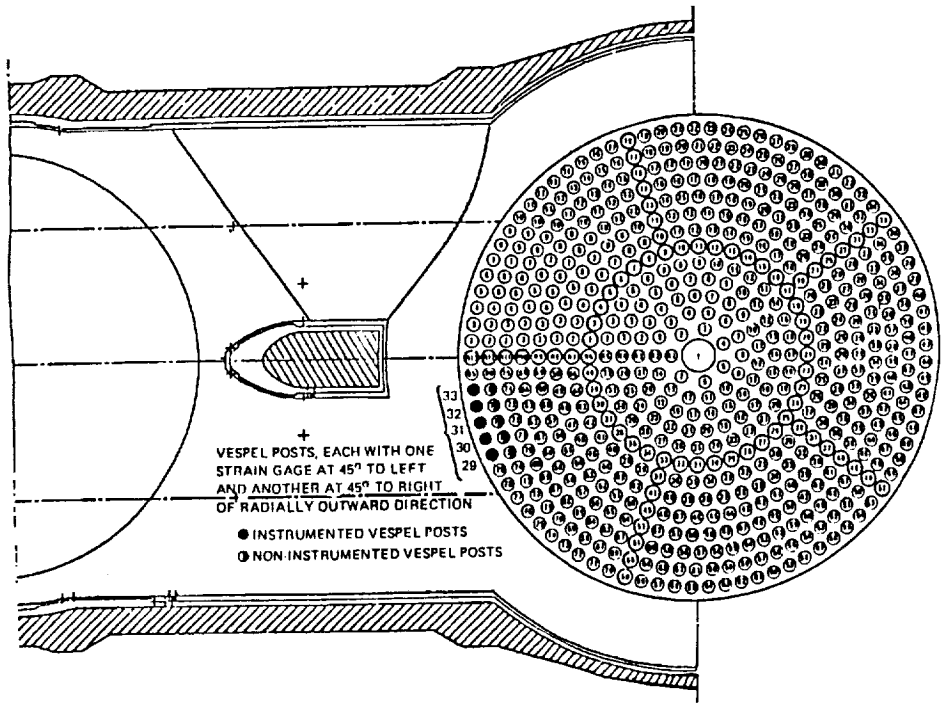

Figure 1.23(a) - LOX Post Strain Response (Right of Radial Direction)

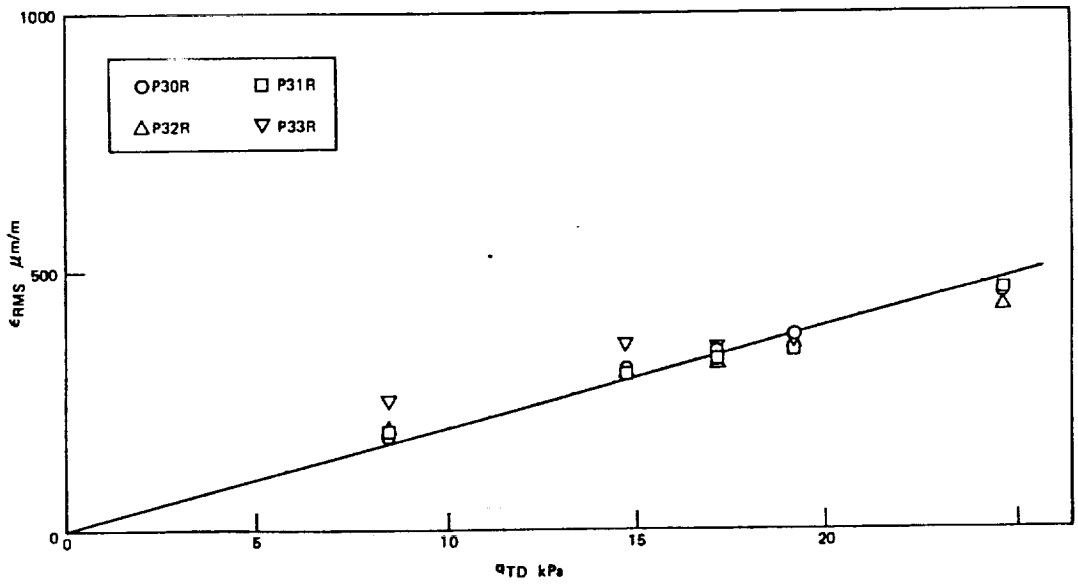

Figure 1.23(b) - LOX Post Strain Response (Left of Radial Direction)

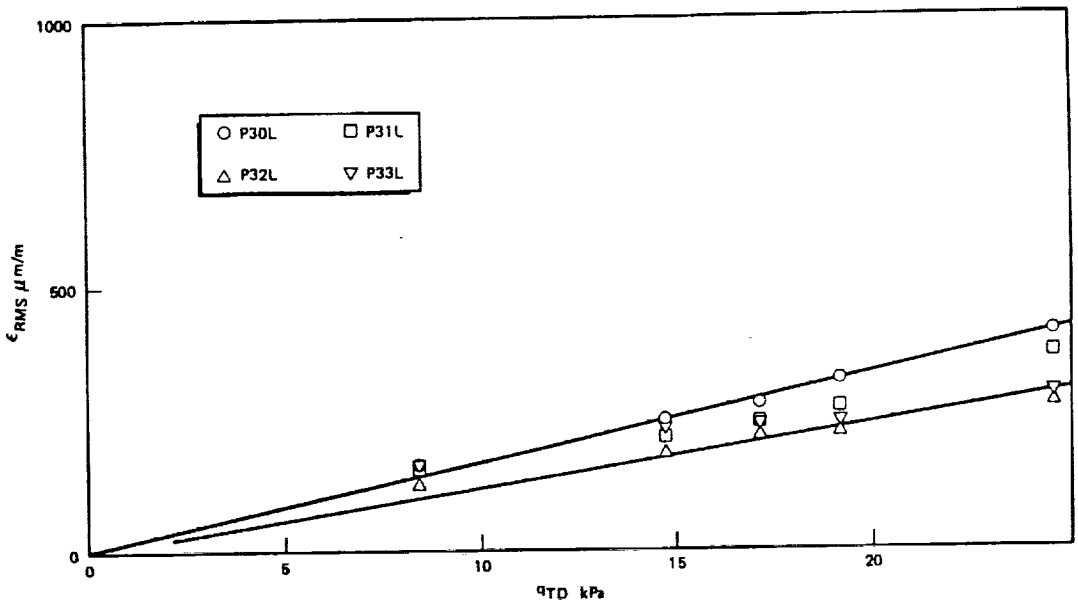

Figure 1.24 - Lissajous Diagrams of LOX Post Strain Response

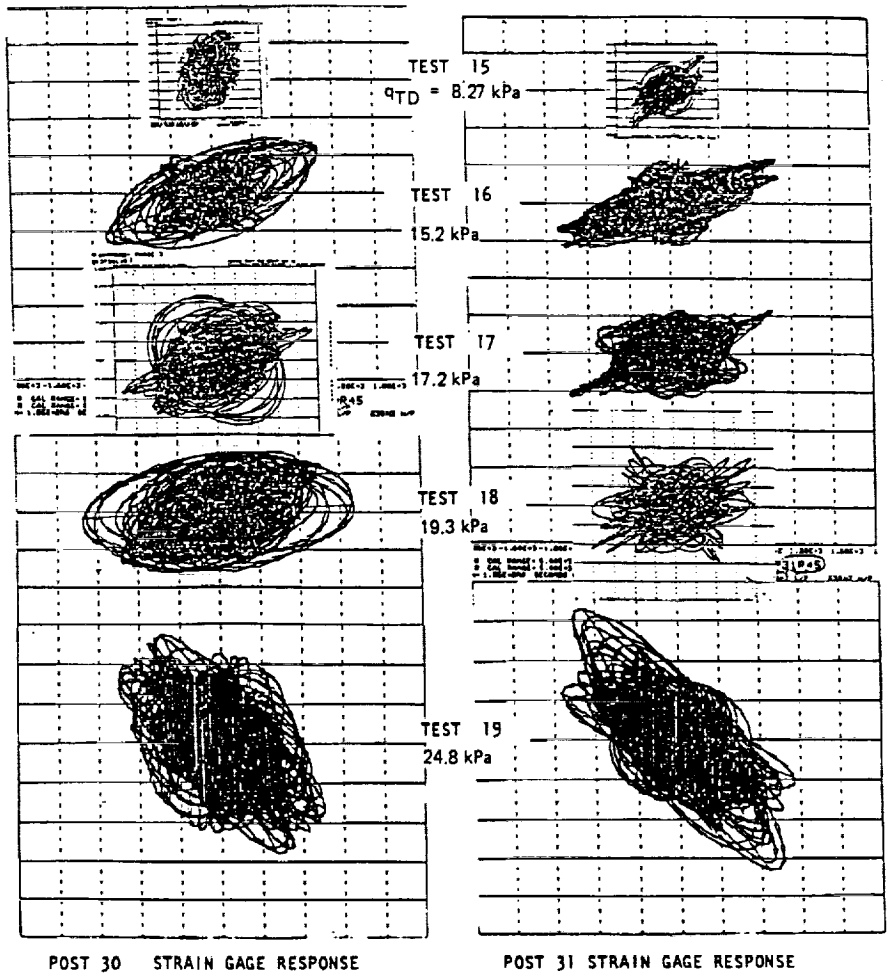

RI/RD 91-157

Figure 1.25 - Two-Duct Air Flow Test Stability Diagram

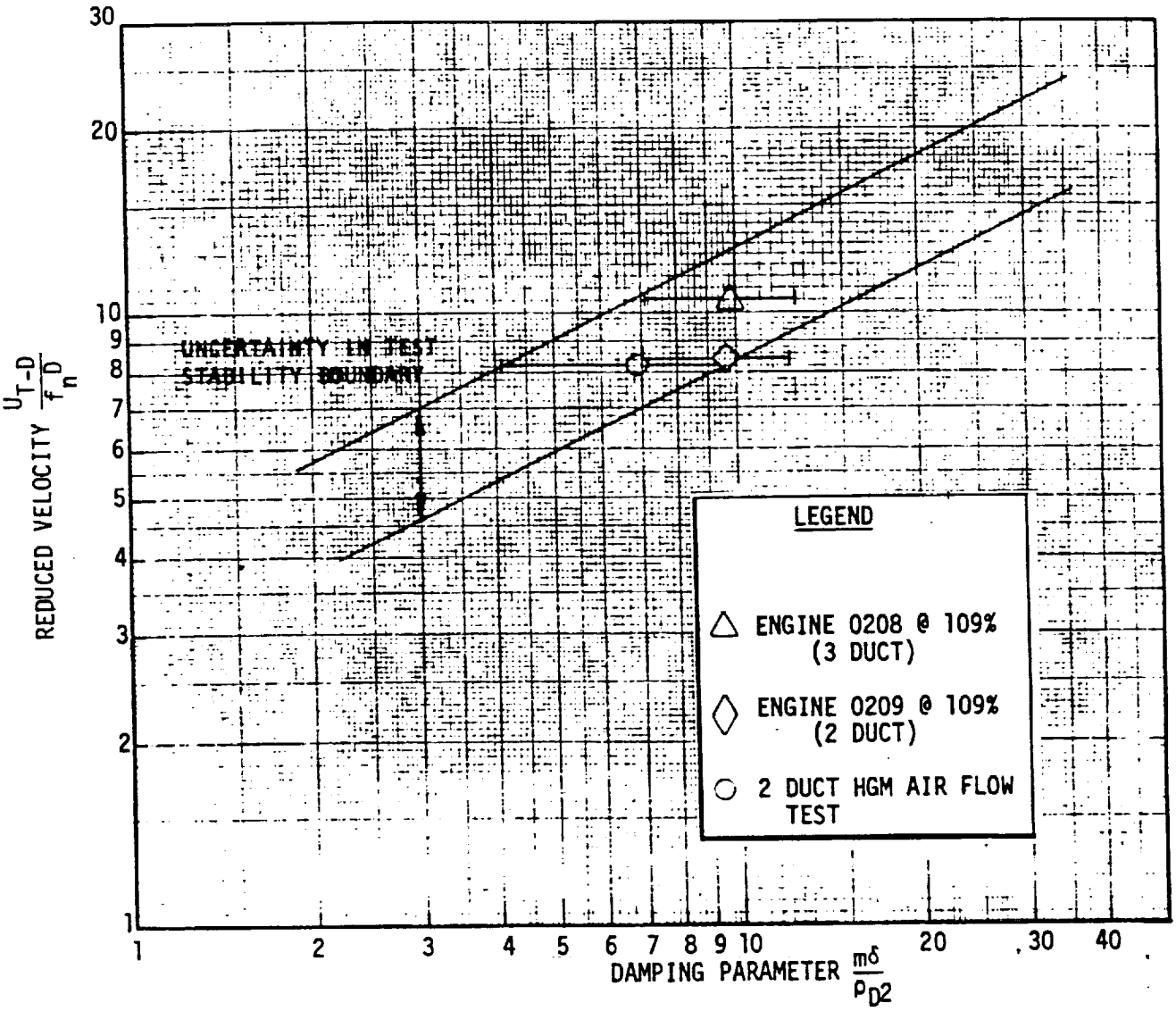

2.0 PROGRAM OVERVIEW

This test program was prepared to respond to the objectives and requirements as defined in the RFP 8-1-4 ED-11418 Work Statement. The entire program was organized, planned, and budgeted according to the tasks defined in the Work Statement. The principal objective of the program on flow-induced vibrations in the SSME injector heads, is to establish the fluid-elastic stability boundary for different sections of the SSME super-post injector under cross-flow and skimming flow conditions. This requires that an experimental investigation be carried out using properly simulated models of the SSME powerhead. The analytical and design phases of the program were jointly carried out by Rocketdyne and Westinghouse; the experimental phase was implemented at Marshall Space Flight Center, where compressed air at ambient temperature was used in a series of blowdown tests.

The analytical phase of the program started with the accomplishment of a pre-test analysis task, whereby predictions were formulated on the stability boundaries of pre-designated super-post elements located on an unshielded main injector to be tested on a three-duct hot gas manifold model. Because instability is expected to occur at flow conditions not achievable in cold-flow tests, work was performed to define the proper model super-post material, end restraint conditions and other pertinent structural simulation parameters to attempt excitation to unstable conditions within the constraints of the test facility. The resulting vibration response recorded during air flow tests, was then related to actual engine operating conditions by performing a similarity analysis. Upon detection of a stability boundary in the course of the experimental phase, it would then be possible to determine the corresponding engine power level at which the occurrence of an unstable condition is suspected. However, because instability was not detected during the experimental phase of the program, an alternative and more conservative approach was utilized whereby the data obtained at the highest possible achieved flow conditions was interpreted as a boundary below which the super-posts are considered stable.

PRE-TEST ANALYSIS

The purpose of the pre-test analysis was to define a properly simulated test approach for evaluating fluid-elastic excitation in the SSME. Included in this task are: (a) the determination of the best possible analytical prediction of the main injector stability boundary, (b) the formulation of criteria to be used in support of the hardware design task, and (c) the development of proper experimental techniques to effectively fulfill the program objectives.

Analytical Predictions

The stability boundary of the SSME super-post was predicted based on available data. In order to calculate effective and critical velocities, knowledge of the injector velocity profiles and post structural response (mode shape and damping) was required. Much of the information available for analysis did not bear a high degree of accuracy. The best data available were thus utilized to make a "first cut" prediction of the instability parameters. Predicting instability conditions analytically for the injector is also difficult because the instability correlations available from the literature are almost exclusively based on arrays of perfectly uniform cylinders, with uniform boundary conditions, tested in wind tunnels with uniform approach flows; conditions which are not characteristic of the SSME injector.

Main Injector Velocity. - Main injector skimming and gap velocity estimates were obtained through the use of computational fluid dynamics (CFD) and full-scale air flow test results available for the main injector. The CFD results available for the three-duct HGM configuration at the time of the pre-test analysis included only a laminar solution (Re=1000). The computational grid was designed to model a 120° slice of the three-duct HGM fuel side. The complex geometry of the main injector itself was modeled as a porous medium with 28.3% porosity (open area divided by total area), which corresponds to an unshielded super-post injector. The CFD model utilized an inlet flow uniformly distributed over the three transfer ducts. Although the computational model was subject to extensive simplifications, it provided a practical means for obtaining initial "rough cut" estimates for main injector instability thresholds.

Radial and tangential velocity profiles were obtained for three main injector locations. These locations were at $\theta = 0°$, 33°, and 85°, as shown in Figure 2.1. The $\theta = 33°$ and $\theta = 85°$ locations generally correspond to regions where post failures have occurred. The $\theta = 33°$ and $\theta = 85°$ locations are also in regions that are believed to experience some of the highest radial (V_r) and tangential or "skimming" (V_t) velocities, respectively. Finally, the three locations encompass array geometries that are in line ($\theta = 0°$) and staggered ($\theta = 33°, 85°$). The tangential velocities were taken just upstream of the porosity location in the CFD results. The radial (gap) velocities were obtained by adjusting the velocity at this location by the porosity value. A typical CFD velocity profile is shown for the $\theta = 0°$ location in Figure 2.2. The velocity is normalized by the transfer duct inlet velocity U. Several of the CFD velocity profiles appeared to have a distinct parabolic shape. A small amount of unshielded flight post three-duct HGM airflow data from previous Rocketdyne tests are available for comparison with the CFD data. These measurements tend to indicate that injector gap velocity profiles are probably more uniform than those predicted by the laminar CFD results.

Figure 2.1 - Plan View of SSME Injector and Test Model Arrays Locations.

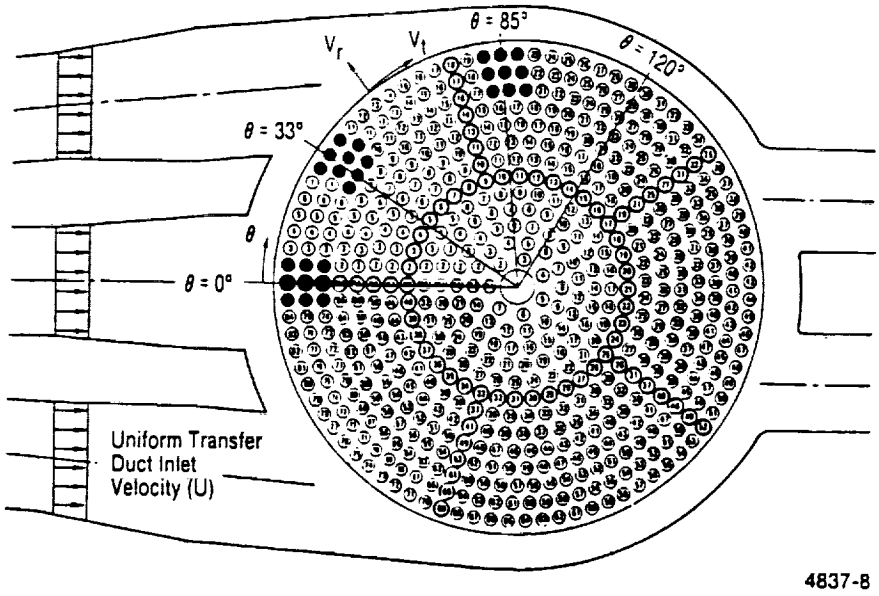

Superpost Mode Shape. - The superpost mode shape was obtained from a Stardyne computer model. Spring connections were used at three locations, two simulating the retainer/post thread joint and a third at the standoff location (see Figure 1.4). The natural frequency of the super-posts installed in a full-scale injector was measured in support of the earlier test program and was determined to be approximately 1820 Hz. The spring constants used for the boundary conditions for the dynamic model were varied so as to match with the measured post natural frequency. The mode shape (first mode) obtained is shown in Figure 2.3. The mass distribution for the post is also necessary for calculation of the effective velocity and is obtained once the elemental dynamics model is established.

Figure 2.2 - CFD Result for Radial Velocity at $\theta = 0°$
Location (Upstream of Porosity)

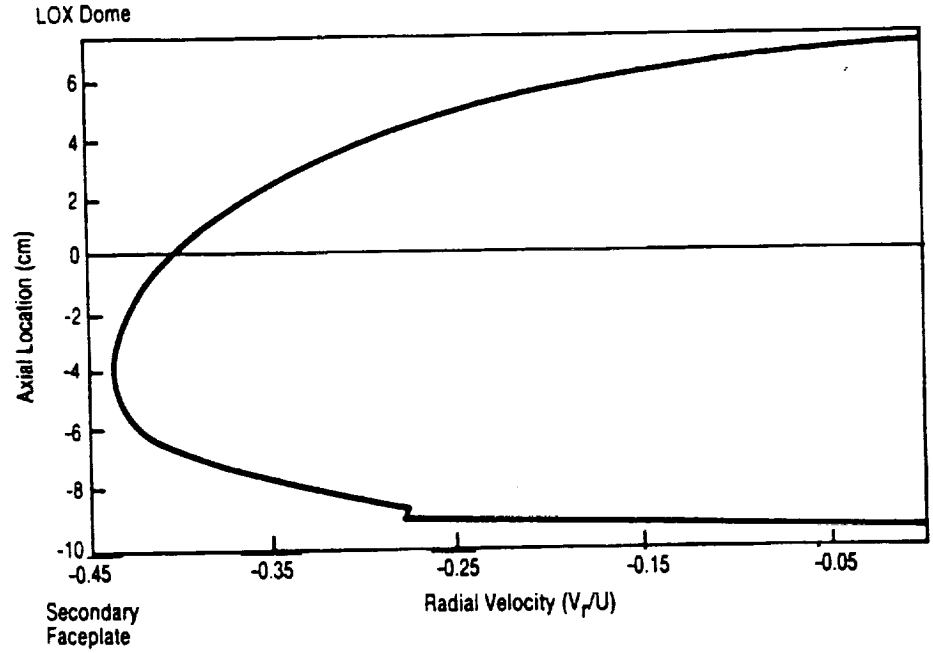

Figure 2.3 - Engine and Model Superpost Mode Shapes

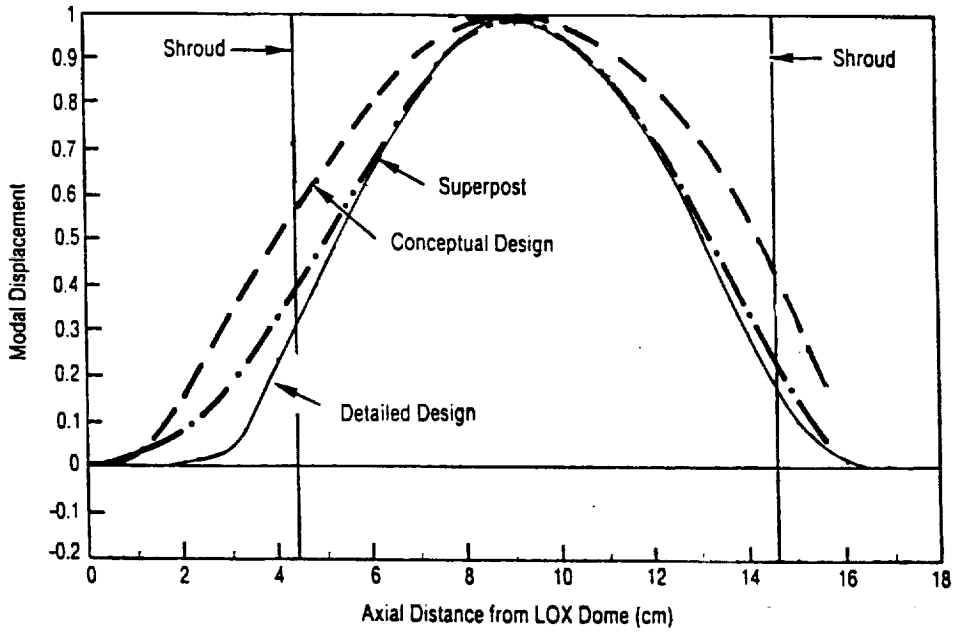

Damping. - As previously mentioned, significant uncertainty exists in the damping values for the super-posts. The variation is mainly attributed to differences in fitup in the threaded region of the posts that give rise to amplitude-dependent, nonlinear damping effects. Based on experiments, damping of the engine super-posts ranges from ζ = 0.84% to 2.3%. Bench testing appears to be warranted to better determine superpost damping and to investigate the range in damping that can be expected as a function of installation fitup. For the model posts, known repeatable damping values were desired and bench testing, as well as main injector testing, of the individual posts had to be performed to determine damping and natural frequency. This type of testing is discussed in more detail in the Instrumentation calibration section of this report.

Instability Prediction. Instability initiates when

$$\frac{U_{en}}{U_{cn}} \geq 1.0 \tag{8}$$

where the critical velocity, U_{cn}, is given by

$$U_{cn} = \beta f_n D \left(\frac{m_0 \delta_n}{\rho_0 D^2}\right)^{1/2} \tag{9}$$

and the effective velocity, U_{en}, is given by Equation 7. Since both radial and tangential velocities act on the LOX posts, instability is predicted to initiate when

$$\left[\left(\frac{U_{er}}{U_{cr}}\right)^2 + \left(\frac{U_{et}}{U_{ct}}\right)^2\right]^{1/2} \geq 1.0 \tag{10}$$

where:

U_{er} = effective radial velocity

U_{et} = effective tangential velocity

U_{cr} = critical radial velocity

U_{ct} = critical tangential velocity.

Calculation of the above values were made for 109% power level engine operating conditions using the data shown in Table 2.1. There is scatter among the values of β reported by the different investigators. The following data were used:

1. Inline arrays, Ref.(15): $\beta_r = (0.37 + 1.76\ T/D)$
2. Triangular arrays, Ref.(16): $\beta_r = 10\ (T/D - 1)$
3. Skimming flow, Ref.(16): $\beta_t = 4.5$.

The values of β in Table 2.1 are for the superpost pitch to diameter ratio (T/D) of 1.7.

Table 2.1 - Engine and Airflow Model Superpost Stability Calculation Parameters

Config-uration	D (mm)	β_t	β_r (In-line)	β_r (Trian-gular)	ρ (kg/m^3)	m_o (kg/m)	$\delta_n = 2\pi\zeta_n$	f_n (Hz)	U (m/sec)
Engine	9.855	4.5	3.385	7.00	12.27	0.456	0.1257	1821	209
Air	9.855	4.5	3.385	7.00	12.27	0.0688	0.0628	470	30.5

Results from the stability calculations are shown in Table 2.2. Under the conditions evaluated, instability is not predicted for the SSME when a damping value of $\zeta_n = 2.0\%$ is used. The $\zeta_n = 0.5\%$ condition indicates instability for all three injector locations examined, with the $\theta = 0°$ location being predicted as the least stable.

Table 2.2 - Summary of Fluidelastic Instability Calculations for Row 13 Engine Superpost

Velocity Parameters	Damping* (%)	Circumferential Location		
		$q = 0°$	$q = 33°$	$q = 85°$
U_{er} (m/s)		307.2	437.6	174.5
U_{cr} (m/s)	2	423.0	874.8	423
U_{et} (m/s)		0	19.96	221.6*
U_{ct} (m/s)	2	562.0	562.0	562.0
U_{er}/U_{cr}	2	0.728	0.574	0.412
U_{et}/U_{ct}	2	0	0.036	0.394
$[(U_{er}/U_{cr})^2 + (U_{et}/U_{ct})^2]^{0.5}$	2	0.728	0.575	0.570
$[(U_{er}/U_{cr})^2 + (U_{et}/U_{ct})^2]^{0.5}$	0.5	1.456	1.150	1.140

*Estimate

Based on Eq. (9), and assuming constant $\delta_{n,}$, it can be inferred that:

$$U_{cn}\sqrt{\rho_o} = \text{constant} \qquad (11)$$

Equation (11) can be used as a simple means of assessing the imminence of an unstable condition during actual testing; the resulting estimate, however, is only as good as the assumptions used to compute the value of the constant. Using Eq. (9) and Table 2.1, the following conditions were calculated for the onset of fluid-elastic instability of the model LOX posts:

Table 2.3 - Instability Thresholds Prediction for Steel-Tipped Model Super-Posts

ROW 13 LOCATION	$U_{cn}\sqrt{\rho_o}$ [Ft/s(Lbm/Ft^3)$^{1/5}$]
0°	67
33°	108
85°	100

LOX POST MODEL DESIGN

The criteria for the model superpost design included the following:

- Fundamental natural frequency and damping values that ensured fluidelastic instability for the range of flow velocities and fluid densities obtainable in the SSME air test model.
- Adequate strength to prevent failure during the tests.
- Reproducible damping and frequency characteristics with no significant change over time or vibration history.
- Easy removal and installation from an assembled injector to avoid injector disassembly and reassemble for model post replacement or modification.

Detailed LOX Post Design

Several design concepts for the model post were considered. The conceptual design chosen in the early stages of the program was similar to a design concept successfully used in testing at Westinghouse, and is shown in Figure 2.4(a). The model post was made out of Vespel and featured reduced diameter sections at the top and bottom ends to reduce the natural frequency. Shrouds are placed over these locations in order to duplicate the overall aerodynamic shape of the SSME LOX posts. Each element was fixed at the top by threading it into the LOX dome inter-propellant plate. The faceplate end was fixed by the combination of the threaded anvil and a nut. This conceptual model design was analyzed using the Westinghouse WECAN code to obtain natural frequency and mode shape. The natural frequency for the conceptual model post design was 256 Hz, and the mode shape is shown in comparison with the Haynes super-post in Figure 2.3. A stability calculation for the conceptual model post in an air-flow test environment was made using the parameters shown in Table 2.1. The results are shown in Tables 2.2 and 2.3. The prediction shows the conceptual post design to be unstable at airflow test operating conditions. Since this initial calculation, a more refined and detailed post design was developed that conforms to the design constraints of the injector test article. The final version of the design is shown in Figure 2.4(b) and the mode shape is shown in Figure 2.3.

Figure 2.4 - Row 13 Model LOX Post (dimensions in mm)
(a) - Model Superpost Conceptual Design
(b) - Final Design Version: Steel Tipped LOX Post

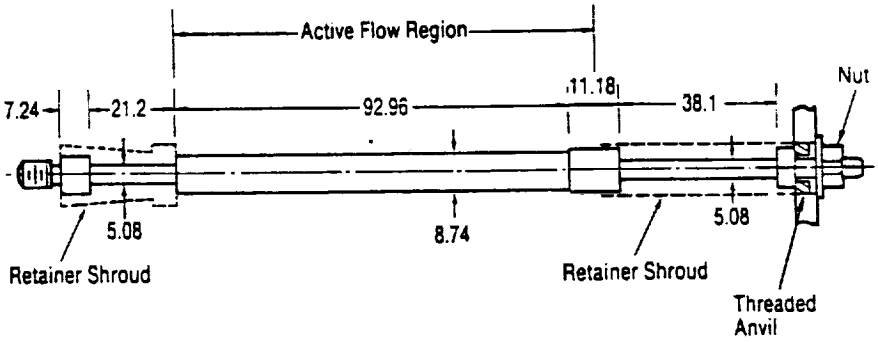

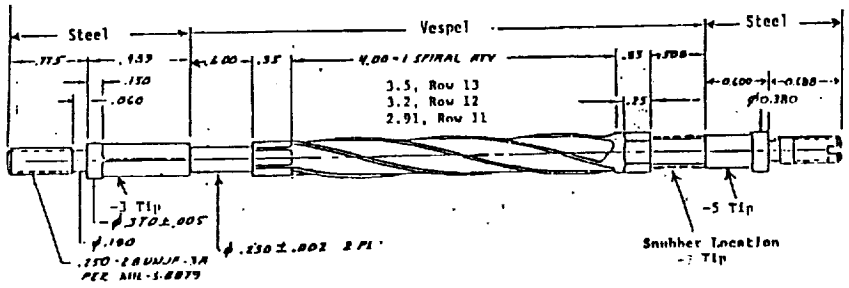

RI/RD 91-157

The final design is the last of a series of design iterations which were carried out in an effort to obtain the best possible mode shape match to the Haynes super-posts, as well as a sufficiently sturdy construction which would go unstable only in the upper range of the air flow test facility capabilities. The main feature of this improved design is the addition of steel tips to the ends of the Vespel LOX post model main body (see Figure 2.4(b)). The Vespel portion is threaded into the upper and lower steel tips, with the use of Loctite material to prevent the post from spinning about its axis. The steel tips, in turn, are held in place in the same manner as the conceptual post described earlier. Figure 2.5 shows a typical assembly view of a steel tipped model LOX post into the main injector hardware.

The steel tipped model LOX post was re-analyzed using the Stardyne computer code. As Figure 2.3 shows, the mode shape of the new design follows the Haynes post mode shape much better than the conceptual model. The natural frequency, however, increased to about 470 Hz (as opposed to 256 Hz for the conceptual model). Due to the higher natural frequency and m_o, the critical velocity ratios, shown in Table 2.4 for the conceptual model, are likely to be higher for the metal tipped design, thus resulting in a model super-post which is more stable during blowdown testing, but is also a better simulation of the structural characteristics of the Haynes super-post.

Figure 2.5 - Typical Steel-Tipped Model Superpost Installation
in the Main Injector Test Article (Row 12 post shown)

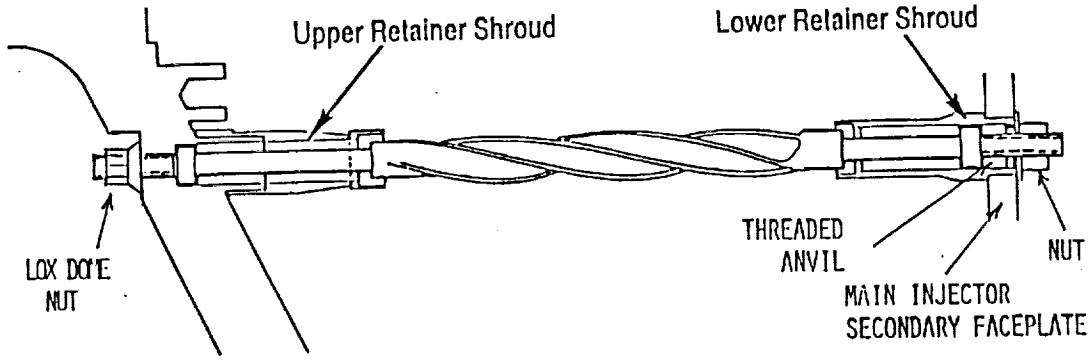

Table 2.4 - Summary of Fluidelastic Instability Calculation for Row 13 Conceptual Model Superpost

Velocity Parameters	Damping (%)	Circumferential Location		
		θ = 0°	θ = 33°	θ = 85°
U_{er} (m/s)		38.97	49.76	18.74
U_{cr} (m/s)	1	16.24	33.58	16.24
U_{et} (m/s)		0	1.69	23.80
U_{ct} (m/s)	1	21.59	21.59	21.59
U_{er}/U_{cr}	1	2.400	1.482	0.154
U_{et}/U_{ct}	1	0	0.078	0.102
$[(U_{er}/U_{cr})^2 + (U_{et}/U_{ct})^2]^{0.5}$	1	2.400	1.484	0.596
$[(U_{er}/U_{cr})^2 + (U_{et}/U_{ct})^2]^{0.5}$	2	1.697	1.150	1.128

Figure 2.6 - Stability Map Showing Engine and Model Operating Conditions and Stability Boundary (based on smooth tube data) for θ = 0° Locations

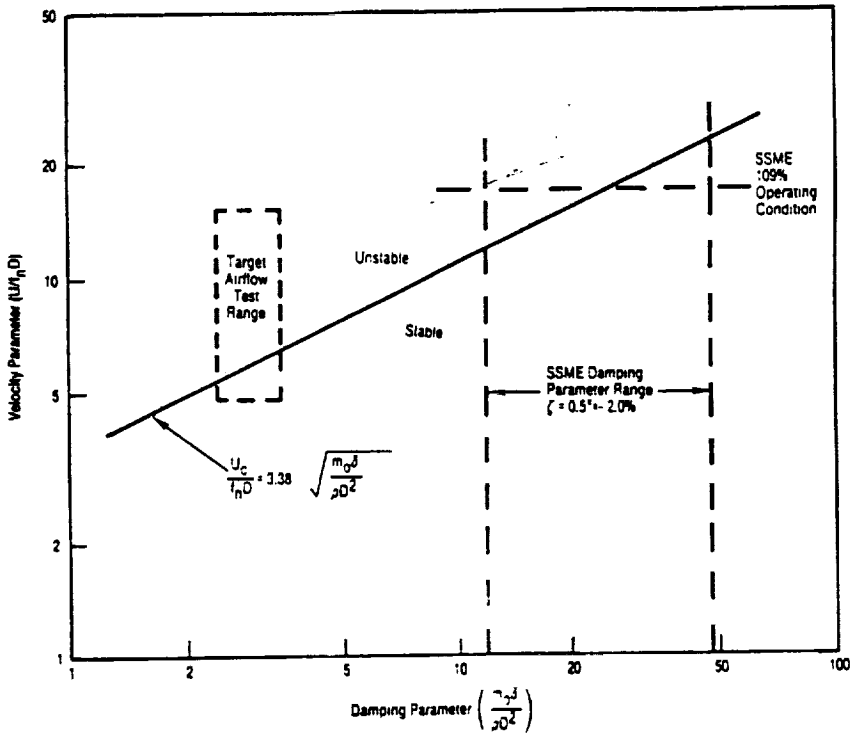

Design Verification

Bench testing was originally developed for verifying the conceptual model post design and calibration of the instrumented model posts before installation in the main injector test article. Tests of a "verification post" (without swirlers) were performed. A natural frequency of 270 Hz, comparable to the value of 256 Hz used in the conceptual model post instability calculations, was measured. A damping (ζ) of 0.64% was measured and found to be essentially independent of vibration amplitude. Dynamic testing was conducted by shaking the post at specified amplitudes for 2-hour intervals in both the horizontal and vertical planes. The verification post tests demonstrated that damping, natural frequency, and calibration remained constant and were repeatable after post disassembly and reassembly.

The damping value of 0.64% measured in the bench tests was lower than that used in the model stability calculations (Table 2.4). In order to ensure that the model post was not too conservative (unstable) at the available airflow facility operating conditions, a higher frequency design was developed, as discussed in the preceding section. Bench tests were repeated, yielding new values of damping and natural frequency of about 0.8% and 470 Hz, respectively.

Parts List

Table 2.5 provides a list of the individual parts used to assemble the model LOX posts into the injector hardware.

Table 2.5 - Model LOX Posts Parts List

DESCRIPTION	PART NUMBER	QUANTITY
MAIN INJECTOR ASSY	7R0017545	1
ROW 13 LOX POST ELEMENT	7R035179-3	12
ROW 12 LOX POST ELEMENT	7R035179-5	11
ROW 11 LOX POST ELEMENT	7R035179-7	10
UPPER RETAINER SHROUD	7R035167-3	27
ROW 13 LOWER RETAINER SHROUD	7R035167-9	9
ROW 12 LOWER RETAINER SHROUD	7R035167-9	9
ROW 11 LOWER RETAINER SHROUD	7R035167-5	9
UPPER TIP ADAPTOR		27
LOWER TIP ADAPTOR		27
UPPER RETAINER NUT		27
LOWER RETAINER NUT		27
JAM NUT	7R035168-3	27
WASHERS		54
SPECIAL TOOLS		
LOCKNUT TOOL	7R035172-1	1
POST TOOL	7R035172-7	1
JAM NUT TOOL	7R035172-11	1

HARDWARE FABRICATION

The hardware fabrication task was subdivided in two separate categories: 1) fabrication of new hardware, and 2) modifications to existing hardware. The new Vespel LOX posts, fabricated by Westinghouse Corp., were based on the design discussed in the preceding section; a total of 27 Vespel LOX posts (plus a few spares) were made available for assembly of three 3x3 arrays extending over main injector rows 11, 12 and 13. For each Vespel LOX post, two stainless steel tips and matching nuts were also required for assembly into the main injector. Figure 2.5 shows a typical assembly view of the LOX post within the main injector.

Several modifications to the main injector hardware were necessary for proper fit of the LOX posts as well as for instrumentation wiring; Microcraft Inc. was primarily responsible for this task. The main injector primary and secondary face plates were retrofitted to accept the metal-tipped LOX post hardware. The most extensive modifications were made to the main injector assembly. After cutting away the thrust cone and LOX inlet manifolds, the upper portion of the doughnut shaped LOX dome was removed, thus exposing the liquid oxygen side of the interpropellant plate. This operation was necessary in order to apply the necessary modifications to the interpropellant plate for LOX post assembly and instrumentation wiring. Additional modifications were also made to permit installation of a 2 inch thick steel pressure proof plate, to be bolted onto the interpropellant plate itself, and of sufficient structural strength to bear most of the powerhead weight as well as thrust generated during the blowdown tests. This plate was also equipped with multi-lead electrical connectors for easy interface of the strain gage instrumentation circuits with the data acquisition systems. Figure 2.7 shows a cross-sectional view of the modified injector hardware in comparison with standard SSME injector.

TEST FACILITY

The air flow facility at MSFC incorporates a high-pressure storage supply tank and a compressor for tank replenishment. The maximum operating pressure of the storage tank is rated at 4200 psig. Flow into the fuel and oxidizer legs is controlled individually by valves which regulate the downstream model inlet pressure to a specified value. This approach in regulating the line pressure provides acceptable run times at given steady state flow conditions. A full description of the facility operation is available in the Facility Operation Guide.

Figure 2.7 - SSME Main Injector Cross-Section
(a) - Actual SSME Hardware
(b) - Test Hardware

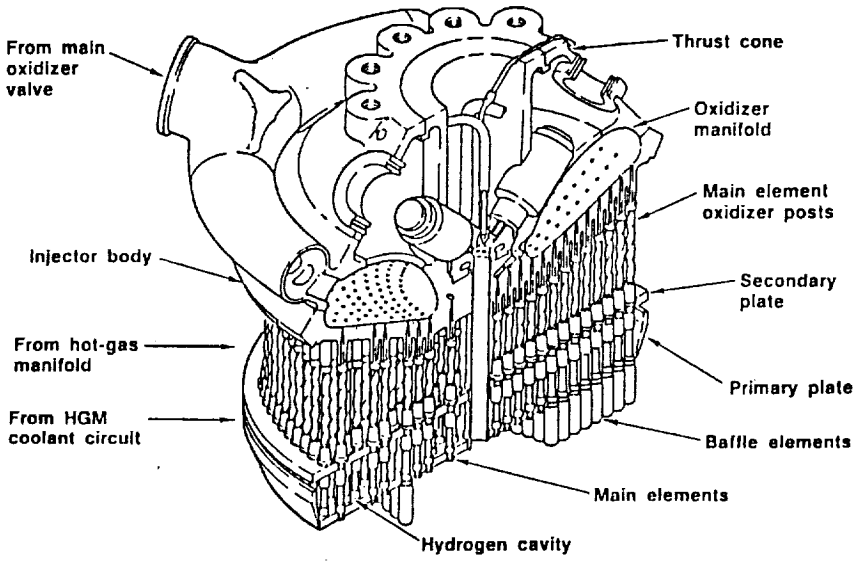

LSS-EC-T-113

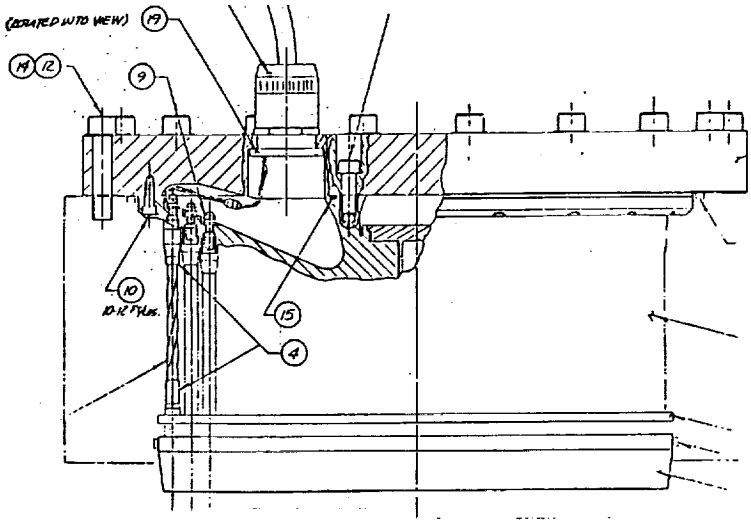

Capabilities

A schematic layout of the facility hardware is shown in Fig. 2.8. The mass flow rates in each leg are measured with two venturi flowmeters located just upstream of the model inlets, and it can be set to pre-established values from the control room. A pressure probe is utilized to measure total pressure upstream of the venturis and the static pressure is measured in the throat plane with four wall taps manifolded together. The 15.6-in. internal pipe diameter is constricted at the Venturi flowmeters to 8.5 in. on the fuel side and 6.2 in. on the oxidizer side to provide a delta P sufficient for flow rate determination, yet resulting in a small overall pressure loss. An exit valve is located between the model main combustion chamber and the exhaust pipe.

The valve is adjustable to provide a choked flow condition so that the desired pressures are maintained in the model. Table 2.6 summarizes the facility capabilities relative to the conditions existing in a phase II+ SSME.

Table 2.6 - Facility Capabilities

PARAMETER	SSME	AIR FLOW FACILITY	
		MIN	MAX
Fuel Inlet Pressure	3570	50	420
Fuel Flow Rate (lbm/sec)	180	13	171
1-D Velocity in FTD (ft/sec)	507	156	312
Mach Number in FTD	0.10	0.14	0.28
Reynolds Number in FTD	$1.3x10^7$	$1.3x10^7$	$1.6x10^7$

Figure 2.8 - NASA/MSFC Air Flow Test Facility

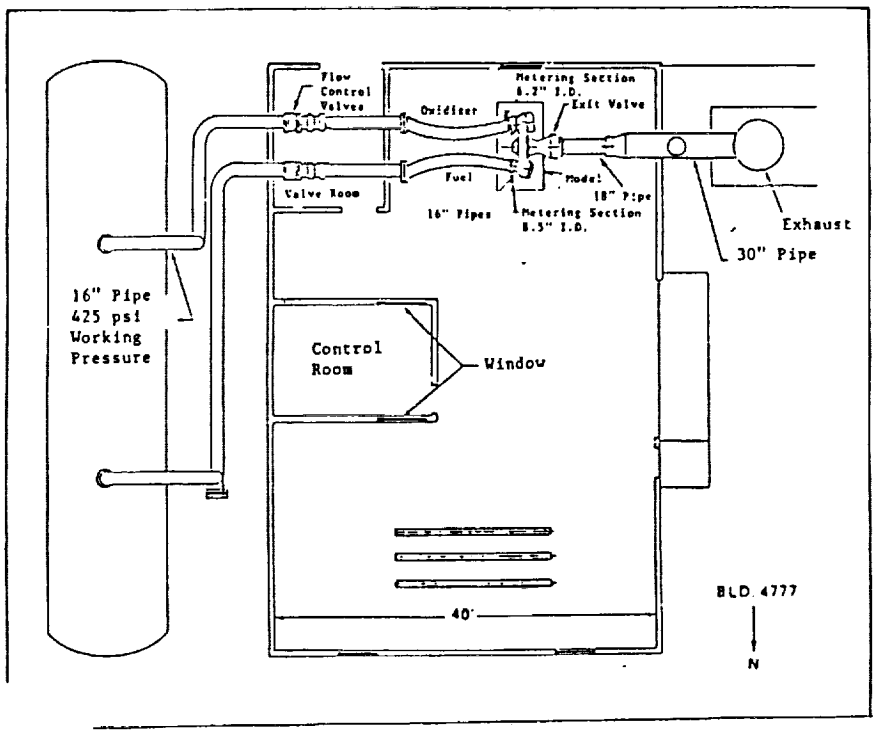

Hot Gas Manifold Model Description

The test model is a full-scale aluminum replica of a three duct Hot Gas Manifold, shown in Figure 2.9. The modular design of this test article allows for retrofitting to a two-duct powerhead version. Most of the instrumentation ports are built into the model itself in the form of permanent wall taps as well as removable ports. The model can accommodate static and total wall pressure taps, total pressure Kiel probes, total pressure pitot tubes, three-dimensional directional probes, total pressure rakes, and high frequency dynamic pressure transducers. Pressure measurements in the fuel side of the model comprise a large portion of the instrumentation, however there are also several ports and taps available for measuring internal flow parameters associated with the oxidizer side, the main injector, and the main combustion chamber. The model was designed and constructed by Microcraft Inc.

During testing, a 70/30 mass ratio of fuel side air flow to oxidizer side air flow is maintained to simulate actual hot-fire conditions. On both fuel and oxidizer sides, the flow enters the respective preburner simulator and is manifolded into an annular passage. On the fuel side, there are twelve large support struts equally spaced circumferentially in the annular passage at the inlet region. The struts simulate major structural components associated with the engine's High Pressure Fuel Turbine (HPFT). Tubing from nearby pressure sensors are routed through the struts.

Just downstream of the struts, two perforated plates are used as turbine simulators. The turbine simulator plates produce a pressure drop simulating that which is generated by the fuel and oxidizer turbine rotors. Swirl vanes are installed just downstream of the turbine simulator plates to simulate the angle of attack of the flow exiting the second stage nozzle, as on the SSME turbines. After exiting the turbine simulator, the flow changes direction 180 degrees in the turnaround duct (TAD) region. Downstream of the 180-degree turn, the outer wall of the annular flow channel is designed with an outward taper for approximately 5-degrees. In addition, there are twenty-four struts and posts in the fuel bowl region to simulate engine components at this region.

Figure 2.9 - Modular Hot Gas Manifold Model (by Microcraft Inc.)

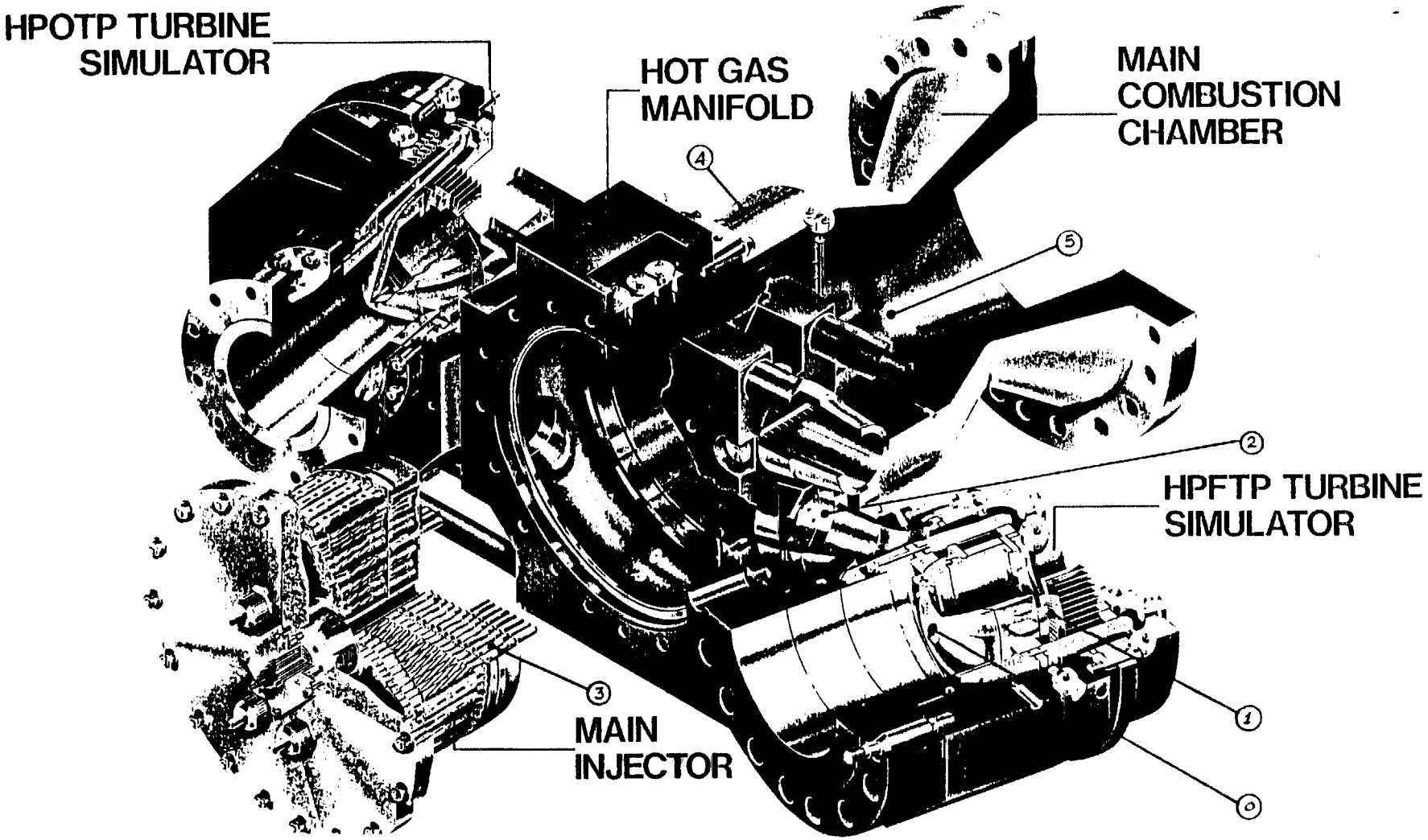

The oxidizer side has four sets of perforated plates similar to the fuel plates which simulate the oxidizer turbine rotors. The porosity of these plates is approximately 50%. The outer wall annular flow channel downstream of the turnaround duct on this side has a 35-degree taper. There are also two turning vanes on the oxidizer side to guide the flow into the heat exchanger. The second set of turning vanes is actual flight hardware as it is part of the heat exchanger assembly .

The fuel preburner/turbine simulator is designed to be easily assembled and disassembled. In the fuel section, the interfaces are designed for easy adaptation of new components, such as the alternate turbopump designed by Pratt & Whitney. The main injector is actual flight engine hardware that was modified for testing purposes. The main injector is a shieldless super-post design, with three arrays of LOX posts designed, built, and specially instrumented for this test program; sections 1.0 and 2.0 of this report cover the description of this component in more detail . Flow across the LOX posts on the oxidizer side is also simulated in the test. Various coolant flows are not simulated, such as in the cavity between the injector face plates.

Instrumentation

Both digital and analog instrumentation were utilized in the course of the experimental phase of the program.

Digital Instrumentation

Table 2.7 summarizes the digital data requirements. Two sets of facility pressure transducer ranges were utilized in order to provide accurate Venturi flowmeter measurements in the lower and higher facility flowrate ranges. The total amount of digital sensors used was considerably less than utilized in previous HGM air flow testing.

Sufficient instrumentation was specified to determine only the basic information essential to the scope of the test program, such as fuel and oxidizer leg flow rates, turbine inlet total pressures, turbine and transfer duct static pressures, and MCC pressure. The shortened list was helpful in reducing the activity involved in digital instrumentation calibration, leak checks, and debugging.

Table 2.7 - Digital Instrumentation Parameter List

ITEM	LOCATION	INSTR.	MEASUREMENT	EXPECTED RANGE A	EXPECTED RANGE B	COMMENT/DESCRIPTION
1	FACILITY	TIME	TIME			TIME RECORD
2		MARKER	MARKER	*	*	MARKER SIGNAL
3		PRESS.	PT-FMETER			FUEL LINE PRESS.
4		PRESS.	PT-XMETER			OX LINE PRESS.
5		DELTA PRESS.	DPS-FMETER			METERING P-FUEL
6		DELTA PRESS.	DPS-XMETER			METERING P-OX
7		TEMP.	TT-FMETER	450-550R		MODEL INLET TEMP-FUEL
8		TEMP.	TT-XMETER	450-550R		MODEL INLET TEMP-OX
9	FUEL TURB.	TOTAL	PT-FCC01			DOME NOSE
10	FUEL TAD	STATIC	PS-FC01			HUB WALL-TE
11	REGION		PS-FC02			
12			PS-FC03			
13			PS-FC04			
14			PS-FC05			
15			PS-FC06			
16			PS-FC07			
17			PS-FC08			

ITEM	LOCATION	INSTR.	MEASUREMENT	EXPECTED RANGE A	EXPECTED RANGE B	COMMENT/DESCRIPTION
18	FUEL TAD	STATIC	PS-FC09			TURB. HOUSING WALL-TE
19	REGION (CONT.)		PS-FC10			
20			PS-FC11			
21			PS-FC12			
22			PS-FC13			
23			PS-FC14			
24			FS-FC15			
25			PS-FC16			
26	FUEL	STATIC	PS-FLA_			OUTER WALL-LTD
27	TRANSFER		PS-FLA_			INNER WALL-LTD
28	DUCT		PS-FLB_			UPPER WALL-LTD
29			PS-FLB_			LOWER WALL-LTD
30			PS-FCA_			RIGHT WALL-CTD
31			PS-FCA_			LEFT WALL-CTD
32			PS-FCB_			UPPER WALL-CTD
33			PS-FCB_			LOWER WALL-CTD

ITEM	LOCATION	INSTR.	MEASUREMENT	EXPECTED RANGE A	EXPECTED RANGE B	COMMENT/DESCRIPTION
34	FUEL TRANSFR	STATIC	PS-FRA_			LEFT WALL-RTD
35	DUCT (CONT.)		PS-FRA_			RIGHT WALL-RTD
36			PS-FRB_			UPPER WALL-RTD
37			PS-FRB_			LOWER WALL-RTD
38	OX TURB	TOTAL	PT-XA01			DOME NOSE
39	OXIDIZER	STATIC	PS-XI1			XLTD
40	TRANSFER		PS-XI3			XLTD
41	DUCT		PS-XI5			XLTD
42			PS-XI7			XLTD
43			PS-XI9			XRTD
44			PS-XI11			XRTD
45			PS-XI13			XRTD
46			PS-XI15			XRTD

Analog Instrumentation

The analog data for the entire series of tests consisted solely of strain gage instrumentation mounted on the model LOX posts. Two half-bridges consisting of two coplanar pairs of SK13031CF350 strain gages per LOX post were used; each pair was mounted orthogonal to each other in the radial and tangential directions. The axial position of the strain gage pairs was chosen at the top portion of the post (LOX dome end), 0.2 inch above the swirler region shoulder. In this position, the strain gages are protected by the inter-propellant plate shrouds.

A special bonding technique, which included the use of a special bonding agent as well as baking at elevated temperatures, was developed in order to prevent detachment of the strain gages during exposure to a harsh flow environment. The technique was later verified by shaker tests at the fundamental frequency for two hours. A total of six leads, three from each bridge, were used on each instrumented post. The leads consisted of 30 AWG teflon coated wires, which were routed through holes into the LOX dome, where they merged with wires from other instrumented posts to form a bundle, as depicted in Figure 2.7(b). At the end of the wire bundle, a single multi-lead quick-disconnect electrical connector was mounted on the LOX dome plate to facilitate injector assembly. Solder tabs located below the retainer shroud for accessibility and to facilitate LOX post removal (Figure 2.10), were used as junction points between the teflon coated wires and the strain gage leads.

Table 2.8 lists the model posts and strain gage instrumentation locations. A later section in this report on the Analog Data Acquisition System describes in detail the electrical circuitry and data recording techniques.

Figure 2.10 - Model Super-Post Strain Gage Instrumentation

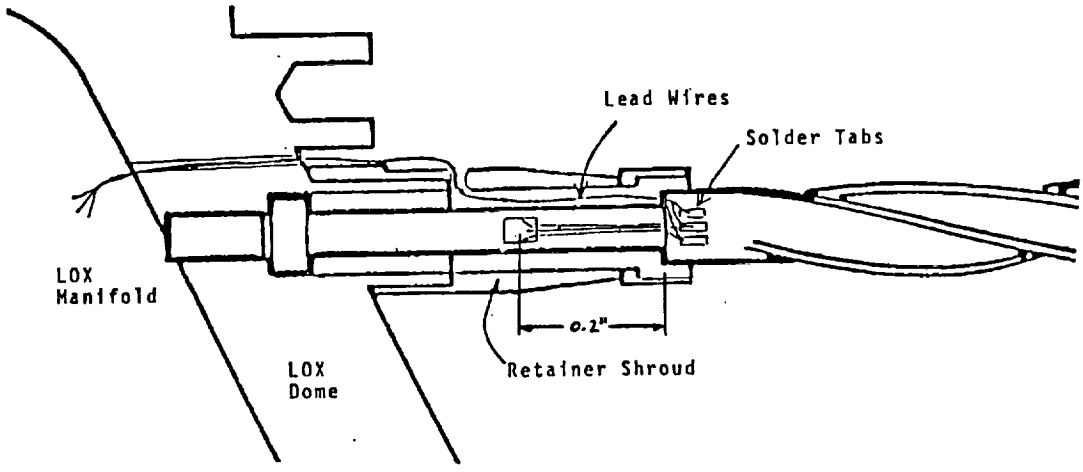

Table 2.8 - Vespel Model Super-Post Injector Strain Gage Instrumentation List

ARRAY LOCATION	ROW	POST	STRAIN GAGE MOUNTING	PARAMETER NAME
0 DEGREES	13	85	RADIAL	R13P85R
		85	TANGENTIAL	R13P85T
		01	RADIAL	R13P01R
		01	TANGENTIAL	R13P01T
		02	RADIAL	R13P02R
		02	TANGENTIAL	R13P02T
	12	01	RADIAL	R12P01R
		01	TANGENTIAL	R12P01T
	11	01	RADIAL	R11P01R
		01	TANGENTIAL	R11P01T
33 DEGREES	13	08	RADIAL	R13P08R
		08	TANGENTIAL	R13P08T
		09	RADIAL	R13P09R
		09	TANGENTIAL	R13P09T
		10	RADIAL	R13P10R
		10	TANGENTIAL	R13P10T
	12	09	RADIAL	R12P09R
85 DEGREES	13	20	RADIAL	R13P20R
		20	TANGENTIAL	R13P20T
		21	RADIAL	R13P21R
		21	TANGENTIAL	R13P21T
		22	RADIAL	R13P22R
		22	TANGENTIAL	R13P22T
	12	20	RADIAL	R12P20R
		20	TANGENTIAL	R12P20T

Calibration of Model LOX Posts

Static calibrations, consisting of the simple measurement of strain gage output voltage versus deflection, were performed on all instrumented LOX posts. In order to ascertain the validity of the resulting calibration curves, tests were performed on each LOX post prior to installation into the main injector - by means of a fixture simulating the injector (bench tests), and after installation into the main injector (injector tests).

Bench Tests

All bench calibration tests were carried out at Westinghouse; the following instrumentation was utilized in order to carry out these tests:

1. Strain gage conditioner Vishay Model 2100. Half bridge input, with 350 ohm fixed-resistors that complete the bridge internal to the Vishay.

2. Bridge excitation voltage, 1.5 V; Amplifier gain, 400.

3. Shunt resistor (for calibration check when gages are installed in the injector), 82.232 K ohms. One of the active gages was shunted for each bridge (yellow/white leads). A shunting connection device was used to check strain gages.

4. The simulated LOX dome end of the calibration fixture was modified to permit the threaded end of the post to pass through a clearance hole and be secured by a nut. The nut on each end of the model post was torqued to 40 in-lb.

Two static calibrations were performed for each bridge. A typical calibration curve is shown in Figure 2.11. Repeatability and linearity have been noted to be consistently acceptable. The post is calibrated with the longitudinal axis in a horizontal plane. The angular orientation of the post is adjusted so that when a horizontal force is applied there is large output from the strain gage bridge that measures motion in the horizontal direction, and a very small output from the strain gage bridge that measures motion in the vertical direction. The scribe mark indicating the radially outward direction on the post is oriented to face upward. The calibration constant for a vertically applied load is designated as C(V), the stiffness lb/in for a vertically applied load is K(V), the shunted bridge output for the gages that measure motion in the vertical direction is S(V), and the millivolt (mv) output for a 2 lb force applied in the vertical direction is F(V) (this value can be used as a calibration check after the posts are installed in the model). The corresponding designations for the horizontally applied load are C(H), K(H), and S(H) (no value for F(H) is given since it is not be possible to check that direction when the post is in the model). The damping is obtained from pluck tests. The post was plucked in the vertical direction and most of the ensuing motion is in the vertical direction. The strain gage signals are passed through high pass filters set at 250 Hz.

The damping expressed as percent critical damping is calculated, using the vector amplitude for the two directions, according to the formula

$$\zeta = \frac{100\delta}{2\pi} = \frac{50}{\pi N} \ln \left[\frac{\sqrt{x_0^2 + y_0^2}}{\sqrt{x_N^2 + y_N^2}} \right]$$

The damping is evaluated at two convenient amplitude ranges (typically at approximately 13 mils peak-to-peak to 8 mils peak-to-peak, and at approximately 8 mils peak-to-peak to 5 mils peak-to-peak) and the average value is reported. The post natural frequency is obtained from the same amplitude/time curves used to determine damping.

The pluck test is conducted with the use of a spring scale to apply a force of 1200 grams at the middle of the swirler region (the same location used to apply the force and measure the deflection during the static calibrations). A rubber band is attached to the end of the spring scale. A loop of fish line goes around the post and is attached to the rubber band. With the strip chart running, the fish line is cut and the amplitude decay curve recorded. It is convenient to pull vertically in the laboratory tests. However, the technique was shown to work equally well for a pull in the horizontal direction (the pull will be horizontal when the damping check is made with the post in the injector head), and the damping values obtained are essentially the same for the two directions.

Calibration test results for the steel-tipped posts are given in Table 2.9 and typical curves are plotted in Figure 2.11. The bridge outputs with one of the active gages shunted were very similar for all the posts. The damping values were also very similar for all posts, with 0.819% critical damping being the average. The average natural frequency is 473.8 Hz for Row 13 posts, 536.3 Hz for Row 12 posts, and 598.7 Hz for Row 11 posts. The calibration constants (mv/mil) for the posts are also given. The variation in calibration from post-to-post (for the same row) for a given direction probably reflects small differences in gage placement.

Injector Tests

Calibration tests similar to the bench tests described in the preceding section were carried out at Rocketdyne just prior to shipment of the injector assembly to MSFC for air flow testing. In order to access LOX post rows 11 and 12, obstructing LOX posts were removed and reassembled upon completion of the test procedure. Each instrumented post was plucked by tying a length of dental floss to the marked center of the post and to a rubber band. A dynamometer was hooked to the rubber band, and a force of 910 grams (2 Lbs) was applied by pulling radially outward in the

Table 2.9 - Bench Test Calibration Results for Steel-Tipped LOX Posts

POST	f_n Hz	ζ %	C(H) mv/mil	C(V) mv/mil	S(H) mv	S(V) mv	K(H) lb/in	KV) lb/in	F(V) mv/2lb
R13P08	472	0.765	67.7	62.1	650.8	643.5	258	250	491
R13P09	480	0.790	62.0	59.2	651.5	645.0	255	253	462
R13P10	472	0.844	64.4	60.2	651.0	645.0	250	253	469
R13P20	460	0.833	68.8	60.5	650.0	642.7	235	233	514
R13P21	482	0.784	63.8	60.1	651.0	643.0	250	247	481
R13P22	477	0.833	61.7	59.6	651.0	645.0	247	245	476
R13P10R	467	0.846	62.6	58.2	644.0	640.3	240	238	489
R12P01	532	0.795	65.7	62.8	650.5	643.7			427
R12P09	540	0.849	72.0	66.1	649.5	644.5			433
R12P20	537	0.812	69.2	62.3	651.5	645.0			405
R11P01	597	0.868	75.9	69.7	650.2	644.7			383
R11P08	602	0.845	74.4	68.0	649.8	644.0			387
R11P19	597	0.810	77.2	73.2	650.6	644.0			403

Figure 2.11 - Typical Strain Gage Calibration Curve (R13P21)

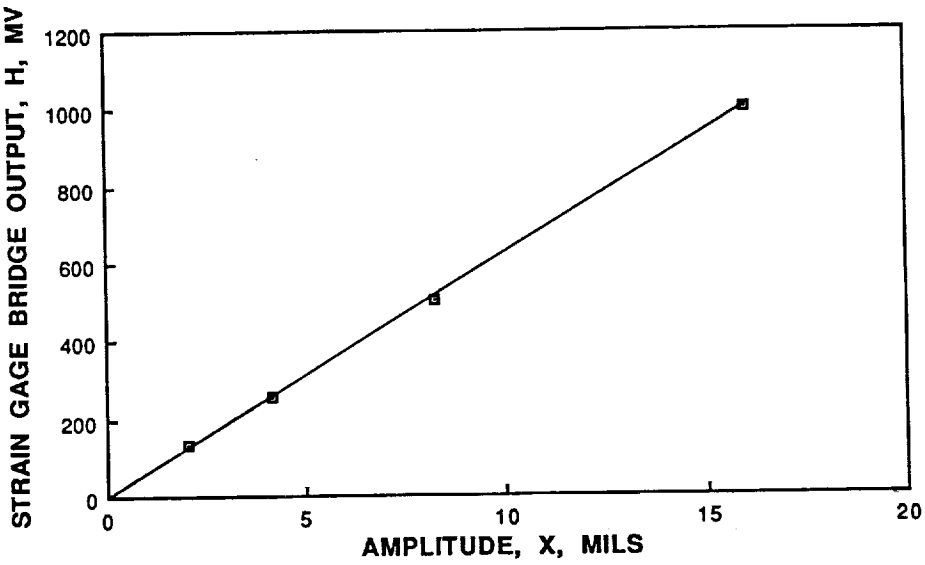

direction of maximum strain sensed by the radial gage. The dental floss was then cut by gently applying the edge of a razor blade. The resulting signal was recorded, and the resulting vibration frequency and damping were then calculated by a signal processor. Figure 2.12 is a typical vibration decay curve used for dynamic calibration. Table 2.10 and Figure 2.13 show comparisons of natural frequency and damping obtained from bench tests (Westinghouse) and Injector tests (Rocketdyne); in addition, comparisons are also made with values calculated from post-processing of actual air flow tests performed at MSFC. The upper portion of Figure 2.13 clearly shows the natural frequency increase over rows 13 through 11 due to the LOX post decreasing length; in addition, a fairly good agreement exists among the three sources. The bottom portion of Figure 2.13 shows damping; notice that in some cases inconsistencies of up to 20% are present. The exact nature of such differences has not been investigated in detail, however it is speculated that differences between bench and injector tests are probably due to installation methods (torque values on retainer nuts and application of Loctite material on threads), whereas the typically higher damping observed during air flow tests is likely to be caused by the added mass of the fluid. The damping values shown for air flow tests (MSFC) are from a single blowdown run chosen at random; it is to be expected that further spectral analysis of the strain response recorded for each LOX post may show trends in the variation of damping with flow rate and pressure.

Figure 2.12 - Typical Vibration Response Obtained from LOX Post Dynamic Calibration Tests

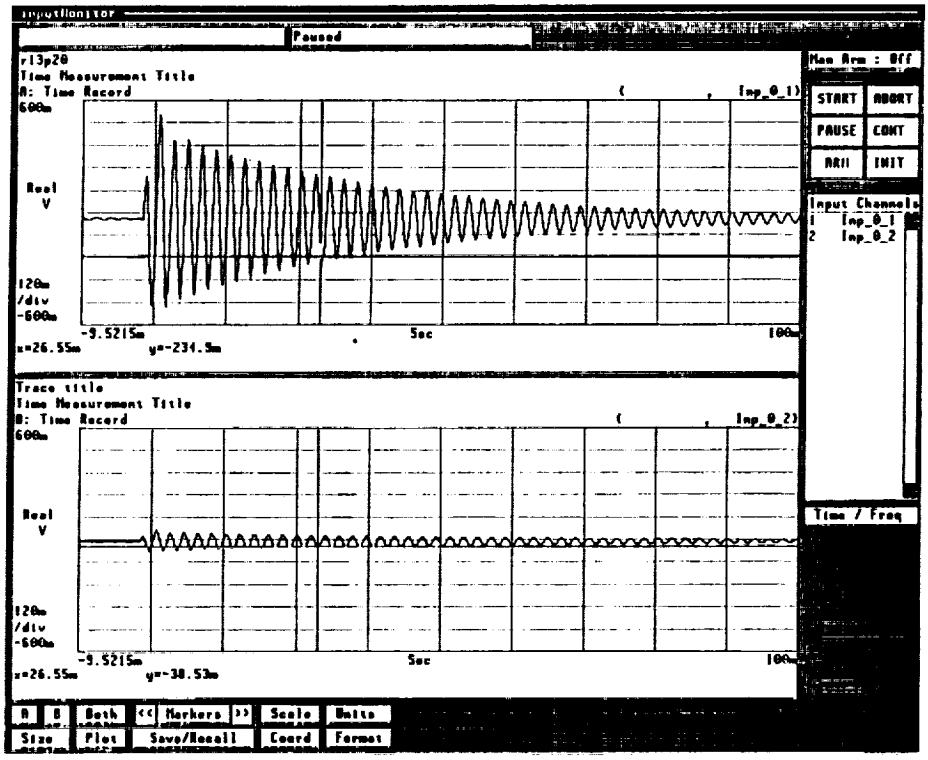

RI/RD 91-157

Table 2.10 - Comparison of Model Super-Post Frequency and Damping Obtained from Bench Tests (Westinghouse), Injector Tests (Rocketdyne) and Air Flow Tests (MSFC)

LOX Post	Westinghouse fn (Hz) Bench	RK fn (Hz) Injector	MSFC fn (Hz) Air Flow Test	Westinghouse Damping % Bench	RK Damping % Injector	MSFC Damping % Air Flow Test
R13P85	-	495	470.0	-	0.839	0.710
R13P01	470	453	467.5	0.825	1.069	0.960
R13P02	470	463	472.5	0.837	0.927	1.060
R12P01	532	519	527.5	0.795	0.831	0.660
R11P01	597	575	585.0	0.868	1.053	1.030
R13P08	472	461	467.5	0.765	0.852	1.100
R13P09	480	479	480.0	0.790	0.874	1.040
R13P10	467	467	470.0	0.846	1.043	1.060
R12P09	540	524	530.0	0.849	0.892	0.940
R13P20	460	469	475.0	0.833	0.993	1.160
R13P21	482	468	472.5	0.784	1.026	1.300
R13P22	477	459	460.0	0.833	0.829	1.200
R12P20	537	520	525.0	0.812	0.901	0.810
	fn (Hz) 1st Bending Mode					

Figure 2.13 - Graphical Representation of Table 2.10

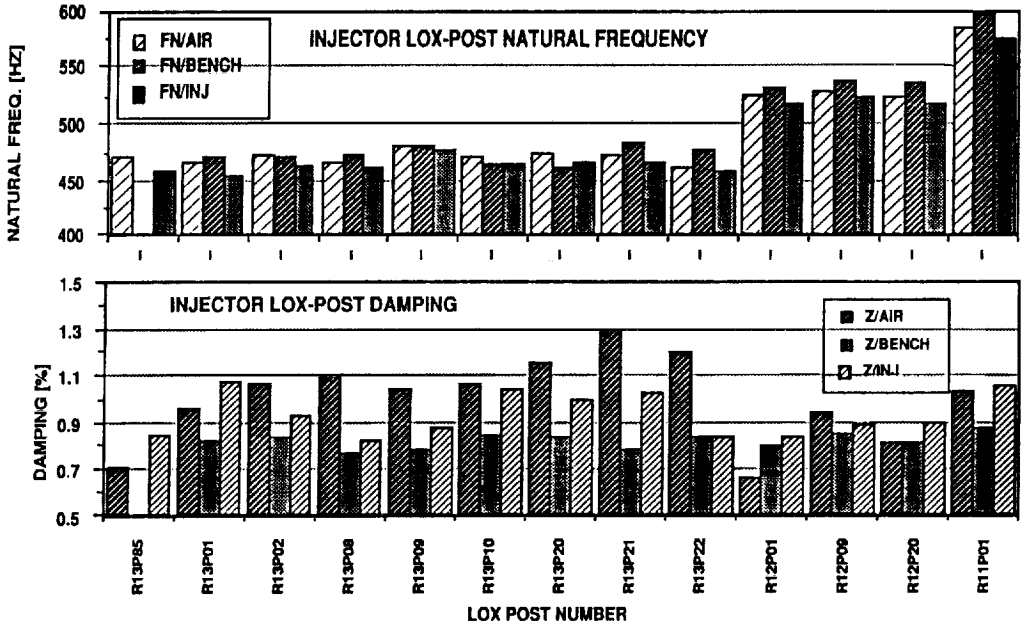

Data Acquisition System

Real time data acquisition is accomplished entirely through the use of two independent systems which are turned on-line just prior to activation of each blowdown run. During testing, the electrical signals transmitted from various sensors installed at locations of interest within the flow model are received and conditioned by each system and then stored on the respective storage facilities for post-processing. Selected parameters of critical interest are also subject to on-line monitoring through the use of oscilloscopes and digital displays. The two independent data acquisition systems are each dedicated to digital and analog operations.

Digital Data Acquisition System

This system acquires and processes data transmitted by pressure transducer type sensors. The pressure sensors, signal amplifiers and power sources are located in a self-contained and self-calibrating digital data scanner model 780-B manufactured by Pressure Systems Inc. (PSI). The digital data is acquired, processed and stored by means of a HP-900 central processing unit (CPU) computer system. Scanning rates of up to 100 samples per second can be achieved by this highly sophisticated system. Prior to each blowdown run, the HP-900 records and adjusts each data channel for zero-level response, and upon completion of each run it automatically processes all acquired data and produces a print-out in engineering units. A self-calibration routine is performed at the beginning of each day; ambient pressure and temperature are input prior to each run for proper conversion to absolute pressure units. The MSFC test facility is capable of simultaneous acquisition of several hundred pressure measurements discussed in greater detail in Reference (17). Several of these measurements were recorded in the course of each test and are in the custody of MSFC personnel for documentation purposes. Digital flow measurements pertinent to this program are listed in Table 2.6. These measurements have been selected on the basis that they provide the most essential flow parameters required to obtain an accurate description of the flow environment along the path included between the turbine simulator inlet and the Main Combustion Chamber discharge.

Analog Data Acquisition System

The Vespel model super-posts' structural response was measured by means of 25 SK13031CF350 strain gages mounted directly onto the surface of 13 LOX posts selected from three separate arrays.

A total of four strain gages were installed on each LOX post in a half-bridge configuration (2 active legs on each Wheatstone bridge). Each pair of strain gages was oriented radially outward and tangential to main injector row 13. Excitation voltage was provided by two HP 6114A power supplies mounted on instrumentation racks common to 25 Tektronix AM502 differential amplifiers. Figure 2.14 shows a circuit diagram representing a typical electrical interface between the strain gage instrumentation and the data acquisition system. The analog signal output was electronically stored for post-processing by means of two Ampex PR2230 FM tape recorders, each capable of accommodating 14 tracks of data. An IRIG generator was also used to provide a common time signal on one track of each tape recorder. The IRIG time was synchronized with the digital data acquisition system clock.

A maximum of 13 channels were simultaneously monitored and recorded in the form of time histograms by means of strip chart recorders. Two of the channels monitored on strip charts were also monitored in the frequency domain by means of a HP 3562A signal processor, which provided on-line Power Spectral Density (PSD) displays of lift and drag gages exhibiting the largest response amplitudes; a plotter was used for hard copy storage. The same parameters were also displayed on a dual channel digital oscilloscope in the form of Lissajous diagrams (orbit plots). The Lissajous and PSD displays were carefully monitored during each blowdown run in order to be able to signal a test abort in case of excessive vibration amplitudes of fluid-elastic nature. For the first 64 runs (run 1/0 through 43/0), the excitation voltage used for all strain gages was 3.0 volts, with a gain factor of 1000 set on all amplifiers. The gain was then reduced to 500 for the remaining 22 runs (run 42/4 through 62/1) due to the higher mass flow rates used. Not all of the runs just mentioned were considered acceptable; only those listed in the test matrix (see section 3.0) were used for data analysis. All post-processing was performed by means of a MASSCOMP 5500 computer system.

Figure 2.14 - LOX Post Strain Gages Instrumentation Circuit Diagram

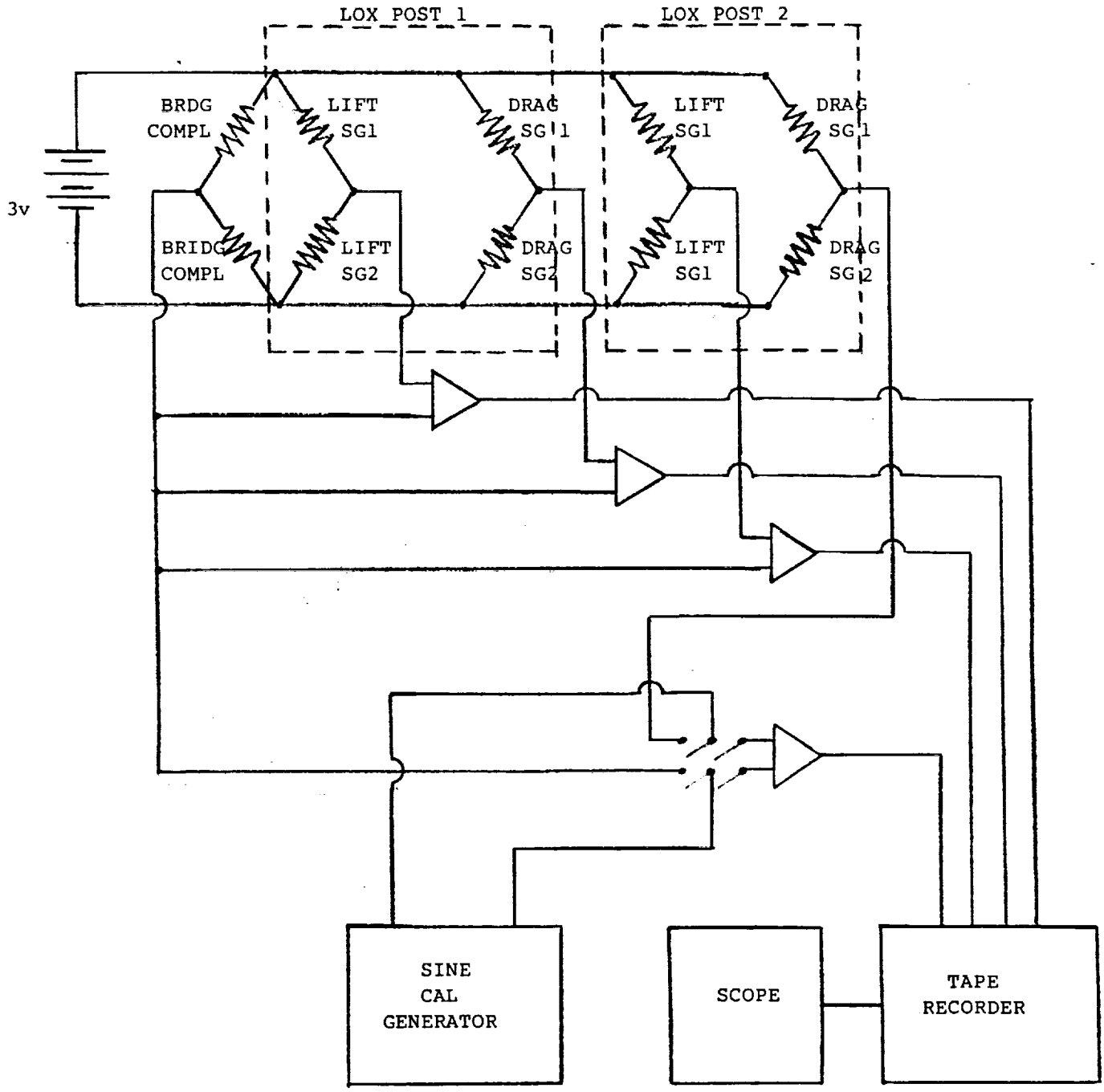

RI/RD 91-157

3.0 ANALYSIS AND DISCUSSION OF EXPERIMENTAL RESULTS

In the experimental phase of the program nearly 100 test runs were carried out at various flow rates and back pressures in an attempt to find the necessary flow conditions suitable for fluidelastic excitation of the instrumented Vespel super-post arrays. The model powerhead inlet and discharge flow conditions were varied in order to cover a sufficiently wide range of reduced velocities and fluid densities, which are the key flow parameters in the fluidelastic excitation domain.

Following a discussion on the test procedures, test matrix, data management, and the techniques utilized in the course of the experiments, the discussion will be then shifted toward the analytical tools used to reduce the raw experimental data. The results obtained from the data analysis will then be interpreted in terms of the high frequency structural response of the model super-posts as well as the steady-state information which characterizes the overall flowpath within the powerhead.

Finally, a relatively simple analytical model of the flowpath, simulating the flow between the simulated fuel turbine inlet and the Main Combustion Chamber (MCC) throat, will be presented for the geometry actually tested and for other possible modifications. This will be done in an attempt to explore the possibility of attaining higher flow regimes which might be better suited for inducing an unstable condition of the model LOX posts within the current test facility capabilities.

TEST PROCEDURES

Due to the relatively fragile construction of the Vespel super-posts and the uncertainties associated with the actual flow conditions required to induce LOX post instability, the incremental flowrates and pressures applied to the test article were selected very cautiously, in fear of inflicting premature damage to the model posts. The primary objective throughout the experimental phase was to establish flow conditions necessary to induce transition in LOX post vibration amplitudes from a linear to an exponential increase, as a function of flow energy input. In this section, the experimental techniques as well as the test matrix utilized in the course of the experimental program are presented.

Test Matrix

A record of all test runs completed in the experimental phase is shown in Table 2.11.

Experimental Techniques

As mentioned in previous sections, searching for a stability threshold in the fluid-elastic domain requires adjustments of two essential parameters: the reduced velocity and the fluid density. In an academic sense, the reduced velocity is defined in terms of the effective velocity (Uen) which, for cylindrical array configurations, would be equivalent to the gap velocity (flow velocity between two adjacent posts). However, for practical reasons, the average of the velocities measured at the exit of each fuel-side transfer duct was used instead of the true gap velocity . The transfer duct velocity was varied by controlling the mass flow rate through the air flow model. Conversely, the fluid density was controlled by the back pressure at the MCC by means of a control valve setting selection of 6%, 13%, 20% or 27.9% opening. The resulting effect can be seen in Table 2.11 which shows that the density was varied from less than 0.1 Lbm/Ft^3 to over 0.5 Lbm/Ft^3, despite the unexpected occurrence of a limitation in the transfer duct velocity to about 350 Ft/s. More details about the velocity limitation will be given later in this section.

As indicated earlier in this report, the structural response of a limited number of LOX posts was monitored in real time during the execution of each blowdown run. Due to the unavailability of additional equipment, a maximum of two channels at a time could be selected for on-line monitoring. First, it was necessary to identify a specific LOX post having the greatest potential for experiencing fluidelastic instability. The selection was made based on vibration amplitudes recorded on strip-chart amplitude histograms. The selected data channels were then input to an oscilloscope - for Lissajous (orbit) diagram display, and to the HP356A signal processor - for spectral density display. After each test, log entries were made to assess any possible changes in the behavior of the strain response through which an instability event could be detected and tracked. Moreover, logs were also maintained on the progression of strain response as a function of the velocity head (q). The HP-900 computer system made this task rather simple because of its ability to compute all of the basic aerodynamic parameters within minutes from shut-down. Data points were manually plotted after each run to ascertain whether the strain was behaving linearly with increasing q, or whether an exponential increase in strain response - similar to that observed in the channel tests (Figure 1.18), was about to occur. Unfortunately, an unstable condition was never attained in the course of this experimental phase.

Table 2.11 - Test Matrix

1	RUN	FUEL/LOX	Utd*SQRT(RHO)	Utd (ft/s)	M-dot n	M-dot s	Rho (lbm/ft3)	q (psi)	Ratio fuel/lo
2	13/0	31/30	69.1	236.4	6.2	2.4	0.0854	0.5149	2.5833
3	14/1	36/35	76.4	254.0	7.1	2.9	0.0905	0.6294	2.4315
4	15/1	41/40	83.0	268.6	7.8	3.3	0.0955	0.7429	2.3636
5	36/0	46/45	90.0	287.0	8.7	3.7	0.0983	0.8734	2.3514
6	19/0	51/50	99.0	303.0	9.9	4.1	0.1068	1.0569	2.4205
7	23/1	61/60	107.0	316.0	11.3	4.8	0.1147	1.2346	2.3542
8	27/0	71/70	117.9	329.0	13.1	5.5	0.1284	1.4989	2.3818
9	30/1	81/80	130.0	337.0	15.5	6.4	0.1488	1.8224	2.4219
10	37/1	86/85	133.0	343.5	16.2	6.7	0.1499	1.9075	2.4179
11	32/0	91/90	138.4	337.0	17.5	7.2	0.1687	2.0655	2.4306
12	33/0	96/95	141.0	335.0	18.5	7.8	0.1772	2.1438	2.3718
13	34/0	101/100	144.5	335.0	19.5	8.2	0.1861	2.2516	2.3780
14	35/0	106/105	149.0	338.0	20.5	8.4	0.1943	2.3940	2.4405
15	38/0	116/115	158.0	343.1	22.5	8.8	0.2121	2.6919	2.5568
16	39/0	126/125	163.0	339.0	24.5	10.3	0.2312	2.8650	2.3786
17	40/0	136/135	170.1	342.4	26.2	10.9	0.2468	3.1200	2.4037
18	41/0	146/145	176.5	344.8	28.1	11.9	0.2620	3.3592	2.3613
19	42/5	156/155	180.8	339.3	29.9	12.9	0.2839	3.5249	2.3178
20	43/0	166/165	186.3	348.8	30.9	13.4	0.2853	3.7426	2.3060
21	44/1	176/175	191.6	342.6	33.3	14.3	0.3128	3.9586	2.3287
22	45/0	186/185	198.4	344.2	35.6	15.3	0.3322	4.2446	2.3268
23	46/0	197/195	207.7	349.6	38.3	16.1	0.3530	4.6518	2.3789
24	47/0	208/205	210.2	346.7	39.6	16.8	0.3676	4.7645	2.3571
25	48/0	218/215	219.1	352.5	42.3	17.7	0.3863	5.1765	2.3898
26	49/0	228/225	224.1	351.1	44.5	18.5	0.4074	5.4155	2.4054
27	50/0	238/235	230.0	353.4	46.5	19.3	0.4236	5.7044	2.4093
28	51/0	248/245	231.7	348.8	47.8	20.0	0.4413	5.7890	2.3900
29	52/0	258/255	237.6	351.4	49.9	20.9	0.4572	6.0876	2.3876
30	53/0	268/265	242.0	353.3	51.5	21.8	0.4692	6.3151	2.3624
31	60/0	278/275	242.9	342.0	no data	no data	0.5044	6.3622	no data
32	61/0	288/285	248.4	347.3	55.2	23.3	0.5116	6.6536	2.3691
33	62/1	298/295	256.6	353.0	58.0	24.3	0.5284	7.1001	2.3868

EXPERIMENTAL RESULTS

The test matrix originally designed for this test program specified a fixed hardware configuration and a fairly extensive regime of mass flow rates and back pressures. This was intended to be a systematic approach to finding the correct combination of reduced velocity and density necessary to induce an unstable condition affecting at least one of the three LOX post arrays under study. Table 2.3 was generated as an aid to this purpose, thus greatly simplifying the experimental task to merely finding the correct combinations of U_{cn} and ρ_o approaching the values listed in the table. The model LOX posts were also designed to experience instability at flow conditions within the operating range of the test facility, however a number of assumptions were necessary to analytically predict the approximate position of the instability threshold (and thus the values in Table 2.3) applicable to the model design. Unfortunately, the analytical prediction sought was also a test objective, thereby creating a situation where the resulting analytical predictions could only be as accurate as the assumptions made during the design phase. After numerous attempts to expose at least one of the model super-posts to fluidelastic instability, it was found that this condition could not be achieved within the operating range of the air flow test facility, or the design constraints of the model LOX posts.

To help illustrate the situation, one of the most critical assumptions needed was the threshold instability constant β; Table 2.1 lists some of the values used to generate Table 2.3. As will be shown in this section, the value of β for row 13 LOX post No.85 (in-line array) calculated from the experimental data is 12.2 as opposed to 3.4 - given in Table 2.1. The actual value will be greater than 12.2 because instability was not observed at that point, and the maximum operating limit of the test facility had been reached. Consequently, the predicted stability threshold listed in Table 2.3 will be more than four times greater than originally believed.

In this section, the experimental data characterizing the flow field in the vicinity of the LOX posts, as well as their structural response, will be presented. The issue concerning the present lack of an unstable response and how it can be applied to the SSME will then be addressed. Finally, analytical methods used to determine the feasibility of attaining instability within the current flow facility constraints will also be presented, as a database for possible future attempts to accomplish the initial objective.

Hardware Configurations

The Hot Gas Manifold air flow model configuration utilized in the course of these tests consisted of hardware components simulating a Full Power Level (FPL), Phase II powerhead. The hardware simulating the High Pressure Fuel Turbine (HPFT), included a single-stage turbine simulator screen needed to reproduce a flow resistance equivalent to the SSME turbine rotors; the open area of the screen is approximately 9 in^2 (referred to as "screen No.1"). A swirl vane assembly was mounted downstream of the plane of the screen to simulate the second stage nozzle exit velocity angle. Screen No. 1 was installed for test runs 1 through 62. Upon completion of the test runs prescribed by the test matrix, this screen was replaced with a two-stage unit with an open area of approximately 20 in^2 (referred to as "screen No.2"). Due to space limitations, it was necessary to remove the swirl vane assembly. Screen No. 2 was used for runs 63 through 66.

Table 3.1 lists geometric areas pertinent to locations along the flow path extending from the fuel turbine simulator screen to the MCC. Stations 1 through 5 are shown on the HGM model in Figure 2.9, and are also defined as follows:

A1 : Turbine Simulator Screen
A2 : Fuel Transfer Ducts Exit Plane
A3 : Injector LOX Post Face Plate Retainers
A4 : MCC Combustor
A5 : MCC Throat

Table 3.1 - HGM Air Flow Model Geometric Areas Along Flow Path

CASE NO	GEOMETRIC AREAS (IN2)				REMARKS
	A1	A2	A3	A5	
1	9.08	44.74	42.72	66.96	SCREEN No. 1 (TESTS 03-62)
2	19.77	44.74	42.72	66.96	SCREEN No. 2 (TESTS 64-66)
3	19.77	44.74	85.44	83.40	262-300 INJECTOR SLEEVES AND MCC VALVE REMOVED
4	19.77	44.74	42.72	83.40	MCC VALVE REMOVED

Description of Flow Field

A sufficient number of measurements were recorded to provide the basic flow parameters - pressure, temperature, density and velocity - at locations along the flow path described in Table 3.1 and Figure 2.9. During the series of runs for which screen No. 1 was installed in the HGM model, an anomaly was encountered in the behavior of the one-dimensional transfer duct exit velocity as a function of flow rate. Figure 3.1 (case 1) shows the transfer duct velocity leveling off at about 350 Ft/s for fuel flow rates greater than 30 Lbm/s. After determining that the Mach number associated with the flow passing through screen No. 1 was sonic, an attempt was made to increase the transfer duct velocity by opening the fuel turbine simulator screen flow area by installing screen No.2, however no improvement was achieved, as indicated by Figure 3.1 (case 2). The Mach number was calculated by means of a one-dimensional algorithm at stations 1, 2, 3 and 5 (Table 3.1) in an effort to provide an explanation for this behavior. The Mach number plotted as a function of fuel flow rate in Figure 3.2 for screen No. 1, shows the turbine simulator screen choking at about 20 Lbm/s fuel flow rate, with the MCC throat choking later at about 30 Lbm/s. The Mach number through the injector fuel sleeves is shown to be sufficiently large to suggest a possible choking condition also at that location. A comparison between Figure 3.2 and 3.3 shows that a large decrease in Mach number through the turbine simulator screen had virtually no effect on the flow velocity in any of the other locations considered. This observation suggested that the transfer duct velocity was being controlled primarily by the high Mach number flow through the injector sleeves. A confirmation of this was later found by using the computer model to predict the transfer duct velocities for enlarged flow areas at stations 3 and 5 (case 3), and at station 5 only (case 4). Figures 3.4 and 3.5 respectively show the resulting transfer duct exit Mach number reaching its highest value for case 3 (injector sleeves and MCC valve removed), corresponding to a velocity of nearly 550 Ft/s, as opposed to 350 Ft/s attainable with the nominal injector configuration. Table 3.2 summarizes these findings as a function of total facility flow rate. Figures 3.1 through 3.5 are plotted as a function of fuel flow rate. Insofar as the critical velocity for the onset of fluidelastic instability is concerned, it is interesting to note from Table 3.2 that the parameter $U\rho^{1/2}$ reaches values far greater than those predicted in Table 2.3, even prior to crossing the stability threshold.

Figure 3.1 - Transfer Duct Exit Velocity Variation as a Function of Fuel Flow Rate (case 1)

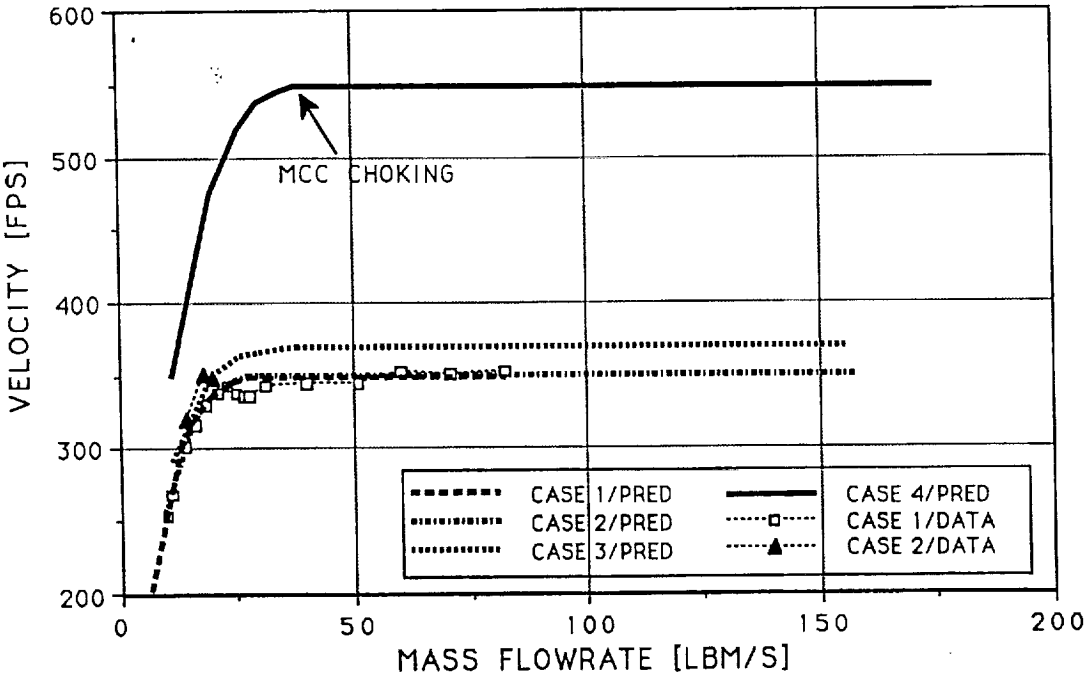

Figure 3.2 - Mach Number Variation at Stations 1 through 5 as a Function of Fuel Flow Rate (case 1)

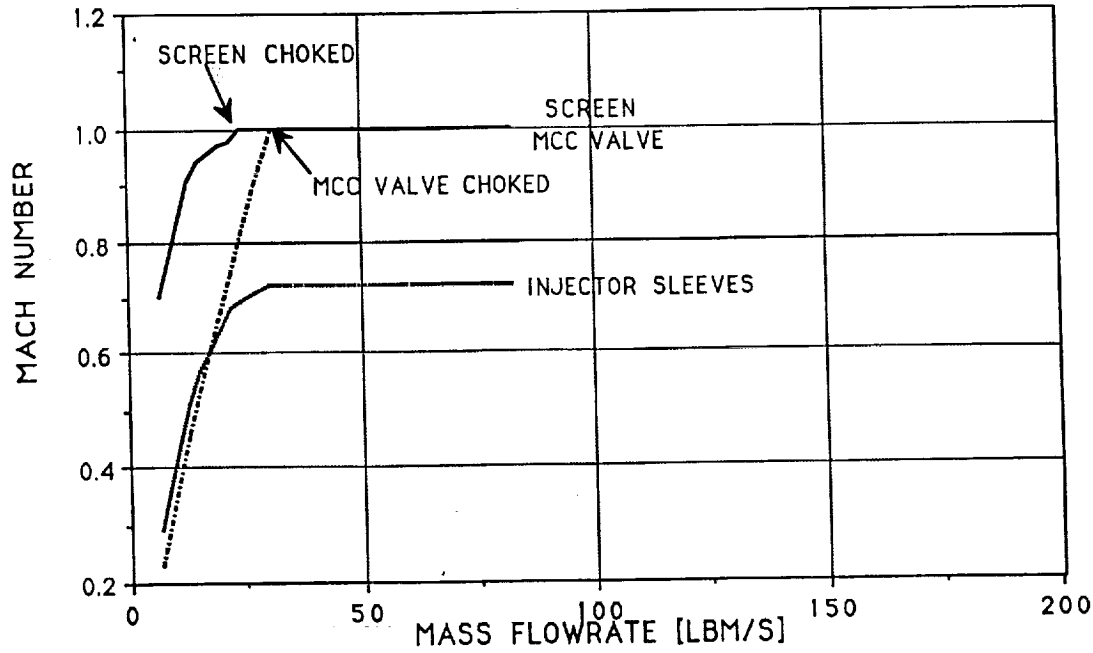

Figure 3.3 - Mach Number Variation at Stations 1 through 5 as a Function of Fuel Flow Rate (case 2)

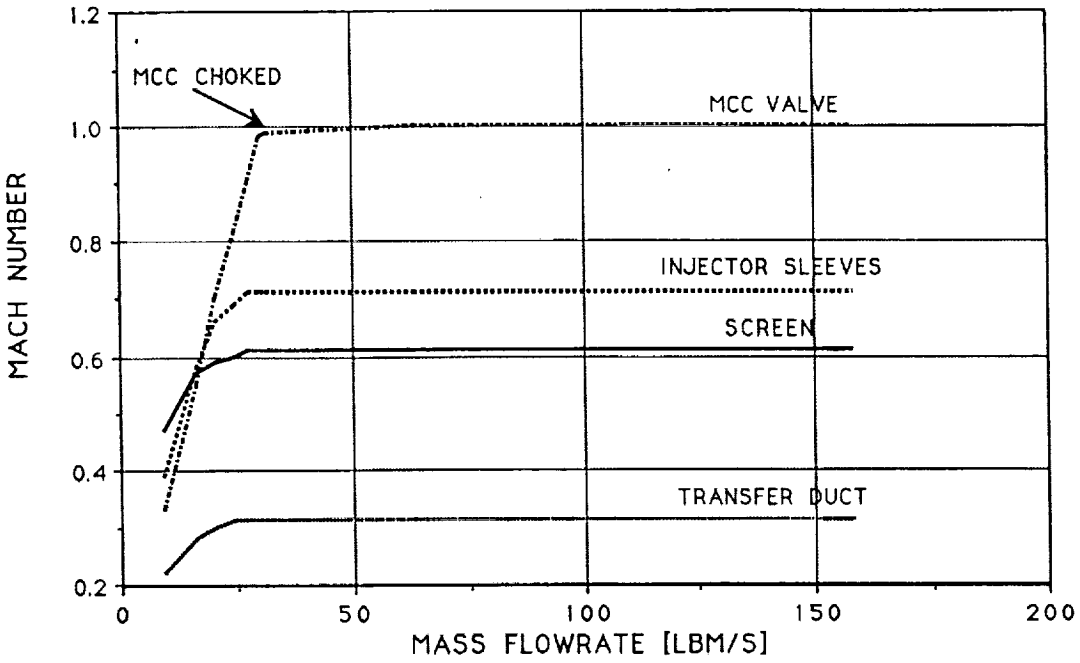

Figure 3.4 - Mach Number Variation at Stations 1 through 5 as a Function of Fuel Flow Rate (case 3)

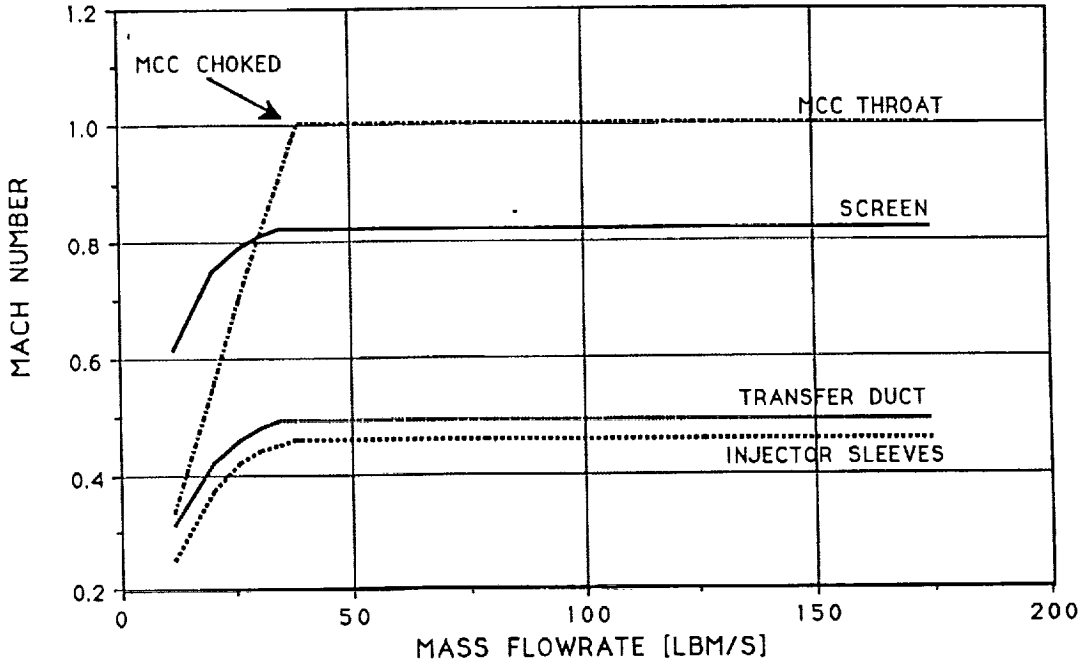

Figure 3.5 - Mach Number Variation at Stations 1 through 5 as a Function of Fuel Flow Rate (case 4)

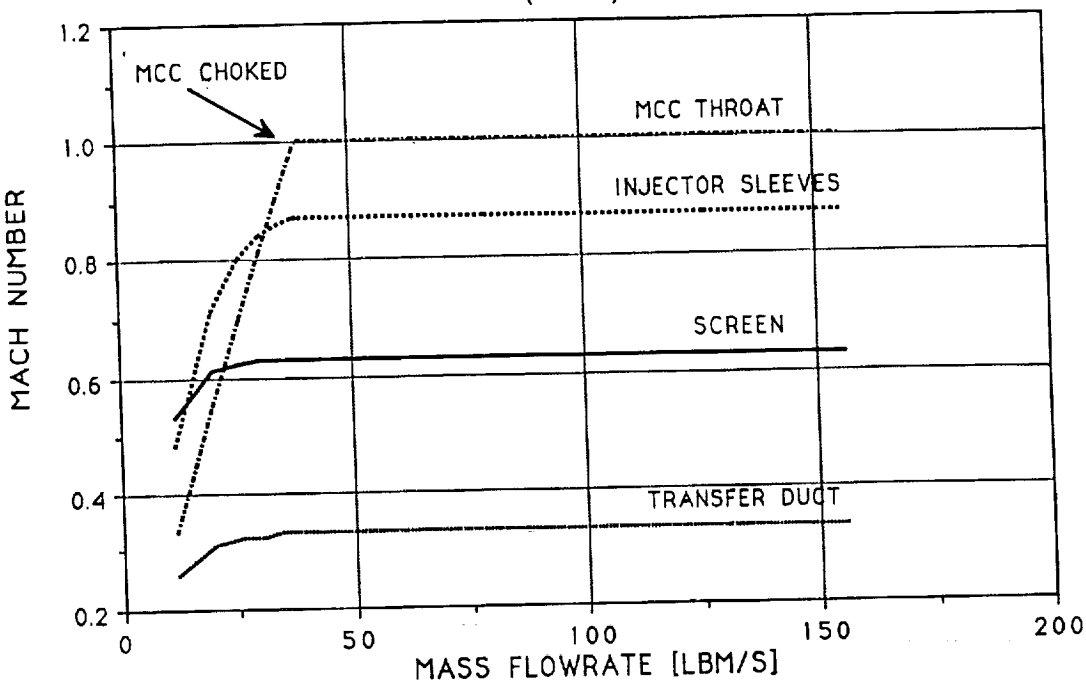

Table 3.2 - Effects of Geometry on Transfer Duct Exit Velocity

PREDICTED VALUES WITH MAX. INLET PRESSURE = 300 PSIA

CASE NO	FLOWRT (LBM/S)	T.D.VEL (FPS)	T.D. q (PSI)	T.D. U $\sqrt{\rho}$	REMARKS
1	82	348	7.0	253	SCREEN No. 1
2	152	350	13.1	348	SCREEN No. 2
3	175	548	23.5	465	SCREEN No. 2
4	156	369	14.1	362	SCREEN No. 2

Injector LOX posts Response

As stated at the beginning of this section, LOX post instability was not detected over the operating range of the test facility. The type of response exhibited by all instrumented LOX posts was consistently typical of turbulent excitation. A representative amplitude histogram obtained for LOX post 9 on row 13 (33° array) in the tangential direction (R13P09t) is shown in Figure 3.6; this plot

also represents the maximum amplitude levels recorded in the course of the experimental phase. It is relevant to note that the signal is random, with maximum peak-to-peak fluctuations of about 16 Lbf. Figure 3.7 is an RMS version of the trace in Figure 3.6, showing an average RMS load of 2.8 Lbf-rms and no sinusoidal behavior. This value is in agreement with the composite spectrum shown in Fig. 3.8, which shows the first 4 modes of vibration in the 0-2.5 kHz spectrum. The first mode of 470 Hz agrees very well with bench and injector calibration tests performed prior to air flow testing. The damping reported in Table 2.10 was calculated from similar curves using the half-power method.

Figure 3.6 - Typical LOX Post Amplitude Histogram (R13P09T)

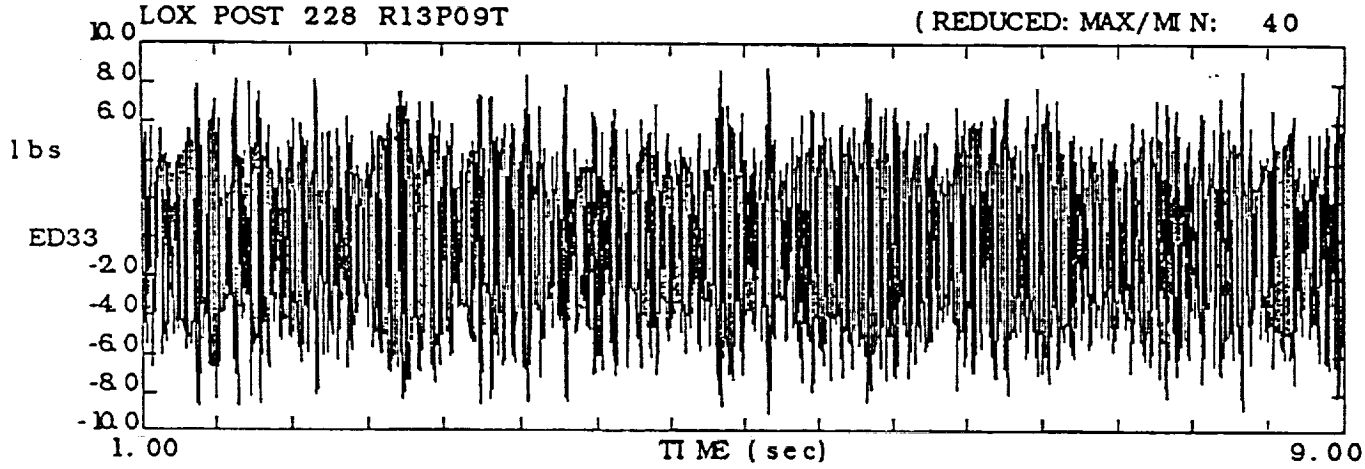

Figure 3.7 - RMS Format of R13P09T Amplitude Histogram

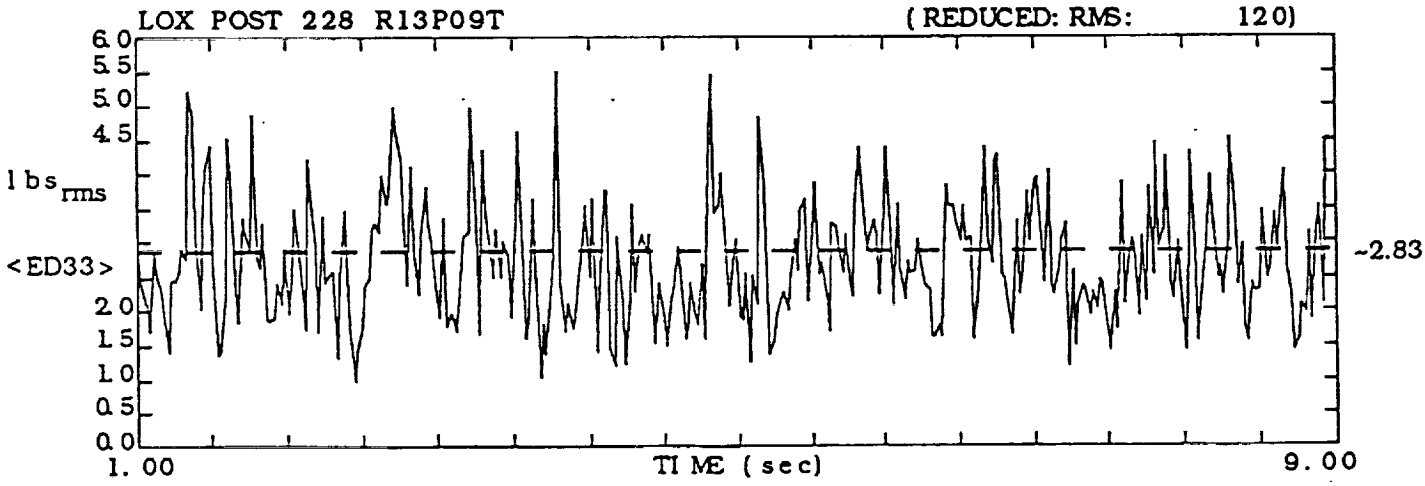

Figure 3.8 - Power Spectral Density Of LOX Post R13P09T

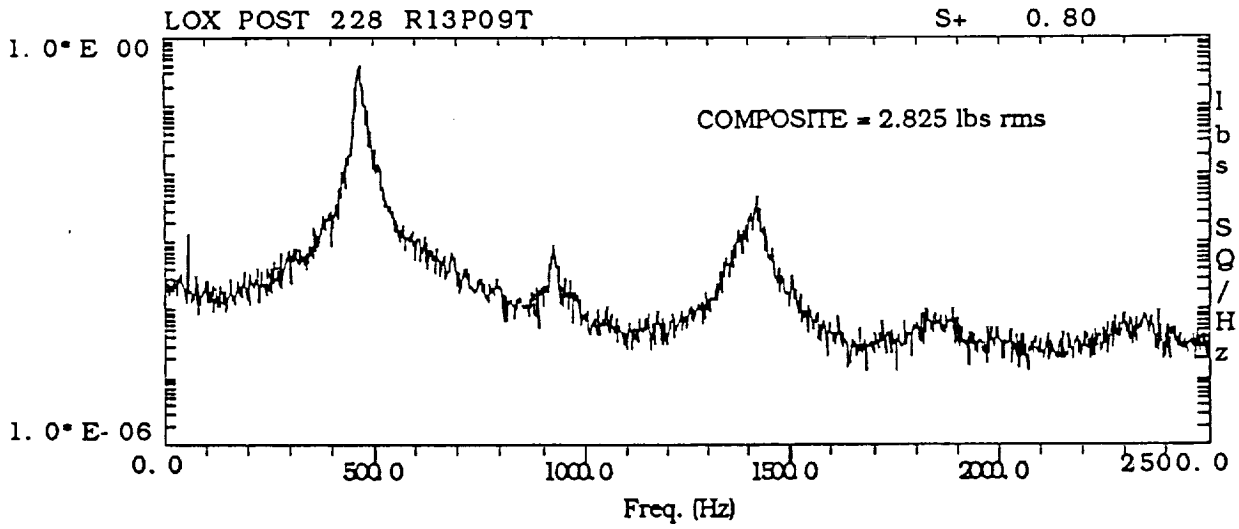

RMS load response of the remaining LOX posts is shown in Figures 3.9 through 3.11 for 0°, 33° and 85° respectively. The majority of the data points plotted appear to follow a linear behavior for values of q greater than 2 psi, thereby exhibiting a non-zero y-intercept. This behavior was not expected, based on data obtained from two-duct tests described in section 1.0 (see Figure 1.23). The model LOX posts used in the two-duct tests are very similar to those used in this test, except for the steel tips and the steel upper and lower shrouds installed in this injector. Differences in the mode shapes between the two design versions are therefore expected, however the mode shape is unlikely to be the cause of a non-linearity in the strain response. Although investigation on this issue is not complete, it is speculated that a possible variation in damping due to interaction between the Loctite material and the steel shrouds may be a possible cause for this behavior. By application of the half-power method to individual strain response PSD curves taken at selected time slices corresponding to increasing flow rates may reveal the true behavior of the damping coefficient. On the upper portion of the RMS strain response curves, sudden exponential increase in amplitude, indicative of a fluid-elastic excitation mode is not easily discerned. The 33° array exhibits a slightly different behavior than the other two arrays due to the last three or four data points. As Figure 3.10 shows, it would appear that posts R13P08R and R13P09R may have the tendency to increase at a higher slope than other data points. It is difficult, however, to make a precise assessment based on a few data points. Moreover, correlation functions have been generated for these and other data points, showing no sign of a lock-in phenomenon. The analog data presented in this section has been analyzed by means of the Masscomp 5500 computer. Strain gage instrumentation sensitivities for calibration purposes are listed in Table 3.3.

Figure 3.9 - Main Injector Super-Post Model Response with Transfer Duct Velocity Head (0° position)

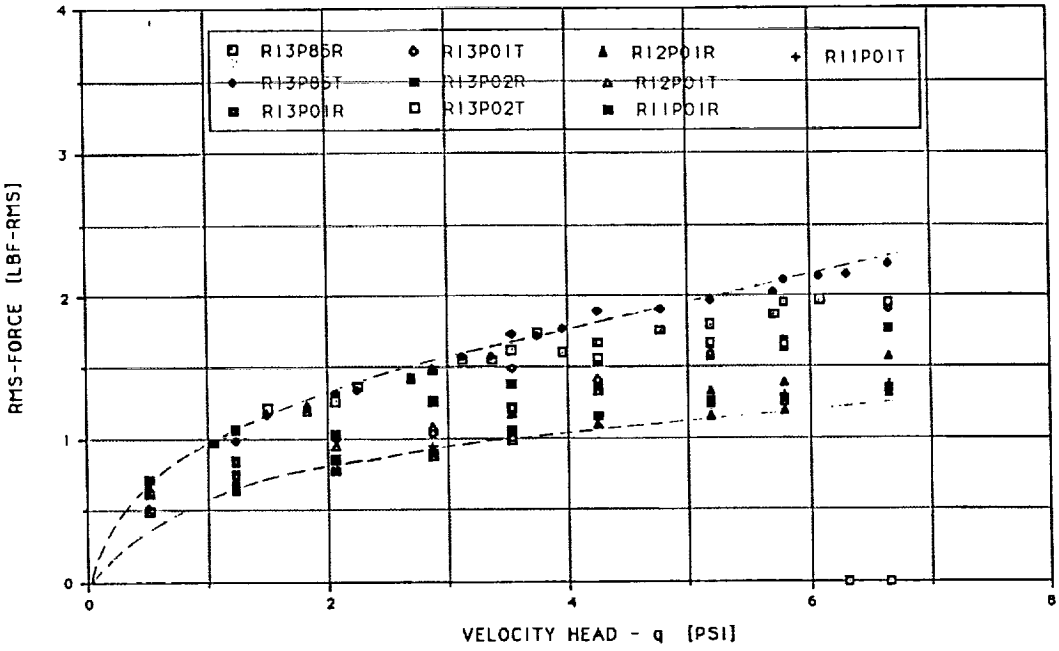

Figure 3.10 - Main Injector Super-Post Model Structural Response with Transfer Duct Velocity Head (33° position)

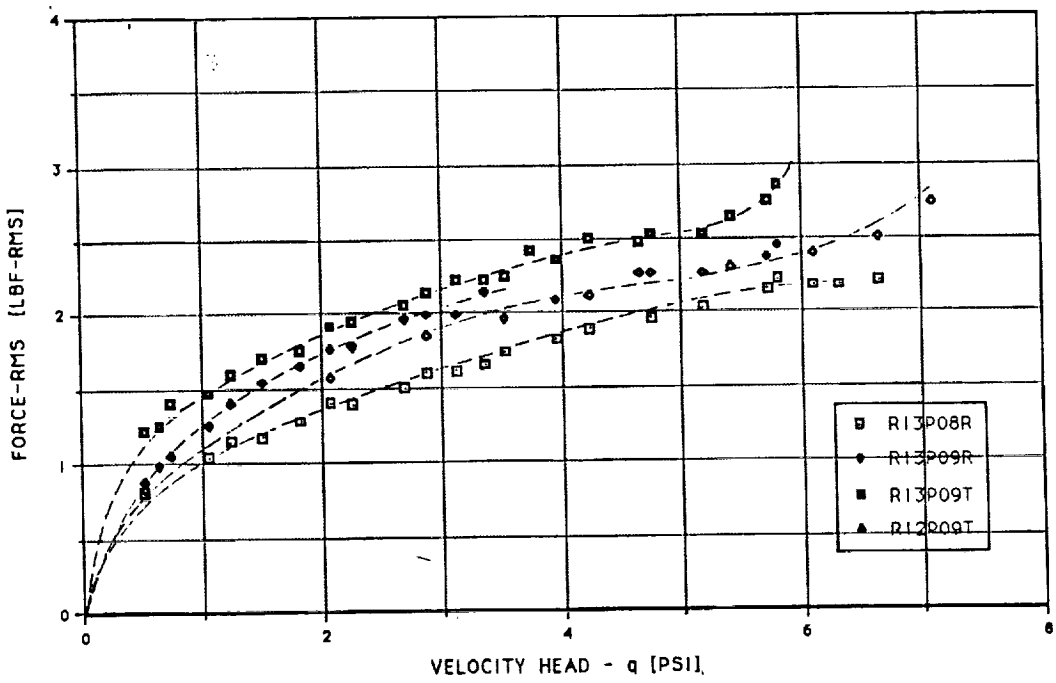

Figure 3.11 - Main Injector Super-Post Model Response with Transfer Duct Velocity Head (85° position)

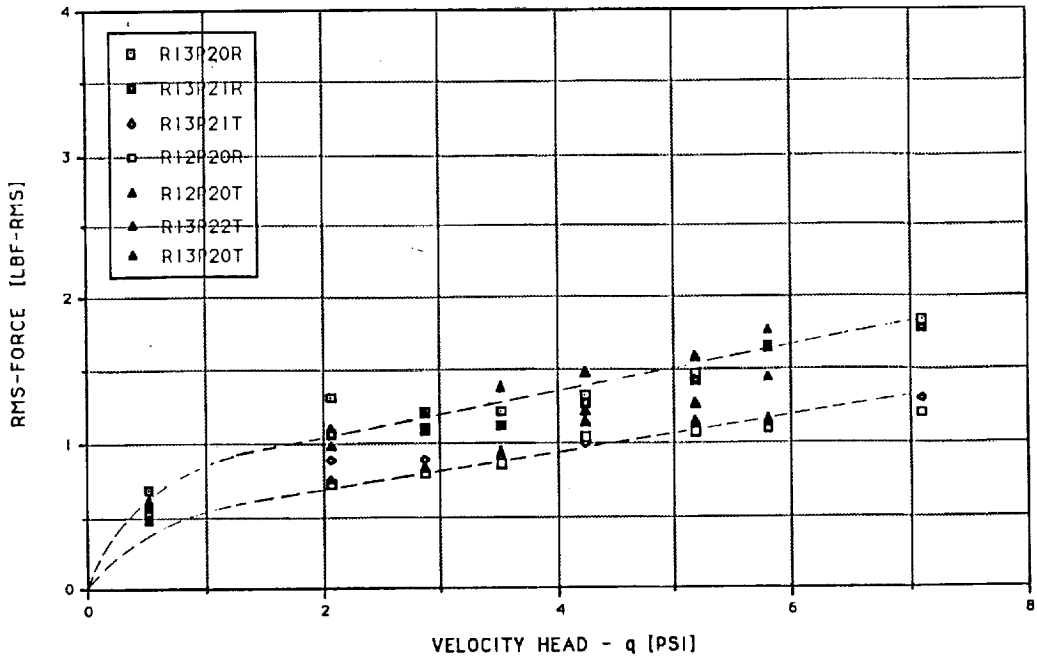

Stability Diagrams

Figure 3.12 shows the stability diagram resulting from experimental data gathered from the injector tests[4]. Reduced velocity - in terms of transfer ducts exit velocity, rather than gap velocity - is shown on the ordinate, and damping parameter on the abscissa. The square symbols represent blowdown runs in the upper range of the parameter $U\rho^{1/2}$. The square symbol to the extreme left of the family of points was chosen as the uppermost stability boundary (curve "A") because it represents the blowdown run with the highest velocity and density data (run 62/1, with q = 7.1 psi), combined with the lowest natural frequency and damping found in Figure 2.13 (LOX post R13P85). This point was chosen because it represents the highest measured "stable" boundary; the location of the actual stability threshold, however, is unknown due to the absence of an unstable LOX post response during test. The second boundary line, labeled "B", represents the lower edge of the envelope which encompasses all LOX post damping and natural frequencies for the same q as in curve A. The specific LOX post with the highest natural frequency and damping is post R11P01. The maximum post-to-post variation of the highest stable boundary recorded is thus between $\beta = 8.2$ and $\beta = 12.2$.

[4] In Figure 3.12, K is used to designate the stability constant normally designated by β in other portions of the report.

Table 3.3 - Strain Gage Instrumentation Sensitivities Used for Analog Data Post-Processing

TAPE #2													
	INJ. SENS.	SEN. (lbs/v)	YRMS(v)	XRMS (v)	XRMS (v)	XRMS (v)	XRMS(v)	XRMS (v)	KEY#(lbs/v)	KEY#(lbs/v)	SEN. (lbs/v)	XRMS (v)	KEY#(lbs/v)
LOX POSTS	(mV/lbs)	Exlcat = 3V		day 199	day 200	day 206	avg	day 208	D199-207	D 208	Exclt. = 1.5V	day 211	D211-215
R13PO9R	472	847.5	0.00356	1.027	1.102	1.038	1.056	0.567	2.86	5.32	1694.9	1.179	5.12
T	472	847.5	0.00356	1.013	1.056	1.009	1.026	0.507	2.94	5.95	1694.9	1.089	5.54
R13P10R	514	778.2	0.00356	0.997	1.061	1.000	1.019	0.501	2.72	5.53	1556.4	1.120	4.95
T	514	778.2	0.00356	1.017	1.068	1.009	1.032	0.511	2.69	5.43	1556.4	1.101	5.03
R12P09T	470	851.1	0.00356	1.040	1.064	1.121	1.075	0.567	2.82	5.34	1702.1	1.039	5.83
R13P20R	507	788.9	0.00356	1.000	1.044	1.091	1.045	0.537	2.69	5.23	1577.9	1.008	5.57
T	507	788.9	0.00356	0.992	1.031	1.079	1.034	0.520	2.72	5.40	1577.9	0.992	5.66
R13P21R	520	769.2	0.00356	1.035	1.055	1.101	1.064	0.538	2.57	5.09	1538.5	1.055	5.19
T	520	769.2	0.00356	1.149	1.040	1.056	1.082	0.567	2.53	4.83	1538.5	1.092	5.01
R13P22R	464	862.1	0.00356	1.114	1.002	1.022	1.046	0.537	2.94	5.72	1724.1	1.049	5.85
T	464	862.1	0.00356	1.137	1.032	1.050	1.073	0.520	2.86	5.91	1724.1	1.041	5.90
R12P20R	422	947.9	0.00356	1.149	1.021	1.041	1.070	0.538	3.15	6.27	1895.7	1.045	6.46
T	422	947.9	0.00356	1.032	1.124	1.062	1.073	0.526	3.15	6.41	1895.7	1.007	6.71
									C*D/H	C*D/I			L*D/M
TAPE #1													
	INJ. SENS.	SEN. (lbs/v)	YRMS(v)				XRMS(v)	XRMS (v)	KEY#(lbs/v)	KEY#(lbs/v)	SEN. (lbs/v)	XRMS (v)	KEY#(lbs/v)
LOX POSTS	(mV/lbs)	Exlcat = 3V					D199-207	day 208	D199-207	D 208	Exclt. = 1.5V	day 211	D211-215
R13P85R	490	816.4	0.00356				1.269	0.686	2.29	4.36	1632.6	1.065	5.46
T	490	816.4	0.00356				1.163	0.506	2.50	5.74	1632.6	1.007	5.77
R13P01R	534	749.1	0.00356				1.554	0.531	1.72	5.02	1498.0	1.017	5.24
T	534	749.1	0.00356				1.207	0.506	2.21	5.27	1498.0	1.016	5.25
R13PO2R	522	766.3	0.00356				1.116	0.537	2.45	5.08	1532.6	1.073	5.08
T	522	766.3	0.00356				1.139	0.540	2.40	5.05	1532.6	1.036	5.27
R12PO1R	475	842.1	0.00356				1.050	0.559	2.86	5.36	1684.2	1.032	5.81
T	475	842.1	0.00356				1.184	0.587	2.53	5.11	1684.2	1.077	5.57
R11PO1R	460	869.3	0.00356				1.159	0.525	2.67	5.89	1739.1	1.087	5.70
T	460	869.3	0.00356				1.053	0.503	2.94	6.15	1739.1	1.043	5.94
R13P08R	532	751.9	0.00356				1.051	0.508	2.55	5.27	1503.8	1.060	5.05
T	532	751.9	0.00356				1.025	0.539	2.61	4.97	1503.8	1.080	4.96
									C*D/H	C*D/I			L*D/M
		NOTE: Days 199-207 = RUNS 1/0 TO 43/0					Gain = 1000	Excit = 3v					
		Days 208 = RUNS 44/0 TO 59/1					Gain = 500	Excit = 3v					
		Days 211-215 = RUNS 60/0 TO 66/0					Gain = 1000	Excit = 1.5v					

Figure 3.12 - SSME Main Injector Super-Post Stability Diagram

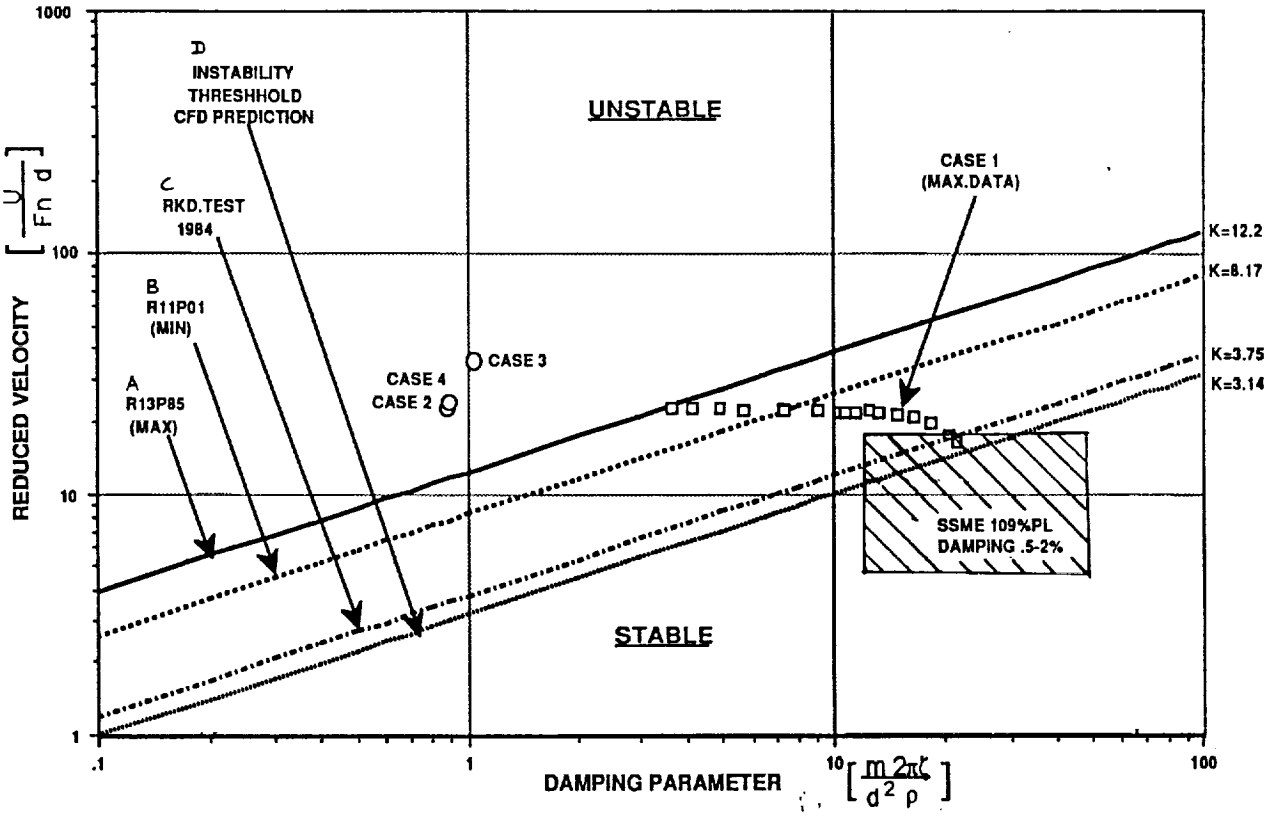

On the same figure, a comparison is also shown with an actual instability threshold obtained form channel tests conducted at Rocketdyne in 1984 (curve "C"). In the course of these tests instability was actually achieved, however the threshold is far below the uppermost stable boundary obtained for three-duct shieldless injector super-posts. The value of the instability constant was reported as 3.75, which is over three times lower than that obtained from present stable tests. It should be also noted, however, that the flow in the channel tests was uniform as opposed to highly three-dimensional as in the present injector tests, and furthermore, the model LOX posts used in the present tests are known to reproduce the mode shape of the Haynes posts quite closely, whereas this information is not available for the channel tests posts.

Additional comparisons are made in Figure 3.12 with the earlier CFD model prediction discussed in section 2.0, upon which the design of the model LOX posts used in the present tests was based (curve "D"). This curve shows a predicted instability constant nearly four times lower than the experimental value (probably even further apart, depending on where the actual threhold is

located). Although not entirely proven, this curve could hold the reason as to why the present test LOX posts never reached an unstable condition. It has been ascertained, based on present data, that although the model LOX posts are well suited for accurate structural simulation of the SSME's Haynes LOX posts in terms of mode shape characteristics, their damping and natural frequency are too high for fluid-elastic instability to occur within the operating range of the air flow test facility. This problem is also compounded by the 350 Ft/s transfer duct velocity limitation described earlier.

It is conceivable that the critical velocity required to trigger instability may be only slightly higher than this value, in which case a few relatively simple hardware modifications may be required to accomplish that objective. The analytical model discussed in the next section was used to explore the alternatives available for this purpose. Cases 3 and 4 in Table 3.1 represent two possible alternatives. In case 3, approximately 300 of the fuel injector sleeves were removed in order to double the geometric area in that region. Additionally, the MCC valve used in the MSFC air flow facility was also removed so as to increase the area at that location nearly 25%. Case 4 is a simplified version of case 3, in the sense that only the MCC valve was removed. Table 3.2 shows the resulting effects on the transfer duct velocity, q, and the instability parameter $Up^{1/2}$. These predictions were made with the assumption that the test facility operating range would remain unaltered. The resulting stability boundaries anticipated for cases 3 and 4 are also shown in Figure 3.12. At first sight, case 3 would appear to increase the upper boundary the most by increasing the value of β = 12.2 currently achieved to nearly 35. Case 4, on the other hand, would increase β to about 22, but it would require far simpler modifications to the hardware and would have no effect the injector flowfield, thus retaining the appropriate dynamic similarity.

Extrapolation to Engine Operating Conditions

Perhaps the most important result obtained from this program is the relative position of the stable boundary lines plotted in Figure 3.12 with respect to the SSME FPL operating range shown in the cross-hatched box. This box, defined earlier in Figure 2.6, represents the uncertainty domain of a shieldless injector at FPL conditions, and it was merely transcribed onto Figure 3.12. In consideration of the structural similarity of the model LOX posts, and the dynamic similarity of the model and prototype flow fields, attaining and recording a fluid-elastic instability event would certainly satisfy the academic objectives of the program. In retrospect, another important objective of this program was to examine the likelihood of a shieldless SSME super-post injector to experience fluid-elastic instability at 109% power level engine operating conditions. Based on the data shown in Figure 3.12 it would appear that a shieldless injector would remain quite stable in this operating range. An experimental determination of the actual stability threshold, however, would significantly enhance the confidence level associated with the earlier conclusion.

ONE-DIMENSIONAL ANALYTICAL FLOW MODEL

In connection with the transfer duct velocity limitation reported earlier, a relatively simple one-dimensional flow algorithm was developed in an effort to examine relevant flow effects occurring at locations along the flow path not equipped with instrumentation sensors. The stations of interest are depicted in Figure 2.9. The model was developed in two stages; in the first stage, the available experimental data was used to calculate the pressure loss coefficients associated with each segment of the flow path included between the inlet and exit boundary conditions (stations 0 and 5). After determining the pressure loss coefficients (K_t), the second stage of the algorithm would perform velocity and pressure computations starting from the exit boundary condition, assuming isentropic one-dimensional flow, and utilizing the pressure loss coefficients determined in the first stage of the algorithm. Velocity, pressure, Mach number and q were then calculated at each of the intermediate stations, and were then used as boundary conditions for the next station, and so on, until the inlet boundary conditions were satisfied. In cases where the internal geometry of the flow passage needed alteration, hand calculated estimates of the resulting change in K_t were input to the code.

Model Verification

Verification of the algorithm was accomplished utilizing the available test data from the same injector tests described in this report. The experimental data was available only for stations 0, 2 and 4, and is plotted in Figures 3.13, 3.14 and 3.15, respectively, and is represented by square symbols. The model predictions are plotted on the same figures for comparison. Case 1 denotes the baseline configuration of the HGM air flow model, the other cases represent different configurations discussed earlier in this report. An additional comparison with experimental data is also shown in Figure 3.1.

Figure 3.13 - Computational Model Prediction and Verification of Inlet Total Pressure (Station 0)

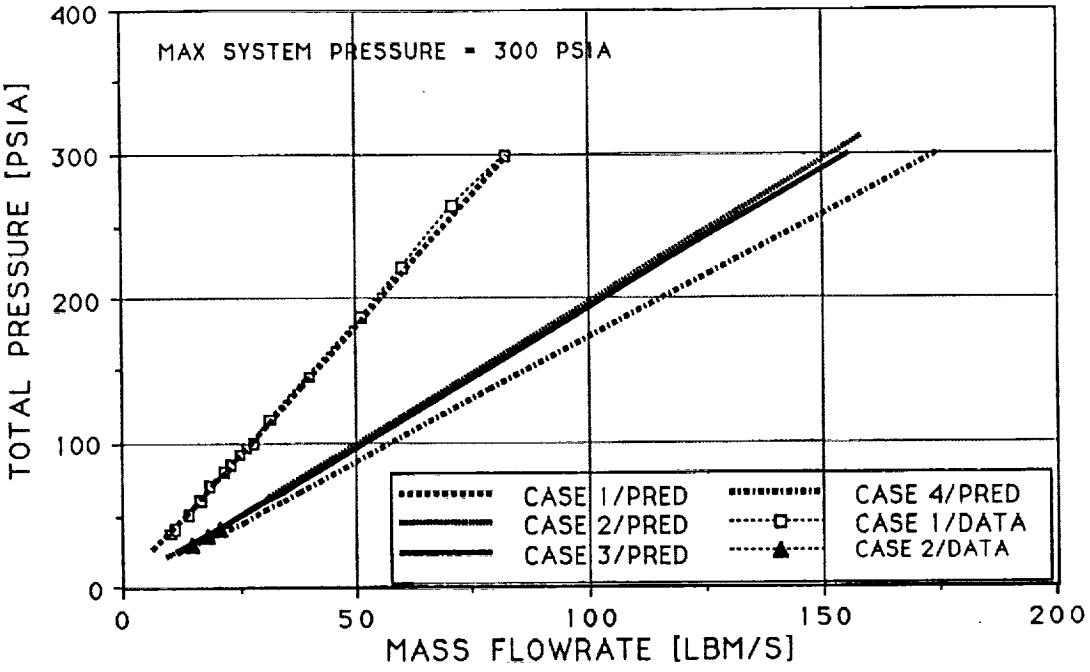

Figure 3.14 - Computational Model Prediction and Verification of Transfer Ducts Static Pressure (Station 2)

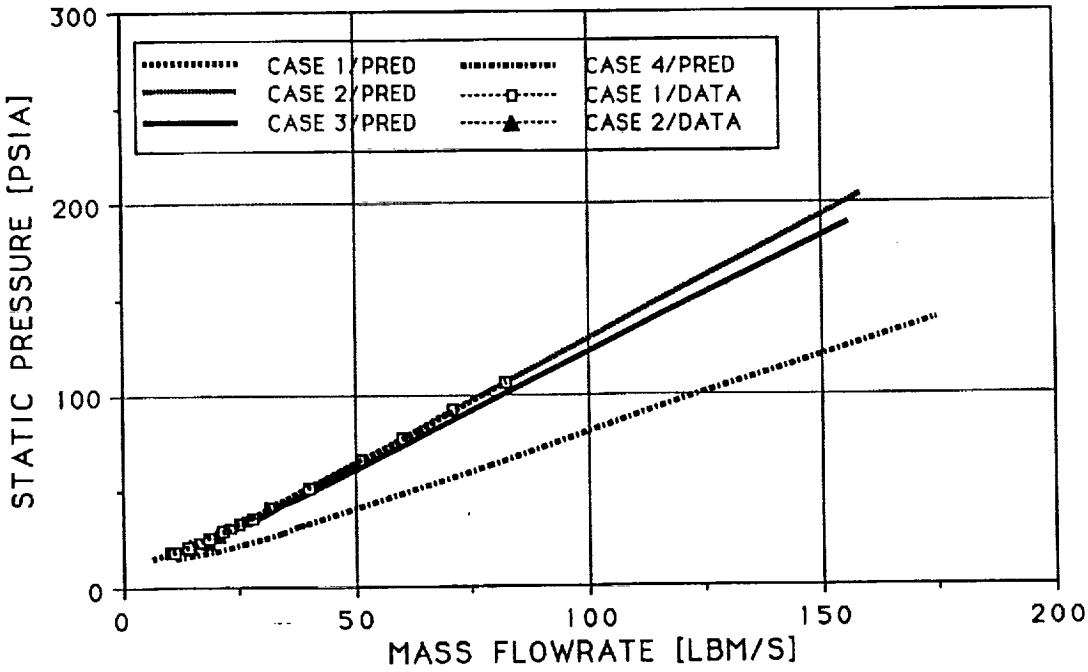

Figure 3.15 - Computational Model Prediction and Verification of MCC Pressure (Station 4)

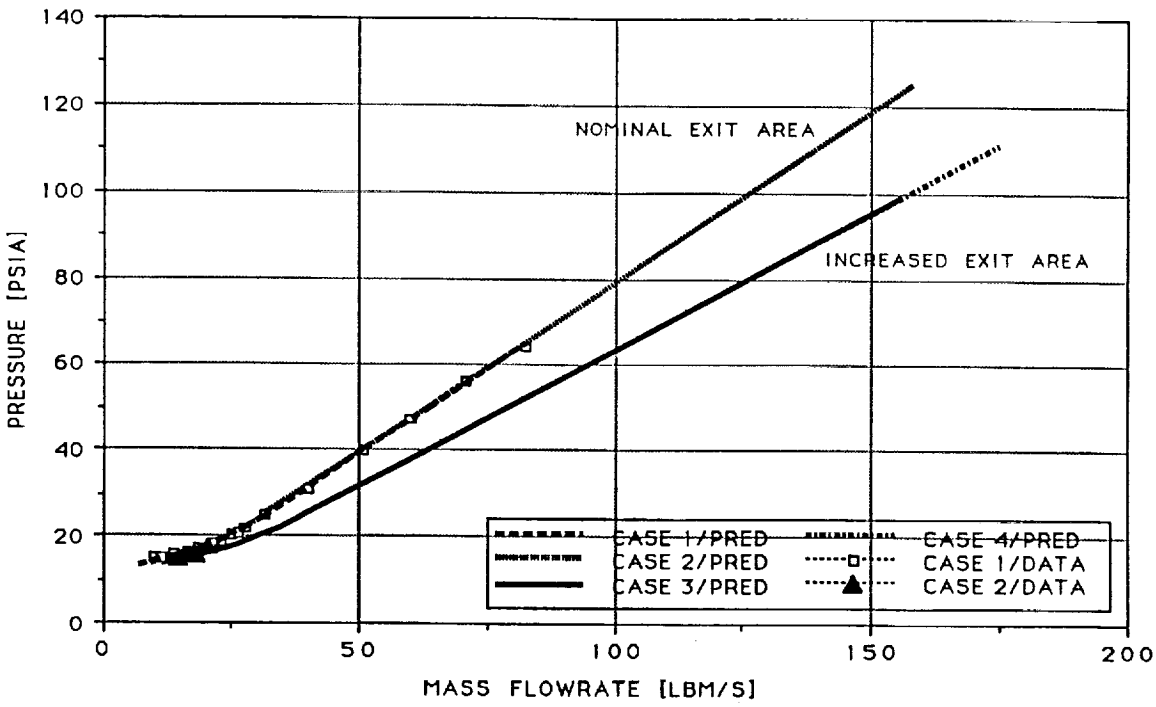

4.0 CONCLUSIONS AND RECOMMENDATIONS

Since the catastrophic engine failures experienced in the early days of the Space Shuttle Main Engine development program, flow shields have been installed on main injector LOX posts in order to prevent reoccurrence of such events. Although the flow shields provide adequate protection against cracking and LOX post rupture, they have an inhibiting effect on the overall performance characteristics of the engine, and also constitute additional weight. The flow shields were originally designed to prevent Cres posts from failing. Since the development days, the new Haynes LOX post design has been incorporated on all engines in the fleet. In addition, a sturdier version of this design, the superpost, has been also introduced. The flow shields, however, retained their status of "standard equipment" on every injector produced. It was never clearly known whether the superpost design would survive the engine FPL environment without the aid of the flow shields, and it probably will never be known with certainty until hot fire tests are performed. This experimental program was designed to provide basic information which would pave the way towards the resolution of this dilemma.

This principle conclusion of this report is that a very successful test program has been conducted to study the flow induced vibration in SSME injector heads. The study was conducted on a 3-duct HGM with an unshielded superpost main injector. While instability was not observed, even at the facility's maximum flow limitations, which resulted in a maximum transfer duct velocity of 350 ft/sec, the results showed that stable performance can be expected in a hot-fire engine test. "Safety" factors of three, based on unstable Rocketdyne channel tests, and four, based on CFD model predications, are derived from the stable experimental values. These observations therefore provide added confidence in the structural integrity of the superposts. It should also be noted that the current Haynes main injector was never tested without the shields.

Concerning the issue regarding the reproduction of a fluid-elastic instability event on one of the model LOX posts tested in this program, it is highly recommended that the air flow model configuration changes addressed in the previous section should be explored further. Temporary removal of the MCC flow control valve, as represented by case 4 in the preceding discussions, is likely to be a relatively simple task. A few runs may be sufficient to ascertain whether the stability threshold can be reached under these conditions; if not, the alternative identified by case 3 can also be explored. In any event, it is highly recommended that the necessary measures be taken to induce and record an unstable condition on the model super-posts; it is believed that such an

accomplishment will provide further physical understanding of the phenomenon, which is likely to be a valuable asset for future engineering tasks as well, and will also increase the level of confidence necessary for the permanent removal of flow shields from future Space Shuttle Main Engines.

REFERENCES

1. D.G.Pelaccio, F.F.Lepore, G.M.O'Connor, G.V.R.Rao, G.H.Ratekin, and S.T.Vogt, "Experimental Evaluation of an Advanced Space Shuttle Main Engine Hot Gas Manifold Design Concept", AIAA Paper No. 84-1463, June 1984.

2. H.J.Connors, "Fluidelastic Vibration and Wear of Steam Generator Tubes", Nuc. Technology, Vol. 55, 1981, pp. 311-331.

3. Y.C.Fung, "Fluctuating Lift and Drag Acting on a Cylinder in Flow at Supercritical Reynolds Number", J. Aerospace Sci., Vol. 27, 1960, pp. 801-814.

4. R.T.Keefe, "An Investigation of the Fluctuating Forces Acting on a Stationary Circular Cylinder in a Subsonic Stream and of the Associated Sound Field", Univ. of Toronto, UTIA Report 76028-1, 1966.

5. M.J.Pettigrew and D.J.Gorman, "Vibration of Heat Exchanger Tube Bundles in Liquid and Two Phase Cross Flow", Flow-Induced Vibration Design Guidelines, PVP-52, ASME, 1981, pp. 89-100.

6. H.J.Connors, "Vortex Shedding Excitation and Vibration of Circular Cylinders", Flow-Induced Vibration Design Guidelines, PVP-52, ASME, 1981, pp. 47-73.

7. R.D.Blevins, Flow-Induced Vibration, Van Nostrand Reinhold Company, New York (1977).

8. M.J.Pettigrew, L.Platten, and Y.Sylvester, "Experimental Studies on Flow Induced vibration to Support Steam Generator Design, Part II: Tube Vibration Induced by Liquid Cross-Flow in the Entrance Region of a Steam Generator", presented at the Int. Symp. on Vibration Problems in Industry, Keswick, UK, 1973, Paper No. 424 (1973).

9. S.D.Savkar and R.M.C.So, "On the Buffeting Response of a Cylinder in a Turbulent Cross Flow", GEAP-24149, September 1978.

10. P.R.Owen, "Buffeting Excitation of Boiler Tube Vibration", J. Mech. Engrg. Sci., Vol. 7, 1965, pp. 431-439.

11. C.Scruton, "On the Wind-Excited Oscillations of Stacks, Towers, and Masts", National Physical Laboratory Symposium on Wind Effects on Buildings and Structures, Paper 16, pp. 798-832, 1963.

12. H.J.Connors, Fluidelastic Vibration of Tube Arrays Excited by Cross Flow", Flow-Induced Vibration of Heat Exchangers, p. 42, American Society of Mechanical Engineers (1970).

13. S.S.Chen, "Design Guide for Calculating the Instability Flow Velocity of Tube Arrays in Cross Flow", ANL-CT-81-40, Argonne National Laboratories, December 1981.

14. M.P.Paidoussis, "A Review of Flow-Induced Vibration in Reactors and Reactor Components", Nuc. Engrg. and Design, Vol. 74, January 1983, pp. 31-60.

15. H.J.Connors, "Fluidelastic Vibration of Heat Exchanger Tube Arrays", Trans.ASME, J. Mech. Design, 100, 347 (1978).

16. H.J.Connors, "Fluidelastic Vibration of Tube Arrays Excited by Nonuniform Cross Flow", Flow Induced Vibration of Power Plant Components, PVP-41, p. 93, ASME (1980).

17. J.Chik and L.Mahorter, "SSME HGM Phase II+ Model Air Flow Testing Pretest Report", Test Number ADF0008, MSFC, 22 Feb.1987, pp. 3-77.